N° d'ordre 146-2005
LYCEN – T 2005-41

Thèse

présentée devant

l'Université Claude Bernard Lyon-I
&
L'Université d'Oklahoma

pour l'obtention du

DIPLOME de DOCTORAT
Spécialité PHYSIQUE des PARTICULES
et SCIENCES de l'UNIVERS

(arrêté du 25 avril 2002)

par

Sébastien BONGARD

Radiation transfer and type Ia Supernovae spectra analysis in the context of Supernovae factory

Soutenue le 4 octobre 2005
devant la Commission d'Examen

Jury :	M.	R.	Schaeffer	Président du Jury Lyon
	M.	E.	Baron	Directeur de thèse
	M.	G.	Smadja	Directeur de thèse
	M.	D.	Branch	
	M.	J.-P.	Chièze	
	M.	P.	Hauschildt	

CENTRE NATIONAL DE LA RECHERCHE SCIENTIFIQUE

IN2P3
INSTITUT NATIONAL DE PHYSIQUE NUCLÉAIRE ET DE PHYSIQUE DES PARTICULES

Université Lyon I - Claude Bernard

&

The University of Oklahoma

Radiative transfer and Type Ia Supernovæ spectra analysis in the context of Supernovæ Factory

A Dissertation submitted

in partial fulfillment of the requirements for the

degree of

Doctor of Philosophy &

Diplome de Doctorat

(arrête du 30 avril 2002)

By

Sébastien Bongard

Lyon, France

Norman, Oklahoma

2005

A Dissertation APPROVED

BY

Baron Edward (Chair)

Smadja Gerard (Chair)

Branch David

Chièze Jean Pierre

Hauschildt Peter

Schaeffer Richard

Acknowledgments

I wish to thank my advisors Eddie and Gerard for embarking with me in these interesting times. Eddie for his support, and his patience in teaching me radiative transfer and how to handle PHOENIX, and Gerard for his sharpness, and the very important corrections he suggested for this dissertation.

In addition to my advisors I wish to thank David Branch for the enlightening discussions we had. Rollin Thomas also deserves credit for the numerous interesting if not always quiet exchanges we had, and for educating me more than he might think in programming and radiative transfer. Darrin Casebeer, in a different way, deserves his name here, also for all these times when we wished PHOENIX could feel pain.

I will also never thank enough Yannick 'SNURP RULES' Copin for his advises and his help when I started. He even deserves the doubtful privilege to be responsible for me using emacs, idl, and xblast. In the same context I have to thank Damien 'Minou' Vercauteren for his icq time, his geek spirit, and for introducing me to bash.org.

Finally, I wish to thank my brother for believing I will one day have a "real job", and my wife, for without her this work would never have been what it is, and me neither.

I haven't at all forgotten you guys, from both Lyon and Norman, who I shared my office with, and I want to thank you because you where indeed wonderful company.

And there is you who became my friend and without whom this work would probably not have been finished.

Contents

List of Figures

List of Tables

Résumé

Dans cette thèse, effectuée en cotutelle avec l'Université d'Oklahoma City, nous avons étudié le transfert radiatif dans les enveloppes en expansion rapide des supernovæ de type Ia (SNeIa) dans le cadre de la collaboration Supernovæ Factory .

Ces étoiles qui explosent avec une luminosité comparable à celle d'une galaxie sont utilisées comme *chandelles standard* permettant d'étudier le comportement à grande échelle de l'univers. Nous avons utilisé le code de transfert radiatif PHOENIX développé par P.Hauschildt, F.Allard et E.Baron, pour simuler des spectres de SNeIa à différentes dates et luminosités afin d'étudier le processus de formation spectrale. Nous avons parallèlement élaboré un module de grille adaptative qui augmente sa robustesse de convergence.

Nous avons montré que la formation des spectres de SNeIa n'était pas aussi localisée que dans le modèle photospherique standard mais qu'elle mettait en relation des régions allant de 5000km.s^{-1} à 20000km.s^{-1} pour des époques proches du maximum de luminosité. Nous avons de plus développé des indicateurs spectraux permettant de mesurer la luminosité des SNeIa avec une précision égale à celle des méthodes basées sur l'analyse des courbes de lumière. Il devient ainsi possible de contraindre de faćon indépendante l'évolution des SNeIa avec le redshift, ce qui place ce travail à l'interface entre l'étude des supernovæ en tant qu'objets stellaires et leur utilisation en cosmologie.

Abstract

This co-supervised dissertation was conducted in collaboration between The University of Oklahoma City (USA) and Université Claude Bernard of Lyon (France). It addresses the radiative transfer issue in type Ia supernovæ expanding envelopes, in the context of the SUPERNOVÆ FACTORY .

We used the multi-purpose radiative transfer code PHOENIX, developed by P.Hauschildt, F.Allard and E.Baron to produce a grid of synthetic spectra sampling dates from 10 to 25 days after explosion and bolometric magnitudes from -18.0 to -19.7. We also developed an adaptive grid scheme in order to stabilize PHOENIX convergence.

We showed the spectrum formation in SNEIA around maximum light to be a multi-layered process involving regions from 5000km.s^{-1} to 20000km.s^{-1}, interacting not only through scattering but also through pure emission. This new understanding allowed us to introduce a new spectral indicators we called $\Re_{SiS}$, which can be used to measure SNEIA blue magnitudes with a precision comparable to the stretch factor. This makes it possible to independently constraint the evolutionary effect on SNEIA that are of crucial importance for high z surveys.

Chapter 1

Introduction

1.1 Scientific background

In the frame work of General Relativity, the universe mass density is described by Ω_M, its curvature by Ω_k, and any possible *dark energy* by Ω_Λ, where Λ is the so called *cosmological constant*, related by $\Omega_M + \Omega_\Lambda + \Omega_k = 1$.

In Fig. 1.1 we display the results of three different experiments that prove according to three different experiments, Ω_M and Ω_Λ have to be finite at a two σ level. The ellipsoids denoted as "supernovæ" are based on the **SCP** results, one of the two experiments that used type Ia supernovæ (or SNeIa) as cosmological probes. Both groups, the **SCP** and the **High z** team, used these extremely bright exploding stars[1] with a very homogeneous B band luminosity as *standard candles.*

Moreover, both groups found a way to correct for part of the SNeIa blue magnitude intrinsic dispersion[2]. As can be seen in Fig. 1.2, SNeIa absolute blue magnitude dispersion can be well accounted for, decreasing the intrinsic dispersion to $\approx \pm 0.15$ blue magnitudes. Note that the upper panel of the figure exaggerates the natural SNeIa dispersion, since lots of "normal" supernovæ have not been plotted for clarity sake.

Knowing the SNeIa absolute luminosity in the B band from the *stretch* or $\Delta_{m_{15}}$, and measuring their apparent blue magnitude, their *luminosity distance* d_L can be inferred, as

[1] as bright as a whole galaxy, i.e. ≈ -19 absolute blue magnitude

[2] **SCP** calling it stretch factor, and **High z** team calling it $\Delta_{m_{15}}$. These are slightly different methods based on the same physical correlation between the SNeIa blue light curve evolution time and maximum.

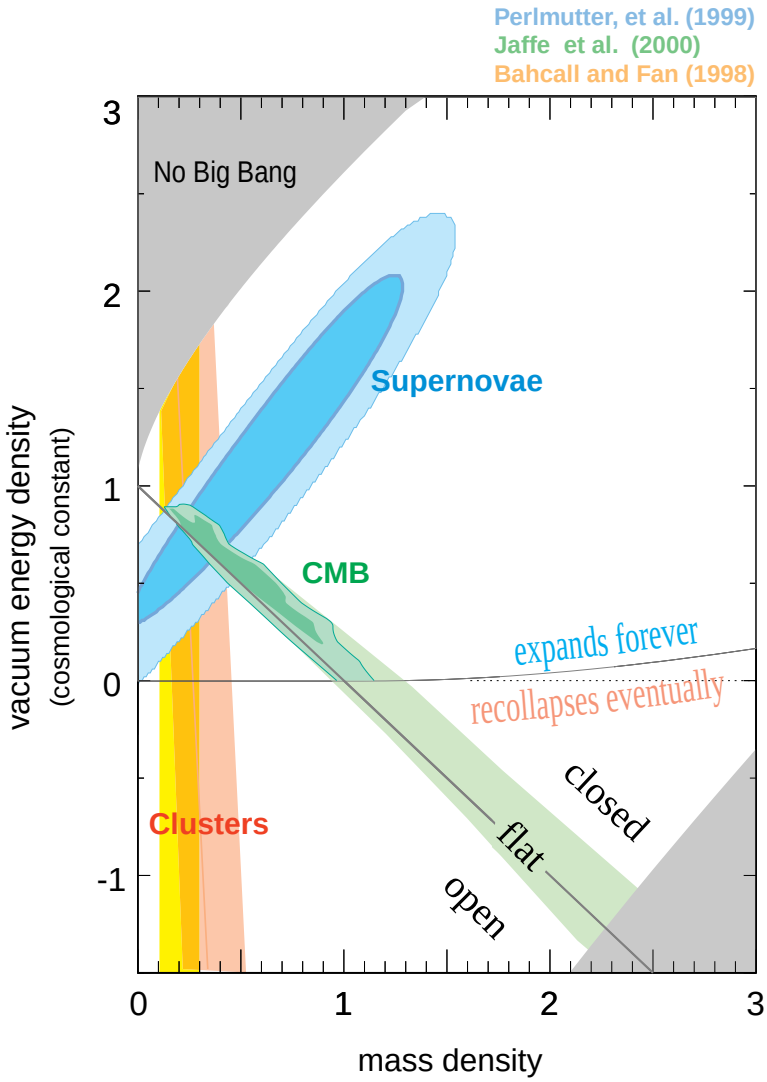

Figure 1.1: *CMB stands for* ***C****osmological* ***M****icrowave* ***B****ackground, and the supernovæ result is the* ***S****upernova* ***C****osmology* ***P****roject (Perlmutter et al. (1999)) one. The* ***High*** *z team result (Filippenko & Riess (1998)) is very similar.*

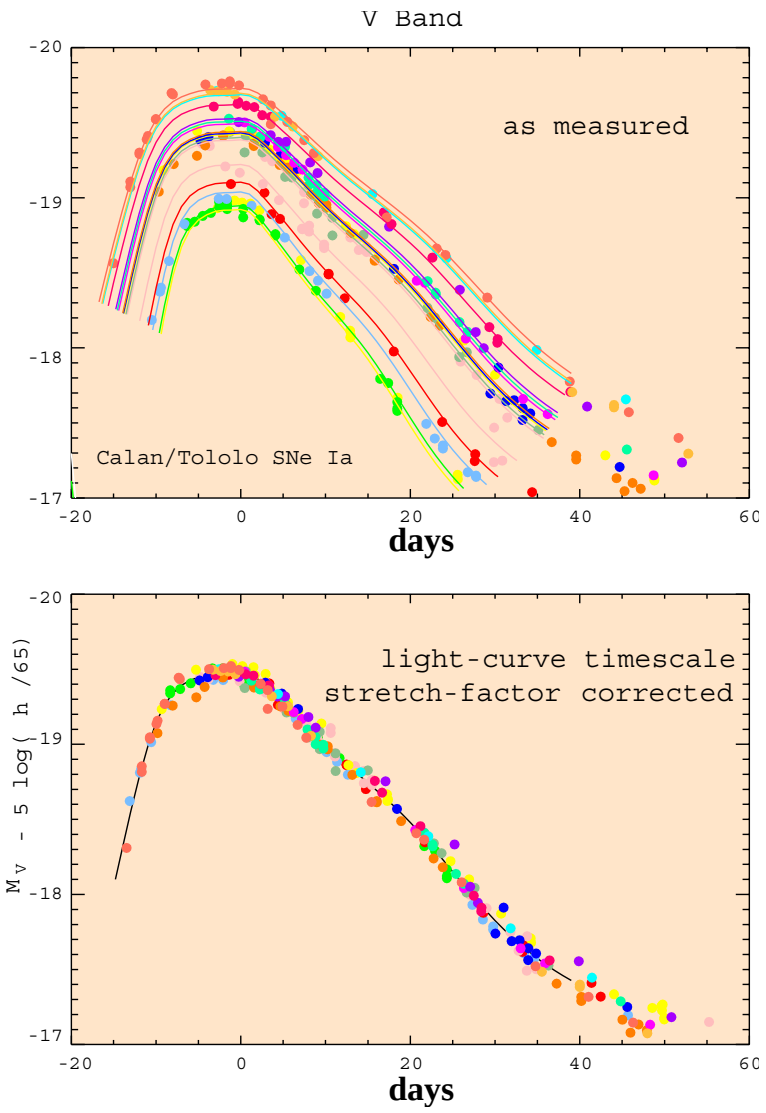

Figure 1.2: SNeIa *light curves. The dispersion of the upper figure is exaggerated as a lot of intermediate(and therefore* standard*)* SNeIa *have been omitted.)*

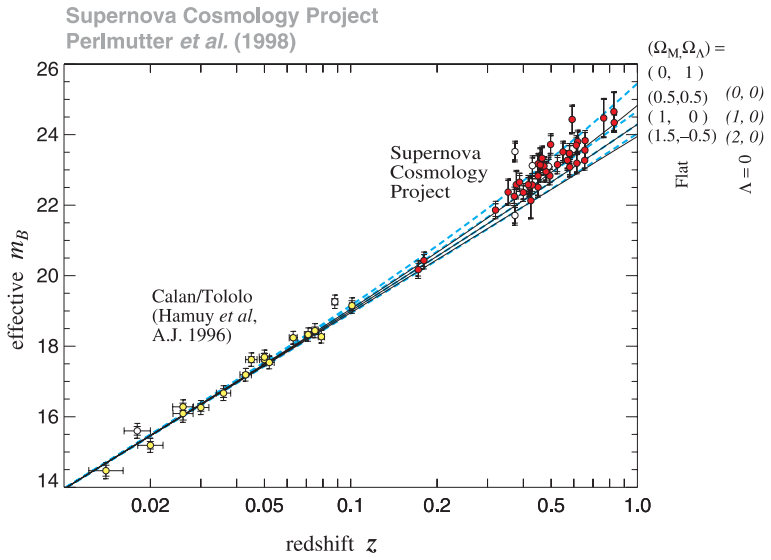

Figure 1.3: *Hubble diagram by SCP group*

shown in eq. (1.1).

$$F_{d_L}/F_0 = d_L^2/10^2 \tag{1.1}$$

where d_L is in parsecs, F_0 is the absolute flux of the supernova at 10pc, and F_{d_L} is the apparent flux of the supernova. Note that prior to show that the SNeIa are good *standard candles* with SNeIa in the Hubble flow, their absolute blue magnitudes had to be calibrated using independent indicators like Cepheids, which means that SNeIa are *secondary* distance indicators.

This luminosity distance d_L describes the distance at which the supernovæ appear to be, and is a function of redshift, the Hubble constant, the universe curvature, Ω_M and Ω_Λ as described by eq. (1.2), eq. (1.3) and eq. (1.4).

- if $\Omega_k < 1$

$$d_L = \frac{c}{H_0}\frac{1}{\Omega_k^{1/2}}\sinh\left(\Omega_k^{1/2}\int_0^z [(1+z)^2(1+\Omega_M z) - z(2+z)\Omega_\Lambda]^{1/2}dz\right) \tag{1.2}$$

- if $\Omega_k > 1$

$$d_L = \frac{c}{H_0}\frac{1}{(-\Omega_k)^{1/2}}\sin\left(\Omega_k^{1/2}\int_0^z [(1+z)^2(1+\Omega_M z) - z(2+z)\Omega_\Lambda]^{1/2}dz\right) \tag{1.3}$$

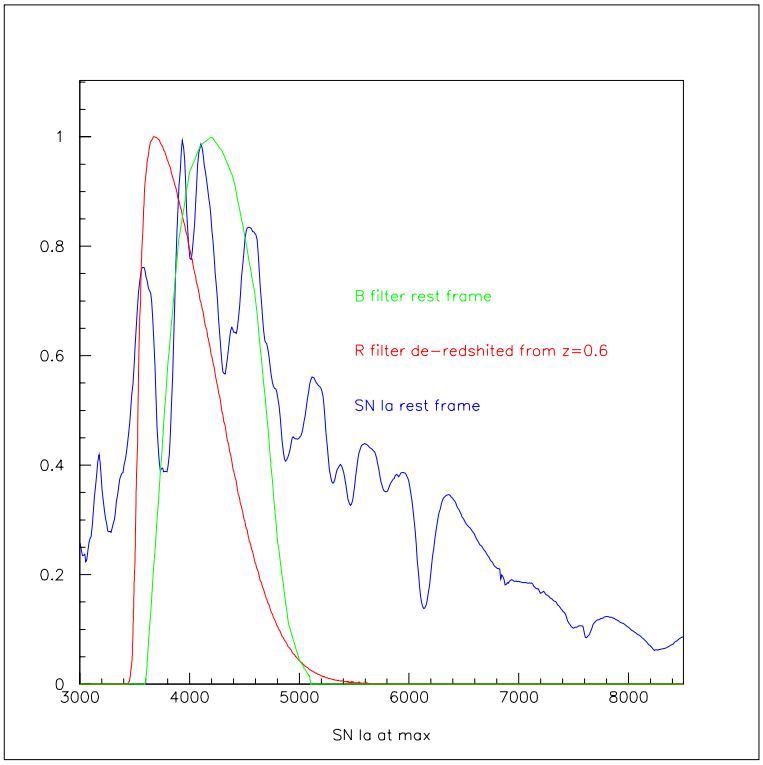

Figure 1.4: *K corrections. The green curve is the blue filter in the* SNIa *rest frame, showing the part of the spectra we are interested in. The red one is the red filter in Earth rest frame blueshifted to the* SNIa *rest frame. We see that the part of light we are interested in falls "almost" in this filter. This means that to measure the blue magnitude of the supernova, we have to observe it in the red filter, and correct for the differences between the two filters . Accounting for this effect is what is called K corrections.*

- if $\Omega_k = 0$ (Which is compatible with the data and usually assumed to be the case)

$$d_L = \frac{c}{H_0} \int_0^z [(1+z)^2(1+\Omega_M z) - z(2+z)\Omega_\Lambda]^{1/2} dz \tag{1.4}$$

By plotting d_L vs z, the possible values of the Ωs can be constrained, usually assuming a flat universe which is the most consistent with the **CMB** measures. Fig. 1.3 shows the **SCP** results, where we see that $0 < z < 0.1$ data do not constrain the values of the Ωs. On the other hand, at $0.6 < z < 1.$, the larger lever arm allows to constrain $\Omega_\Lambda - \Omega_M$ as has been done by the **SCP** and the **High z** team.

At $z > 1.5$, the Ω_M term dominates the expansion rate, breaking the degeneracy of the previous result. The natural evolution of the **SCP** program was thus to observe farther SNeIa in order to estimate Ω_M and further constrain the Universe equation of state which is the goal of the space project **SNAP**. But for this project to be conclusive, several specifications must be met (cf Kim et al., 2004).

First, distant SNeIa have their spectra redshifted, which makes their luminosity measure in any given filter complex: the filters used in the Earth rest frame will usually *not* correspond

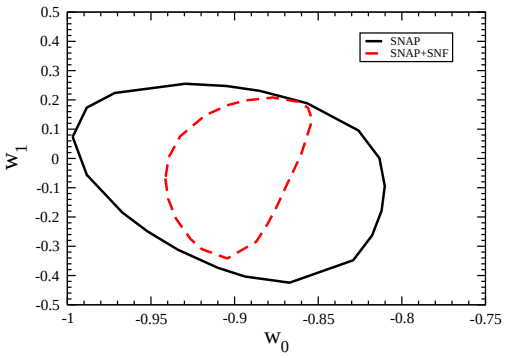

Figure 1.5: SNAP/JDEM *with and without* SUPERNOVÆ FACTORY *results.* ω_0 *and* ω_1 *are the two first terms of the Universe's equation of state expansion with respect to* z

to any classic filter in the SNIA rest frame, as can be seen in Fig. 1.4. Building a set of filters accounting for each redshift is of course out of question. "K corrections" are a way to correct for this effect. This critical photometric issue can also be solved using a good SNEIA spectra catalog to infer from the colors at z the corresponding colors at rest.

This scheme will be implemented in SNAP/JDEM making a good SNEIA spectra catalog a prerequisite for this high z space program. SNAP/JDEM will also incorporate a dedicated spectrograph able to do spectrophotometry, in order to constrain the systematics inherent to the K correction method.

In order to take full advantage of the large leverage power of high z measurements, the zero point of the Hubble diagram previously displayed in Fig. 1.3 has to be accurately fixed. Fig. 1.5 shows how a large survey of nearby SNEIA could improve SNAP/JDEM results by addressing this issue.

In addition, if the SNEIA host galaxies could be observed, metallicity studies might be performed. They would help to constrain the potential evolution of SNEIA luminosities with the age of the universe (or redshift), which is so far only taken into account as a systematic error.

Finally, a large nearby SNIA survey would provide high quality data that would be of great use for the study of these stellar objects. Not only would the understanding of the SNEIA homogeneity be comforting when using them for cosmological studies: these objects are also *intrinsically* fascinating. They are among the very few astronomical objects that evolve on a human time scale, displaying extreme physical conditions even on stellar standards, and they are as well one of the two heavy element producers of the Universe which makes them fundamental in its evolution. Moreover, the understanding of SNEIA

spectral formation might lead to independent luminosity indicators that would prove useful when constraining the systematic errors in SNAP/JDEM like programs.

All these considerations lead to the project called **S**uper**N**ova **F**actory, as the first step toward a high z SNeIa survey.

1.2 Supernovæ Factory and SNIFS

The Supernovæ Factory is a collaboration between French and American laboratories: The **CRAL**[3] Observatory (Lyon), the **IPNL**[4] (Lyon), the **LPNHE**[5] (Paris), and the **LBL**[6] (Berkeley). Its purpose is to use an integral field spectrometer (called SNIFS for **S**uper**N**ovæ **I**ntegral **F**ield **S**pectrometer) to follow spectrophotometrically ≈ 300 SNeIa within 4 years.

This spectrograph is an **I**ntegral **F**ield **U**nit, or **IFU**: instead of falling on a slit as in usual spectrographs, the image of the sky is focussed on a microlens array whose focal plane coincides with a detection CCD on the other side of a grism (grating+prism).

Each microlens therefore contains a small specific section of the sky ($0.4'' \times 0.4''$ in SNIFS case) which light will be focused and scattered into a single spectrum on the CCD. The complete image on the CCD will therefore be a collection of spectra, each one corresponding to a definite part of the sky. This result in the **IFU** gives spatial as well as spectral information, which explains why they have first been used in galactic surveys, where they allowed the velocity mapping of the galaxies. This feature is expected to prove useful when extracting the supernova from the galaxy.

Moreover, since SNIFS total field of view is a $6'' \times 6''$ microlens array and not a slit, it will contain the whole supernova[7]. Therefore, no unknown part of the supernova light would be cut off, as in slit spectroscopy, making photometry possible at the same time as spectrometry for **IFU**s. This scheme is summarized in Fig. 1.6. Since SNIa spectrophotometry of high quality is very rare and of crucial importance to achieve the Supernovæ Factory scientific goals, the central part of the project had to be an integral field unit: SNIFS.

[3]Centre de Recherche Astronomique de Lyon
[4]Institut de Physique Nucléaire de Lyon
[5]Laboratoire de Physique Nucléaire et des Hautes Énergies
[6]Laurence Berkeley Laboratory
[7]Differential refraction at high airmass can extend the supernova enough for this statement to become inaccurate.

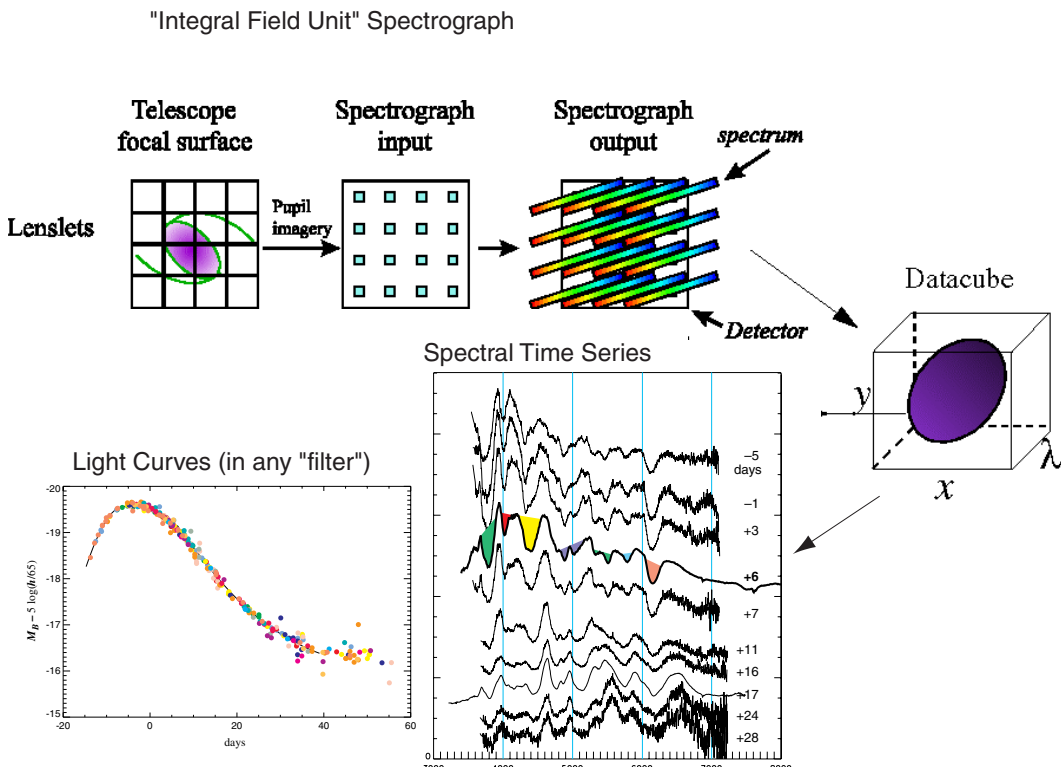

Figure 1.6: SNIFS *IFU principle*

SNIFS has been built at the **CRAL** in France, as they have great expertise in this field[8], and is mounted on UH telescope on the Mauna Kea in Hawaii.

The SNeIa detection uses the **NEAT**[9] data to find variable objects. Since asteroids are moving objects close to the Earth, the same field can be scanned every 3 days without decreasing their detection probability. This allows us to find variable objects by "simple" subtraction. The main problems of this method come from the huge volume of data that has to be dealt with. Also, each field of view is not observed at the same time each night, and is therefore rotated at a different angle with respect to the CCD in each exposure. Even worse, the seeing varies from night to night, making it easier to find subtraction artifacts like rings than variable objects.

Once the true variable objects have been found, there is a discrimination between type Ia candidates and other variable objects. This is done using the two exposures separated

[8]They built the IFUs of the **Tigre**, **Oasis**, and **Sauron** projects.
[9]**N**ear **E**arth **A**steroid **T**racking

by three days where the varying object appears, plus the reference pose. Rise time considerations allow to sort out AGNs and quantify the likelihood of a candidate to be type Ia supernovæ. Once this first sort is done, a SNIFS exposure is taken in order to identify the candidate. If it appears that it is a SNIa, it will then be followed until about 40 days after maximum light.

1.3 Type Ia supernovæ

The Supernovæ Factory is the background in which this PhD work takes place, and supernovæ spectra analysis is its cap stone. The only pieces of information we require about SNeIa are spectra and photometry, and luckily enough lots of information can be found in the optical.

Therefore, radiative transfer plays a key role in understanding type Ia supernovæ, since it connects their physical structure to what we observe. The motivation of this PhD work was using synthetic spectrum simulators, to understand spectra formation better as well as its link to SNeIa physical structure, which we now discuss.

1.3.1 Progenitors

SNeIa display these very specific features:

- SNeIa luminosity is homogeneous
- SNeIa spectral features consist of blends of wide P-Cygni profiles
- SNeIa spectra display no hydrogen lines
- SNeIa spectra display no helium lines
- SNeIa spectra display strong SiII and CaII lines
- ≈ 1 SNIa explosion per galaxy per 1000 years

The homogeneity of the luminosity points toward an *homogeneous* class of progenitors. Since there are neither helium nor hydrogen lines in the spectra, the abundance of these elements must be low, therefore pointing toward *old* progenitors.

The wide P-Cygni profiles [10] show that the element velocities are very high (going all the way up to above 30000km.s^{-1}), which leads to an estimate of the total kinetic energy to be ≈ 1 *foe*, i.e. 10^{51}ergs. This impressive amount of energy, together with the shape of SNeIa light curves which is at late times dominated by nuclear disintegration suggests *thermonuclear explosions* as SNeIa energy source.

All these elements lead Colgate & White (1966) to propose type Ia supernovæ to be White Dwarf (**WD** in the following) thermonuclear explosions. This makes these supernovæ very specific, in that they are the only ones not powered by a core collapse mechanism.

The process that leads to the White Dwarf explosion is still not well understood, but the community mostly agrees on that the typical type Ia progenitor is most likely to be a *near Chandrasekhar mass* White Dwarf that reached this mass through accretion from a binary companion.

Many different accretion models, together with collapsing binary **WD** systems have been proposed, and are still debated. Whether or not the type Ia diversity comes from a diversity of progenitor systems is still an unresolved issue. What is certain is that in our actual knowledge of **WD** populations, none of these models can account for the ≈ 1 SNIa per galaxy per 1000 year alone. Whether or not there are enough **WD** in order to account for all the type Ia supernovæ observed is still to be determined.

On the other hand, the explosion models that fit the observations the best are *near Chandrasekhar mass* C/O **WD** thermonuclear explosions, making them the widely accepted candidate for type Ia supernovæ progenitors.

1.3.2 Explosion models

The main problem of **WD** explosion simulations resides in the thermonuclear flame development. The object to be simulated is approximately 1000km wide, and the flame structure is dominated by turbulent effects that take place at the centimeter scale. To simulate such a process would require more computing power than currently available, or, alternatively clever coding schemes and parameterizations.

The first step in **WD** explosion simulation was to compute 1D models, and they are

[10] more will be said on these profiles in 2.1

still the only models that run fast enough to allow accurate nucleosynthesis simulations. In these models, the flame propagation has to be parameterized since there are not enough dimensions for turbulence to develop[11]. Flame velocity is then used as a free parameter to tune the nucleosynthesis. At high densities, the C/O **WD** burns into mainly nickel and other *heavy* elements ($A \approx 56$). At intermediate densities, it burns into *intermediate mass* elements like silicon, magnesium, sulfur, etc. And at low densities the flame dies out.

As the **WD** burns, there is a competition between its expansion, due to the huge energy input coming from the flame, and the flame propagation. The quicker the flame, the bigger part of the **WD** that will burn at high densities, and therefore the higher the mass of nickel produced. Similarly, if the flame is slow more intermediate mass elements will be produced before the flame dies out.

The most famous of type Ia 1D models ever computed is called W7 (cf. Iwamoto et al., 1999) and has been the one giving the best results in simulating SNeIa spectra for more than 20 years. It is the model that was used the most in this PhD work, and it will be discussed much more thoroughly later on.

Lots of other 1D models have been computed, and more will be said about them. Particularly, the other models we used are different in that they are *delayed detonations*. This means that the subsonic flame is at some point artificially turned into a supersonic flame.

Whether or not this really happens in real **WD** explosions is still a topic of intense debate, but what is sure is that it can happen for non thermonuclear flames[12].

Recently, in addition to 1D models, some 2D and 3D models have been computed. The solution of the scale problem has been very nicely overcome through turbulence theory, which allows us to simulate larger scale flame fronts without micro-detailed simulation. Still, the computing power needed to simulate a full **WD** explosion is tremendous, and it is not yet possible to compute accurate nucleosynthesis from a 3D model.

Nonetheless, the understanding of **WD** explosions has improved a lot, and the Nickel/Cobalt disintegration chain powering of SNeIa is not challenged any more. In this context, with

[11] Turbulence needs *at least* 2D, in order for the instabilities to develop.

[12] A natural gas pipeline in Siberia for example once started to burn. And it was clearly seen from the temperature monitoring that the flame at some point turned form steady subsonic burning into supersonic, and therefore one can say pretty unsteady, burning.

the foreseeable advent of accurate nucleosynthesis from 3D models less parameterized than 1D ones, the very high quality of SUPERNOVÆ FACTORY spectrophotometry will be of great use to constrain and test their prediction. This cannot be achieved without lots of radiative transfer, since the only available information from the explosion model comes from SNEIA spectra.

Chapter 2

PHOENIX and Radiative Transfer

In this chapter will be presented some radiative transfer notions as well as the radiative transfer code SYNOW and PHOENIX used in this thesis work.

2.1 Some Radiative Transfer notions

2.1.1 Definitions

The specific intensity

To study light transfer in any physical environment, there are at least three different approaches. The first one would be to use Maxwell's equations, and is suited for local interaction between the radiation and the environment studies.

An other approach is the Monte-Carlo method, where photon propagation is simulated individually or by packets, following their path through the considered media. Its property to take care of complex integrals by simple photon summation make it especially suited for 3D radiative transfer. Some 1D and 3D Monte-Carlo based works could be found in Thomas et al. (2002), Kasen et al. (2003), Mazzali (2000) for example.

The third method, used in both codes that we worked with, is analytical and studies the energy transfered by light, instead of it's "vehicle"(photons, or electro-magnetic fields). The key function used in this formalism is the *specific intensity*, usually noted $I(\mathbf{r}, \mathbf{n}, \nu, t)$, defined with eq. (2.1) as the energy transported in the direction $\mathbf{n}$ by a radiation of frequencies $\nu, \nu + d\nu$ across an element of area dS into a solid angle $d\omega$ in a time interval dt (cf Fig. 2.1).

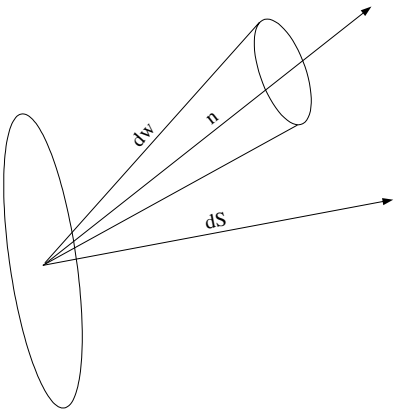

Figure 2.1: *Pencil of radiation used to define specific intensity. The vector* $\mathbf{n}$ *is the direction of propagation, while* $\mathbf{dS}$ *is the vector perpendicular to the element of area* dS*, such that* $||\mathbf{dS}|| = dS$

$$dE = I(\mathbf{r}, \mathbf{n}, \nu, t)\ \mathbf{dS}\ \mathbf{n}\ d\omega\ d\nu\ dt \tag{2.1}$$

Mean intensity, energy density and radiation pressure

From now, we will note $A(\mathbf{r}, \mathbf{n}, \nu, t) = A_\nu$ any function depending on $\mathbf{r}$ and $\mathbf{n}$, once it has been defined.

The mean intensity of the radiation, or first moment of the intensity is defined as the integral of I_ν over all directions:

$$J(\mathbf{r}, \nu, t) = \frac{1}{4\pi} \int_0^{4\pi} I_\nu d\omega \tag{2.2}$$

and is related to the energy density of the radiation field by

$$E(\mathbf{r}, \nu, t) = \frac{4\pi}{c} J_\nu(\mathbf{r}, t) \tag{2.3}$$

The specific intensity's second and third moments are defined using $\mu = cos(\theta) = \mathbf{n} \cdot \frac{\mathbf{dS}}{||\mathbf{dS}||}$. These quantities are related to the flux F, and the radiation pressure P, as shown in eq. (2.4), eq. (2.5), eq. (2.6) and eq. (2.7).

$$H_\nu(\mathbf{r},t) = \frac{1}{4\pi}\int_0^{4\pi} I_\nu \mu d\omega \tag{2.4}$$

$$F_\nu(\mathbf{r},t) = 4\pi H_\nu(\mathbf{r},t) \tag{2.5}$$

$$K_\nu(\mathbf{r},t) = \frac{1}{4\pi}\int_0^{4\pi} I_\nu \mu^2 d\omega \tag{2.6}$$

$$P_\nu(\mathbf{r},t) = \frac{4\pi}{c} P_\nu(\mathbf{r},t) \tag{2.7}$$

These integral quantities allow us to describe the energy flow of unpolarized light. Polarization could also be added to this formalism, but since it was not included in either SYNOW, or PHOENIX, we will only refer the reader to the literature, for example Kasen et al. (2003).

2.1.2 Radiative transfer equation

The problem to be solved in radiative transfer is to find the solution of the differential equation describing the local energy balance of the radiative field with appropriate boundary conditions. This trivially stated problem is made "more interesting[1]" by the non linearity of the electromagnetic field coupling with the matter. Moreover, the radiative field also couples spatially distant points, adding non locality to the difficulty of the problem.

The energy *sinks* are described by the **extinction coefficient or function**, usually noted $\chi(\mathbf{r},\mathbf{n},\nu,t)$. Eq. (2.8) relates it to the energy extracted from a beam of specific intensity I_ν, going through a volume element of surface dS and length ds, propagating into the solid angle $d\omega$ during the time dt:

$$\delta E = \chi(\mathbf{r},\mathbf{n},\nu,t)\ I(\mathbf{r},\mathbf{n},\nu,t)\ dS\ ds\ d\omega\ d\nu\ dt \tag{2.8}$$

$$\chi(\mathbf{r},\mathbf{n},\nu,t) = \kappa(\mathbf{r},\mathbf{n},\nu,t) + \sigma(\mathbf{r},\mathbf{n},\nu,t) \tag{2.9}$$

Using the extinction coefficient, we define the *photon mean free path* to be $l_\nu = \frac{1}{\chi_\nu}$,

[1] "May you live interesting times" Old Chinese curse

which describes the photon mean propagation length in the considered medium.

The extinction coefficient usually takes into account scattering, noted σ, as well as "true absorption"[2], noted κ. It is often convenient to include the induced emission in κ, as a "negative" absorption. Since the stimulated emission is coherent, the mean free path of the photon remains $l_\nu = \frac{1}{\chi_\nu}$, even though the simulated emission is taken into account in κ.

The **emissivity**, denoted $\eta(\mathbf{r}, \mathbf{n}, \nu, t)$ describes the amount of energy released into the beam through relation eq. (2.10) which uses the same conventions than eq. (2.8).

$$\delta E = \eta(\mathbf{r}, \mathbf{n}, \nu, t)\ dS\ ds\ d\omega\ d\nu\ dt \tag{2.10}$$

Finally, the energy balance of the volume element previously defined gives the general radiative transfer equation (2.11):

$$\frac{1}{c}\ \frac{\partial I_\nu}{\partial t} + \frac{\partial I_\nu}{\partial s} = \eta_\nu - \chi_\nu\ I_\nu \tag{2.11}$$

where η_ν, the emissivity is given by $\eta_\nu = \kappa B_\nu + \sigma J_\nu$, where B_ν is the Planck function and J_ν is the zeroth Eddington moment of the specific intensity.

For further discussion we will consider the static plane parallel case in non relativistic matter flows, in order to emphasize the physics over the algebra.

Equation (2.12) is the standard radiative transfer equation for a one-dimensional planar atmosphere, where the coordinate z increases toward the external observer.

$$\mu\ \frac{\partial I_\nu}{\partial z} = \eta_\nu - \chi_\nu\ I_{nu} \tag{2.12}$$

It is then useful to define the **optical depth** $\tau(z, \nu)$:

$$\tau(z, \nu) = -\int_{z_{max}}^{z} \chi(z', \nu)\ dz' \tag{2.13}$$

which increases with non zero opacities zones[3]. Equation (2.12) now becomes:

[2]By opposition to scattering, which could result in "absorption" features since the scattering of light in all directions from an incoming beam results in a diminution of the intensity in the beam direction.

[3]τ increases *from* the observer, i.e. it goes the opposite direction from the z axis previously defined.

$$\mu \frac{\partial I_\nu}{\partial \tau} = I_\nu - S_\nu \quad (2.14)$$

$$S_\nu = \frac{\eta_\nu}{\chi_\nu} \quad (2.15)$$

Where S_ν is the **source function**, describing the ratio of emissivity over absorption in the medium. The formal solution of eq. (2.14) can then easily be calculated analytically and reads:

$$I(\tau_1, \mu, \nu) = I(\tau_2, \mu, \nu)\ e^{-(\tau_2 - \tau_1)/\mu} - \mu^{-1} \int_{\tau_1}^{\tau 2} S_\nu e^{-t/\mu}\ dt \quad (2.16)$$

Let us consider the case of an incoming beam with direction $\mu = cos(\theta) = 1$. We suppose that this beam crosses a zone of finite optical depth and of constant source function, as it is the case for example in the Sobolev approximation that will be developed later on. In this case, equation (2.16) becomes:

$$I(0, \mu = 1, \nu) = I(\tau_{-\infty}, \mu = 1, \nu)\ e^{-\tau_{-\infty}} + \ S_\nu(1 - e^{\tau_{-\infty}}) \quad (2.17)$$

The left hand side of this formal solution is the intensity seen by the observer looking photons going in the $\mu = 0$ direction. The right hand side describes the different contributions to this intensity. The first term expresses the incoming intensity decreases as it goes through an absorbing or scattering zone. The larger the optical depth, the more the intensity will exponentially fade. Whenever the first term dominates, it will result in absorption features with respect to the incoming intensity.

The second term of the right hand side gives the emission contribution to the observed intensity. This time, the larger the optical depth, the more important the contribution of the source function. A region where the optical depth is higher than one is called "optically thick", and where the optical depth is less than one "optically thin".

Outside of an optically thick layer heated by incoming radiation, we will only see the source function contribution, the incoming beam being completely shielded by the medium. But it will change the local energy density and therefore indirectly change the source function. Also, for an incoming beam in the $\mu = 0$ direction, i.e. perpendicularly with respect to the observer, only the source function term will remain, accounting for the pure emission

as well as the incoming beam scattering.

Calculating the spectrum needs the solution of the transfer equation for a given structure, and the knowledge of the opacities and the source function. If the source function and the opacity are known, inverting the radiative transfer equation to find the intensity becomes easy. The calculation of the flux then only needs the integration of I_ν into H_ν. The complexity of the problem resides in the fact that usually the source function is not known independently of J_ν and thus of I_ν, and both have to be calculated simultaneously.

Assuming the opacities to be known, in order to calculate S_ν, we integrate the formal solution over all directions, i.e. over $\mu = cos(\theta)$, transforming eq. (2.16) into:

$$J_\nu(\tau_\nu) = \frac{1}{2}\int_0^\infty S_\nu E_1(t_\nu - \tau_\nu)dt_\nu \tag{2.18}$$

$$E_1(x) = \int_1^\infty t^{-1}e^{-xt}\,dt \tag{2.19}$$

if the source function is isotropic.

This last equation is then usually written in operator formalism, which can be transformed to matrix notation once we discretize the problem. It then reads:

$$\Lambda_\tau[f(t)] = \frac{1}{2}\int_0^\infty f(t)E_1(t_\nu - \tau_\nu)dt_\nu \tag{2.20}$$

$$J_\nu = \Lambda_{\tau_\nu}[S_\nu(t)] \tag{2.21}$$

Since both the intensity, and therefore J_ν, and the source function are supposed to be unknown, eq. (2.20) has to be solved iteratively taking into account the considered problem boundary conditions.

The Λ_ν operator contains information on the opacities for each wavelength and physical point, and its calculation requires the knowledge of the physical structure of the medium. In the case of pure scattering, eq. (2.20) is all that has to be solved, whereas pure emission has to be accounted for additionally as will be discussed in next subsection.

This scheme can be generalized to spherical symmetry and to the special relativistic case, additional complexity arising from the following effects:

- In moving atmospheres, the radiative transfer equation left and right term are differ-

ent: the left hand side term is more naturally expressed in the observer rest frame where the wavelength of a specific intensity beam is constant, while the opacities and source function are more naturally expressed in the comoving frame where scattering is isotropic. Any chosen frame will therefore need to transform part of the equation, increasing its complexity.

- Taking into account scattering requires information on beams coming from all directions, so that the Λ_ν operator must sample the θ or μ parameter even in 1D.

- The calculation of the Λ_ν matrix coefficients is always time consuming since it contains lots of exponentials which are costly in computer time.

2.1.3 The rate equation

We mentioned that even if the level populations were perfectly known, the source function would still have to be calculated because it depends on the energy density J_ν through scattering. But usually the level and ionization populations are not known *a priori* and have to be calculated by solving the **rate equation**.

In this section, J_ν and the temperature structure are supposed to be known. As this if often not the case, the resolution then uses a nested iteration scheme, solving the radiative transfer equation to get the temperature and the energy density, and the rate equation to find the level and ionization populations needed to calculate the opacities and emissivities. The temperature structure also depends on the radiation field and therefore must be corrected, which is usually done by enforcing the energy conservation between different physical layers.

If we assume statistical equilibrium, the general rate equation for level population reads:

$$\frac{dn_i(\mathbf{r})}{dt} = \sum_{j\neq i}^{N} n_j(\mathbf{r}) P_{ji}(\mathbf{r}) - n_i(\mathbf{r}) \sum_{j\neq i}^{N} P_{ij}(\mathbf{r}) = 0 \tag{2.22}$$

with n_i the population of a particular level, N the total number of levels, and P_{ij} the transition rates between level i and level j. This equation has to be supplemented by the charge conservation equation and the nucleus conservation equations. The electron density if found from the generalized equation of state.

This problem can then be addressed either assuming **L**ocal **T**hermodynamic **E**quilibrium, denoted **LTE**, or in the more general **N**on **L**ocal **T**hermodynamic **E**quilibrium case, denoted **NLTE**.

- **LTE:** In this approximation, the level and ionization populations are assumed to follow the $Saha - Boltzmann$ equation. This assumption holds of course in Thermal Equilibrium, but is also a good approximation when collisional rates are preponderant, since the level populations and atom ionizations are then dominated by the matter velocity distribution, i.e. the temperature structure. Two sub classes of LTE approximations exist:

  - The **pure LTE**, where thermal equilibrium really holds locally with the direct consequence that the source function is a Planck function with the local matter temperature:

$$S_\nu(\mathbf{r}) = B_\nu(T(\mathbf{r})) \tag{2.23}$$

  - The "**LTE-ϵ**" approximation where the atom level populations and ionizations are supposed to follow the Saha-Boltzmann equation but where the part of the source function corresponding to the lines is allowed to depart from the Planck function in order to take into account coherent line scattering. In this case

$$S_\nu = (1-\epsilon)J_\nu + \epsilon B_\nu \tag{2.24}$$

    where ϵ is the so called *thermalization factor*. Obviously, if the pure LTE approximation holds, $\epsilon \sim 1$. Allowing ϵ to be different than one *for the lines* allows to take into account line scattering which is important for spectrum formation, pure scattering corresponding to the $\epsilon = 0$ case. This equation is the one we missed in the previous section once we had defined the Λ_ν operator. Here $(1-\epsilon)J_\nu$ accounts for the line scattering, and ϵB_ν for thermal emission of the element lines. For all other processes $\epsilon = 1$. In our LTE calculations we usually use $\epsilon \sim 0.05$, making the line source function dominated by scattering. In NLTE, the ϵ factor is not needed, but can be estimated, and has been shown to always be $\epsilon \approx 10^{-7}$ for ion

lines in SNeIa around maximum light.

- **NLTE:** In this more general case, the atomic levels and atom ionizations are not supposed to follow the Saha-Boltzmann equation, and the radiation field is allowed to depart completely from the thermal equilibrium with matter. The complete rate equation has therefore to be solved, taking into account the radiative and collisional transition rates, and their relation with the radiative field. NLTE ionization effects can also be taken into account using generalized partition functions. Whereas in **LTE** the levels are related by Boltzmann statistics, one now has to account for each possible transition rate between any considered levels, which results into a dramatic increase of the calculations needed (68 levels for HeII, 13675 for FeII).

2.1.4 Level populations

LTE:

In LTE, the problem to solve is simpler, and computationally less costly than in NLTE. In thermodynamic equilibrium at temperature T with an electron pressure P_e, the atoms are distributed over their bound levels according to Boltzmann statistics. The number $N_{r,s}$ of atoms in excitation state r of ionization state s ($s = 0$ for neutral atoms) compared to the total number N_s of atoms in ionization state s is accordingly:

$$\frac{N_{r,s}}{N_s} = \frac{g_r e^{-\chi_r/k_B T}}{Q_s(T, P_e)} \tag{2.25}$$

where k_B is Boltzmann's constant, Q_s the partition function and χ_r the excitation energy relative to the ground-state configuration of ionization state s. Between two ionization states, the Saha equation has to be used, and reads:

$$\frac{N_{s+1}}{N_s} = \frac{(2\pi m)^{3/2}(k_B T)^{5/2}}{h^3 P_e} \frac{2 Q_{s+1} e^{-\chi_{s,s+1}/kT}}{Q_s} \tag{2.26}$$

with $\chi_{s,s+1} =\mid \chi_s - \chi_{s+1} \mid$, the energy difference between the ionization states s and $s+1$.

The solution must fulfill the constraints of particle (total and for each element) and

charge conservation:

$$N_{\mathrm{tot}} = \sum_{r,s,i} N_{r,s,i} \tag{2.27}$$

$$\epsilon_i N_{\mathrm{tot}} = \sum_{r,s} N_{r,s,i} \tag{2.28}$$

$$N_e = \sum_{r,s\neq 0,i} N_{r,s,i} \tag{2.29}$$

where ϵ_i denotes the abundance of the element i, N_{tot} the total number of particles, and N_e the total free electron number.

It can be shown that this set of equations is equivalent to a single non-linear equation for the free electron number N_e. In LTE one then just has to solve this single equation to get the level populations and ionization level.

NLTE:

In NLTE, the general rate equation (2.22) has to be solved with the transition rates taking into account the radiative as well as the collisional rates:

$$P_{ij} = R'_{ij} + C'_{ij} \tag{2.30}$$

with R'_{ij} the radiative transition rate between level i and level j and C_{ij} the collisional rate associated to the same levels.

For calculation purposes we change from the R' and C' probability transitions previously defined. We note the upward transition rates $(i \rightarrow j)$, $n_i R_{ij}$ and $n_i C_{ij}$. We also note the downward transition rates $(j \rightarrow i)$, $n_j(\frac{n_{i^*}}{n_j^*} R_{ji})$ and $n_j(\frac{n_{i^*}}{n_j^*} C_{ji})$, where n_i^* is the LTE population of level i computed from the actual number densities of the ground state of the next ionization stage of the element and the electron density[4]. Finally, the κ subscript denotes the continuum.

Still assuming $\frac{dn_i}{dt} = 0$ we can now write the complete rate equation for each bound state

[4]It is usually a good approximation to consider that free electron are thermalized with the matter, i.e. the atoms, since they are are at least three order of magnitude lighter.

i of each ionization stage of each chemical specie in the material:

$$\begin{aligned}
&\sum_{j<i}^{\kappa} n_j \left(R_{ji} + C_{ji}\right) \\
&\quad -n_i \left\{ \sum_{j>i}^{\kappa} \left(R_{ij} + C_{ij}\right) + \sum_{j<i}^{\kappa} \left(\frac{n_j^*}{n_i^*}\right) \left(R_{ij} + C_{ji}\right) \right\} \\
&\quad + \sum_{j>i}^{\kappa} n_j \left(\frac{n_i^*}{n_j^*}\right) \left(R_{ji} + C_{ij}\right) = 0.
\end{aligned} \tag{2.31}$$

The collisional rates C_{ij} are given by $C_{ij} = \omega_{ij} N_e$, where ω_{ij} is a function of T tabulated or calculated for each level of the considered model atom. The radiative rates for the lines are given by

$$R_{ij} = B_{ij} \bar{J}_{ij} \tag{2.32}$$

$$R_{ji} = A_{ji} + B_{ji} \bar{J}_{ij} \tag{2.33}$$

$$\bar{J}_{ij} = \int_0^{\infty} \phi_{ij}(\lambda) J(\lambda)\, d\lambda \tag{2.34}$$

Here A_{ji}, B_{ji} and B_{ij} are the Einstein coefficients for the transition $i \rightarrow j$ and $\phi_{ij}(\lambda)$ is the normalized line profile function for this transition.

The radiative rates for the bound-free transitions are given by

$$\begin{aligned}
R_{i\kappa} &= \tfrac{4\pi}{hc} \textstyle\int_0^{\infty} \sigma_{i\kappa} \lambda J(\lambda)\, d\lambda \\
R_{\kappa i} &= \left(\tfrac{n_\kappa}{n_i}\right)^* \tfrac{4\pi}{hc} \textstyle\int_0^{\infty} \sigma_{i\kappa} \lambda \left[\tfrac{2hc^2}{\lambda^5} + J(\lambda)\right] \exp\left(-\tfrac{hc}{k\lambda T}\right)\, d\lambda
\end{aligned} \tag{2.35}$$

were $\sigma_{i\kappa} = \sigma_{i\kappa}(\lambda)$ denotes the photo ionization cross-section from level i to the continuum state κ. There is one equation per level, which means that if the charge conservation equation is added for the continuum level population, the system is closed, i.e. it gives one independent relation per unknown.

Finally, this set of equation can be compactified to operator notation, with n the level

populations vector, including each chemical species level, and ionization stage as well as the continuum, and R the rate operator containing all the transition probabilities and defined as follows:

$$R_{ij} = [R_{ij}][n] \tag{2.36}$$

Solving the rate equation is numerically costly since it is non linear for the electron number as well as for the level population numbers. Still, if one manages to solve the rate equation, in NLTE[5], it becomes possible to calculate the opacities needed to solve the radiative transfer equation scattering problem.

2.2 SYNOW

We shall now present the two codes we used, starting with the parameterized radiative transfer code SYNOW which takes full advantage of the simplifications specific to the supernovæ case.

2.2.1 SYNOW approximations

Spherical symmetry: SYNOW assumes spherical symmetry to solve the 1D spherical radiative transfer equation. This is well supported by the low polarization ($\approx 1\%$) of SNeIa spectra . In order to correctly treat scattering, $\mu = cos(\theta)$ previously defined is sampled.

Sobolev approximation: This approximation takes advantage of the large velocity gradient present in SNeIa. If one considers an element presenting a line at λ_0 in its rest frame, at velocity v_{obs} toward the observer, this element will present a non negligible opacity in the observer rest frame at $\lambda = \lambda_0(1 + \frac{v_{obs}}{c})$, assuming that the first order Doppler shift formula holds.

The element line is then said to be in resonance at the wavelength λ. This resonance will extend on a zone of velocity width Δv, where $\frac{\Delta v}{c} = \frac{\Delta_{\lambda_0}}{\lambda_0}$, Δ_{λ_0} standing for the line profile width.

[5]depending on his time or his resistance against adversity

In the Sobolev approximation, this zone, called the resonance zone, is assumed to be small enough to consider its velocity and all the relevant physical parameters (temperature, level populations, etc) as constant. The source function of the line at the wavelength λ, as well as its optical depth at the same wavelength are therefore given by their resonance region values, without having to integrate over the whole extension of the atmosphere: the Sobolev approximation changes S_ν and τ_ν into local quantities.

We can now derive the equation for the specific intensity emergent from a resonance region centered on s_* where s is the beam path coordinate (cf Jeffery & Branch, 1990) for a resonance wavelength λ_* in the same way as in eq. (2.17):

$$I(\lambda_*, \mathbf{n}, \infty) = I(\lambda_*, \mathbf{n}, -\infty)e^{-\tau} + S(\lambda_*, \mathbf{n}, s_*)(1 - e^{-\tau}) \tag{2.37}$$

In this equation $I(\lambda_*, \mathbf{n}, -\infty)$ is the incident specific intensity, and τ the optical depth calculated on the resonance region. $S(\lambda_*, \mathbf{n}, s_*)$ is the source function evaluated in the resonance region.

In the Sobolev approximation, multiple resonance regions are also considered to be at infinity relative to each other in wavelength space. The previous equation is then easily generalized to more than one line:

$$I(\lambda_*, \mathbf{n}, \infty) = \sum_{i=1}^{N} S(\lambda_*, \mathbf{n}, s_i)(1 - e^{-\tau_i}) + I(\lambda_*, \mathbf{n}, -\infty)e^{-\sum_{i=0}^{N}\tau_i} \tag{2.38}$$

Transforming the source function and the optical depth into local quantities has simplified the solution of the radiative transfer equation, but the Sobolev approximation does not hold for overlapping resonance regions, which is for instance the case for elements with numerous close lines, such as the iron group elements. This will prove important later on, when the flux transfer issue will be addressed.

Photospheric model SYNOW also assumes the photospheric model, which considers the supernova to be formed of an opaque region with a black body spectrum called the *photosphere*, on top of which lie some scattering elements. This model has long been thought to well describe SNeIa around maximum, when their central part is supposed to be very

dense and hot. It therefore presents a very high continuum opacity from the free electrons coming from the ionized material. The photosphere is assumed to be optically thick enough for the radiative field to be thermalized with the matter, and thus to be well described by a black body spectrum. We found the situation to be more complex, and will address this issue in later chapters.

Boltzmann level population In SYNOW, the rate equations are not solved. Each element is considered to be at a fixed excitation temperature, its lines weights being scaled with respect to a given reference line optical depth at the photosphere surface, using the Boltzmann level equation. Each optical depth decreases from the photosphere toward the outside of the supernova, as $(\frac{v}{v_{phot}})^{-n}$, with n empirically chosen to be $n = 7.5$, v_{phot} being the photospheric velocity. This is a stronger approximation than LTE, for which LTE is of course a prerequisite.

It is also possible in SYNOW to *detach* lines, i.e. to have their optical depth to be maximal at $v > v_{phot}$. In this case their optical depth is considered to be zero between the photosphere and the velocity of their maximum.

2.2.2 P-Cygni profiles

All these simplification make SYNOW a fast code, and allow to simulate the geometrical effects of many different element distributions. If one is well aware of the underlying hypotheses, SYNOW is a powerful tool for line identification.

In the photospheric approximation, the main geometrical effect of line scattering is the characteristic spectral feature called a P-Cygni profile. Figure 2.2 displays the geometrical structure of the photospheric model. The *line forming region* is the zone lying on top of the photosphere. We will first suppose that it contains only one element scattering light at a single wavelength λ_0 in its rest frame. In the zone in front of the photosphere with respect to the observer, called the *absorption zone*, the scattering results in a decrease of the incoming flux from the photosphere, as was seen in eq. (2.17) or eq. (2.37), $I(\tau_{-\,\mathrm{inf}}, \mu, \nu)$ being here the black body photospheric intensity. Since all the matter in front of the photosphere is going toward the observer, the resulting absorption feature will be blue shifted with respect

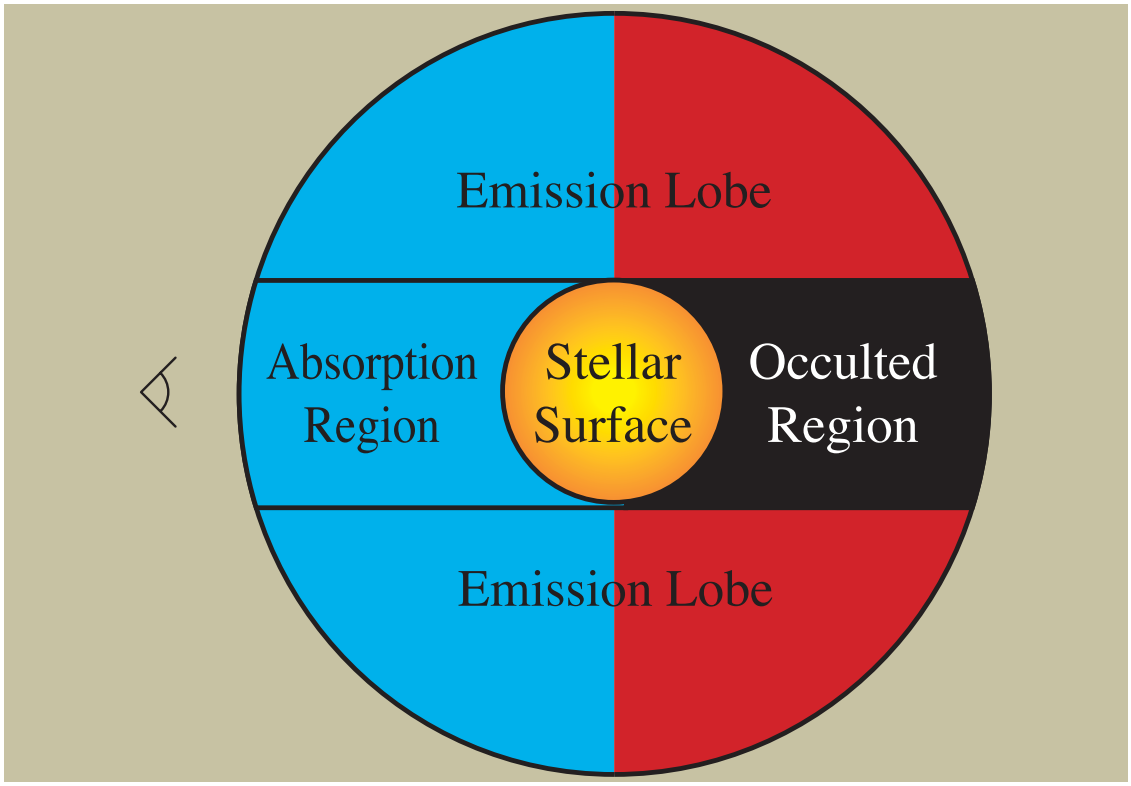

Figure 2.2: *Geometry resulting in a P-Cygni line profile. In this simplistic picture, the extended line forming region above the stellar surface is optically thin to continuum radiation, but is optically thick to line radiation. The far side of the emission lobe is moving away from the observer (at the left), resulting in an emission feature extending to the red of the rest wavelength of the line.*

to λ_0.

In SYNOW, the matter lying behind the photosphere, i.e. in the *occulted region*, affects the spectrum only through multiple scattering, which results in a a negligible contribution to the total flux. On the other hand, in more detailed simulations, this zone has an important if indirect effect on the overall spectrum because of the non locality of the problem: it should not be thought of as equivalent to an empty region.

The side lobes also scatter the light emitted by the photosphere. The corresponding case in eq. (2.37) or eq. (2.17) would be a null incoming flux. The observer will still see the source function contribution, i.e. the light scattered in his direction by the line. Since these lobes are often very large, the amount of light scattered toward the observer usually outweighs the photospheric intensity, resulting in an emission peak centered on the rest wavelength of

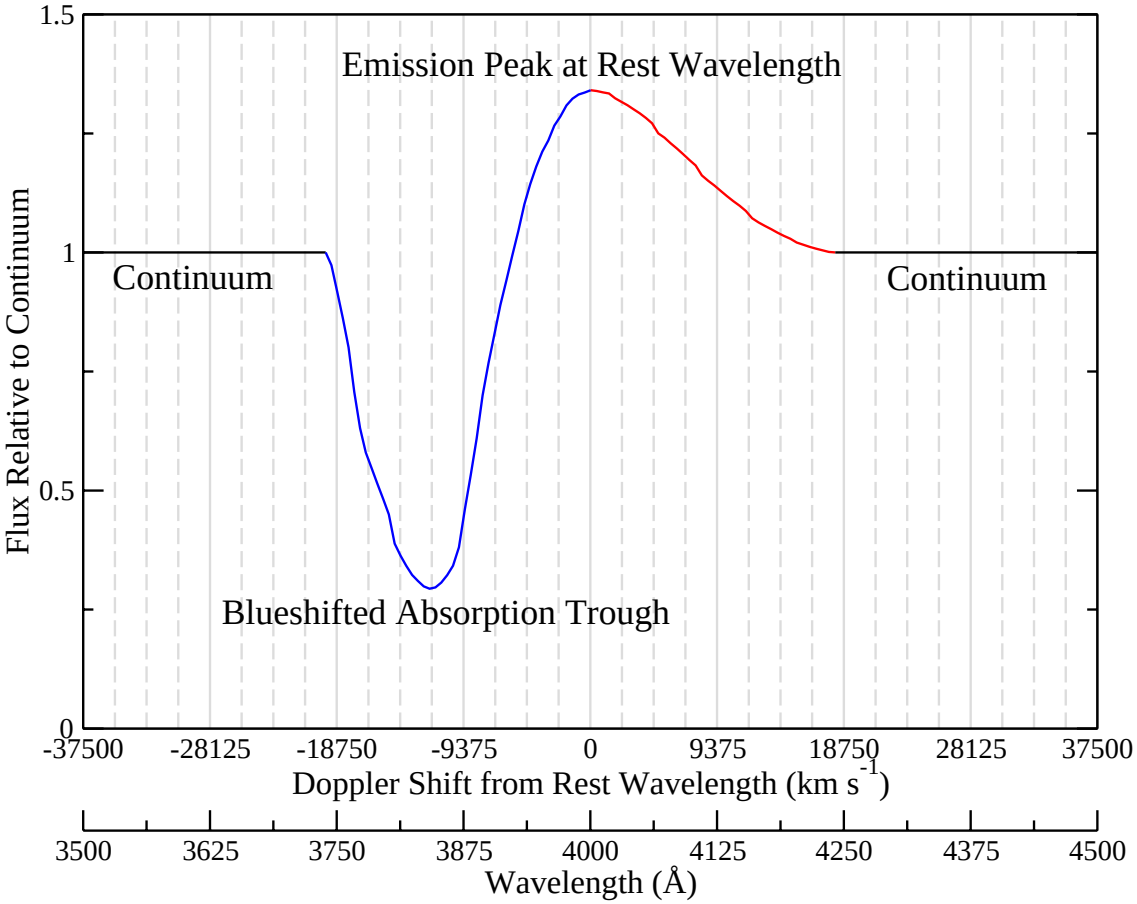

Figure 2.3: *Schematic P-Cygni line profile. The blueshifted absorption trough comes from material blocking the core of the object, expanding toward the observer. The emission feature is peaked at the rest wavelength, and results from light scattered toward the observer.*

the scatterer by geometrical symmetry of the emission lobes.

The sum of the contributions of the different regions results in the characteristic P-Cygni profile displayed in Fig. 2.3 If there is more than one scattering line in the line forming region, which is usually the case, the resulting feature is *not* the linear combination of each line resulting P-Cygni profile. Instead, lines blend together, which is where SYNOW proves useful: by an iterative manual process one can fit supernovæ spectra using different sets of elements. It then becomes possible to infer precious information on the elements present in the line forming region[6].

[6]This is how the most well known SNIa explosion model W7 was devised: using SYNOW to iterate on its outcome in order to tune the flame velocity

2.3 PHOENIX

PHOENIX, the other radiative transfer code we used, is mainly developed by P.Hauschildt, F. Allard, and E.Baron. It is designed to be a general non-LTE stellar atmosphere code. As such it has as few physical assumptions as possible, and can be used to simulate very different objects and has been used to compute synthetic spectra for, e.g., novæ, supernovæ of many types, M and brown dwarfs, O to M giants, white dwarfs and accretion disks in Active Galactic Nuclei.

PHOENIX solves the 1D spherical time independent radiative transfer equation in the relativistic case, and solves the rate equations in NLTE. Note that PHOENIX only neglects the *explicit* time dependence, since it has been shown in Baron et al. (1996) that its effects are of smaller order than all the special relativistic effects.

The cost of this lower degree of parameterization compared to simpler codes like SYNOW, are increased computing power requirements. The output on the other hand is much more than a spectrum, also containing the converged physical structure of the simulated type Ia supernova.

In the PHOENIX mode we used, the input is an abundance structure with respect to velocity, given by an explosion code. We mainly used the W7 model, and did not consider the abundance set as free parameters. The only free parameters were the bolometric luminosity of the supernova, and the time after explosion.

2.3.1 Radiative transfer equation solution in PHOENIX

The radiative transfer equation can be solved with a number of different methods. PHOENIX uses the operator approach described previously, in the 1D spherical relativistic case. It can also be expressed in the form of eq. (2.20) but with a more complicated Λ operator. Directly inverting this equation requires too large amounts of CPU time and memory. Instead, PHOENIX uses the so called "Accelerated Lambda Iteration" method (ALI), developed on the philosophy of operator perturbation. It consists in splitting the Λ operator by introducing an appropriate operator Λ^*, rewriting eq. (2.20) as:

$$\Lambda = \Lambda^* + (\Lambda - \Lambda^*) \tag{2.39}$$

Example of the LTE case

PHOENIX is designed to solve the full NLTE problem, but since most of the PHOENIX models presented in this work where calculated in LTE we exemplify the radiative transfer equation solution in the LTE-ϵ approximation.

The iterative solution using a fixed point iteration scheme is presented in eq. (2.40) for the atomic line part of the LTE case:

$$J_{new} = \Lambda S_{old} \quad , \quad S_{new} = (1-\epsilon)J_{new} + \epsilon B \tag{2.40}$$

At large optical depth in scattering dominated atmospheres like in SNeIa, $\epsilon << 1$ and $S \approx J$. The change per iteration, i.e. the convergence speed, $\Delta S = S_{new} - S_{old}$ is thus small. Physicaly, the reason is that Λ follows photons in its propagation of correction per step since it transfers the old S in to a new one using J. Therefore the corrections propagate by $\Delta\tau = 1$ steps just as photons do. As the thermalisation depth is of order $1/\sqrt{\epsilon}$, it needs many more iteration to converge than to reach the $\Delta S/S << 1$ point. This is mathematically similar to say that the Λ operator has an eigenvalue spectrum close to unity for large optical depth.

In the ALI method, the Λ_* operator is chosen to have smaller eigenvalues than the operator Λ. Rewriting the iteration scheme as

$$J_{new} = \Lambda^* S_{new} + (\Lambda - \Lambda^*) S_{old} \tag{2.41}$$

Or equivalently as

$$[1 - \Lambda^*(1-\epsilon)]J_{new} = J_{fs} - \Lambda^*(1-\epsilon)Jold \tag{2.42}$$

will then increase the convergence. In the last equation $J_{fs} = \Lambda S_{old}$ is the formal solution for the energy density.

PHOENIX implements this ALI method, calculating a tri-diagonal (or larger band-width, up to the full operator) Λ^* operator, solving equation (2.42) for the new values of J, and then using them to compute the new source function S, with eq. (2.40) in the LTE case, for the next iteration cycle until convergence for each wavelength and physical point.

2.3.2 Rate equation in PHOENIX

Once the scattering problem converged for a first guess of the level populations, PHOENIX solves the rate equations, either in the LTE approximation (by a call to the EOS) or in non-LTE for a desired set of atomic levels.

In LTE, the level populations are calculated using the Saha-Boltzmann equation. It has to be noted that this LTE approximation is not the stronger LTE approximation where the radiation is considered in full local equilibrium with the matter.

In NLTE mode, PHOENIX solves eq. (2.37) with the sums extended over all the included levels of the considered model atoms. The weaker radiative transitions are treated as LTE background opacities.

As for the radiative transfer equation, an ALI method accelerates eq. (2.36) iterative solution, since the direct inversion of such a system would be too costly in CPU time and memory.

The rate equation can be rewritten using the "Accelerated Lambda Operator" R^* defined as

$$R_{ij} = [R^*_{ij}][n_{\rm new}] + \left([R_{ij}] - [R^*_{ij}]\right)[n_{\rm old}] \tag{2.43}$$

and built to have eigenvalues much smaller than one. The resulting equation still displays explicit non linearities with respect to the level population n_i and the free electron density n_e, as the coefficients of the $[R^*_{ij}]$ and $[R^*_{ji}]$ are quadratic in n_i, and because of the Saha-Boltzmann factors dependence on the electron density.

The rate equation is linearized replacing the terms $n_{j,new}[R^*_{ji}][n_{new}]$ by $n_{j,old}[R^*_{ji}][n_{new}]$. The resulting increase in the iterations needed to converge the solution is by far outweighed by the removal of the major part of the non-linearities of the rate equation eq. (2.35). But this equation is still non linear with respect to n_e, and still has the high dimensionality of the original system.

$$\sum_{j<i} n_{j,old}[R^*_{ji}][n_{new}] - n_{i,old}\left(\sum_{j<i}\frac{n^*_j}{n^*_i}[R^*_{ij}][n_{new}] + \sum_{j<i}[R^*_{ij}][n_{new}]\right)$$
$$+\sum_{j>i} n_{j,old}\frac{n^*_i}{n^*_j}[R^*_{ji}][n_{new}] + \sum_{j<i} n_{j,new}([\Delta R_{ji}][n_{old}] + C_{ji})$$
$$-n_{i,new}\left(\sum_{j<i}\frac{n^*_j}{n^*_i}([\Delta R_{ij}][n_{old}] + C_{ji}) + \sum_{j>i}([\Delta R_{ij}][n_{old}] + C_{ij})\right)$$
$$+\sum_{j>i} n_{j,new}\frac{n^*_i}{n^*_j}([\Delta R_{ji}][n_{old}] + C_{ji}) = 0 \tag{2.44}$$

To linearize further more, the electron density calculation is separated from the rate equation solution, so that n_e can be considered as given during the rate equation solution. Changes in the electron density are then accounted for in a separate iteration to find a consistent solution of the rate equations and the electron densities.

This resulting scheme only requires the solution of large linear systems and low-dimensional non-linear systems. Moreover, since separate equations are solved for each group of elements, this process can be parallelized, distributing the groups among the available processors allowing PHOENIX to take full advantage of the cluster computing power available nowadays.

Finally, the NLTE effects on the electron density are also taken into account by a modification of the LTE partition functions used to calculate the ionization equilibrium.

2.3.3 Temperature correction

PHOENIX outermost level of iteration is the temperature correction, based on a generalization of the Unsöld-Lucy temperature correction scheme for spherical geometry and NLTE model calculations. It uses the global constraint equation of energy conservation to find corrections to the temperature structure.

PHOENIX supposes the atmosphere to be in local radiative equilibrium, in which case

the energy conservation equation that has to be fulfilled reads:

$$4\pi \int_0^\infty [\eta_\nu - (\chi_\nu - n_e\sigma_e)J_\nu]d\nu = \frac{\dot{S}}{4\pi}, \tag{2.45}$$

where $\dot{S}$ is any external energy source such as gamma-ray deposition or mechanical energy from a wind.

At any given iteration of the temperature correction scheme, the temperature structure is fixed. In each layer the matter temperature is $T(l) = T_{eq}(l) + \Delta T(l)$, where T_{eq} stands for the temperature that would, for the calculated radiation field, fulfill the radiative equilibrium.

It can be shown that to obtain the radiative equilibrium in the relativistic case solved by PHOENIX, the temperature should be corrected so that the Planck function changes by an amount $\delta B(r)$ equal to:

$$\delta B(r) = \frac{1}{\kappa_P}(\kappa_J J(r) - \kappa_P B(r) + \frac{\dot{S}(r)}{4\pi}) - 2\frac{\kappa_J}{\kappa_P}(H(\tau = 0) - H(0)) - \frac{1}{fqr^2}\int_r^R qr^{'}\chi_F(H(r^{'}) - H_0(r^{'})dr^{'}) \tag{2.46}$$

where $H(r) = F(r)/4\pi$. $H_0(\tau)$ is the target luminosity at the particular τ depth point, and q is the "sphericity factor":

$$q = \frac{1}{r^2}e^{\left(\int_{r_{core}}^r \frac{3f-1}{r^{'}f}dr^{'}\right)} \tag{2.47}$$

r_{core} being the inner radius of the atmosphere, R the total radius, and $f(\tau) = K(\tau)/J(\tau)$ the *Eddington factor*, where K, H and J have been defined in eq. (2.2), eq. (2.4) and eq. (2.6).

We also remind that κ_P, κ_J, and χ_J are the wavelength averaged absorptions:

$$\kappa_P = \frac{\int_0^\infty \kappa_\nu B_\nu d\nu}{\int_0^\infty B_\nu d\nu} \tag{2.48}$$

$$\kappa_J = \frac{\int_0^\infty \kappa_\nu J_\nu d\nu}{\int_0^\infty J_\nu d\nu} \tag{2.49}$$

$$\chi_J = \frac{\int_0^\infty \chi_\nu F_\nu d\nu}{\int_0^\infty F_\nu d\nu} \tag{2.50}$$

Using this procedure, PHOENIX corrects the temperature structure and through iteration of the whole process converges a self consistent supernova physical structure.

2.3.4 Summary

The global PHOENIX iteration scheme for the multi-level non-LTE problem solution can be summarized as follows:

- **Set up:** Having a first guess T, n_i, n_e as function of radius, the hydrostatic and hydrodynamic equations are solved with the explosion model abundances to calculate the gas pressure P_{gas}[7].

  1. **Wavelength loop:** Done at fixed n_i, n_e and T for each grid point.
     (a) Iteration over the wavelength loop to solve for the radiative transfer field until J and S are converged to the desired accuracy.
     (b) Update of the radiative rates and rate operators
  2. **Rate equation solution:** Done at fixed J and T for each wavelength and layer point
     (a) Solution of the high dimensionality linear system for the level population n_i
     (b) Solution of the low dimensionality non-linear system for the electron density n_e
  3. **Temperature correction:**
     (a) Correct T to enforce better radiative equilibrium.
     (b) If radiative equilibrium is obtained to desired accuracy, exit the iteration scheme, else start again at the **Wavelength loop**.

- **Converged model:** This converged model can then be used to obtain the spectrum through the calculation of the radiative transfer solution.

[7] In the supernova case, the equation of state procedure, that reads $P_{gas} = f(n_e, T)$ only has to be inverted to find n_e

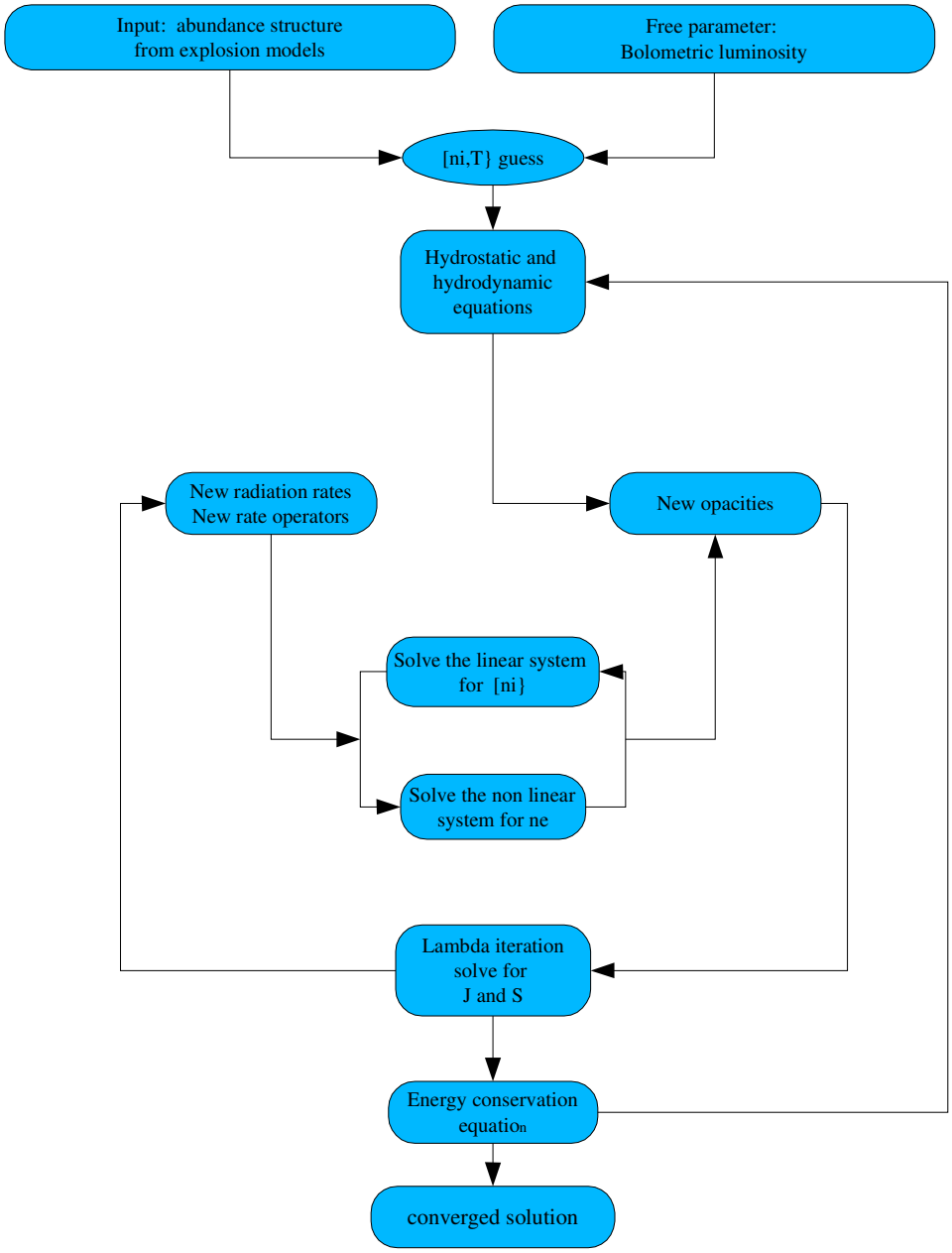

Figure 2.4: PHOENIX *General iteration scheme.*

Chapter 3

Adaptive Grid for PHOENIX

Mathematically, the ALI method used in PHOENIX belongs to the same family of iterative methods as Jacobi or Gauss-Seidel methods. They have the general form:

$$Mx_{n+1} = Nx_k + b \tag{3.1}$$

If we note x_0 the solution of this problem, and if we start with $x_1 = x_0 + \delta x_1$ we have:

$$x_2 = x_0 + M^{-1}N\delta x_1 \tag{3.2}$$

$$\delta x_2 = M^{-1}N\delta x_1 \tag{3.3}$$

which shows that this procedure will converge if the spectral radius of the matrix $G = M_{-1}N$ is lower than unity. Moreover, if in the course of the calculation of x_{n+1} we introduce errors bigger than $\delta x_{n+1} - \delta x_n$, this procedure will fail.

This well known problem of PHOENIX users occurs when an ionization front becomes too poorly spatially sampled. In order to keep PHOENIX convergence time and memory needs within acceptable bounds, we can not use much more than ≈ 100 radial points for the velocity grid, that ranges from 0km.s^{-1} to 30000km.s^{-1}. Since the temperature structure changes in the course of model convergence, the ionization fronts move, and the spacial grid is too coarse to sample them finely enough everywhere.

At ionization fronts the electron density and the species densities vary quickly, making the optical depth and the source function varies accordingly. If the optical depth and source

function changes are too poorly spatially sampled, their interpolation while calculating the formal solution will introduce errors important enough to cause the convergence to fail.

The usual solution to such convergence problems was to provide by hand a new grid with more points at the main ionization fronts. The automatization of this long and tedious procedure has been included in this PhD work.

3.1 The grid density:

The first step of our adaptive grid algorithm is to automatically find the main unsampled ionization fronts, calculating their partial pressure derivatives. We select the three species with the worst sampled partial pressures in order to define the *grid point density function* noted R. Since large electron density variations usually also cause large optical depth or source function variations, we included it to the calculation of R. The number of functions used to calculate R is somewhat arbitrary, but too many would unavoidably degrade the resampling, since the total number of grid points is fixed. Consequently, we selected only three of them.

Once the relevant functions found, we as grid points density function:

$$R = \sqrt{1 + a_1 \left(c_1 \frac{dy_1}{dv} \right)^2 + a_2 \left(c_2 \frac{dy_2}{dv} \right)^2 + a_3 \left(c_3 \frac{dy_3}{dv} \right)^2} \tag{3.4}$$

The coefficients a_1, a_2, a_3 are the relative weights attributed to each one of the three functions. The scaling coefficients c_1, c_2, c_3 are the ratio of the grid span (i.e. the difference between the maximum velocity and the minimum velocity) to the function span (i.e. the difference between the maximum and the minimum of the function). They transform the function derivatives into non dimensional quantities comparable to 1. If $c \frac{dy}{dv} > 1$, the variation is locally more important than the global variation $\frac{\Delta y_{tot}}{\Delta x_{tot}}$, and identically, if $c \frac{dy}{dv} < 1$, the function variation is lower than its average.

Finally the $\frac{dy_1}{dv}$, $\frac{dy_2}{dv}$ and $\frac{dy_3}{dv}$ are the derivatives values of the chosen functions defined as

$$\frac{dy}{dv}(i) = \frac{y(i+1) - y(i)}{x(i+1) - x(i)} \tag{3.5}$$

We preferred this simple choice to spline derivatives in order to ensure computational robustness. Moreover, the natural propensity of splines to amplify variations empirically proved to be a drawback because of the partial pressures sometimes high and narrow peaks, their spline fitting resulting in an artificially too large grid density.

The R function obtained describes the relative grid point density corresponding to the best sampling of the three chosen function variations.

3.2 Adapting the grid

Once the grid point density known, we have to calculate the new grid. The grid point density $R(x)$, x being the grid variable and x_i the i^{th} grid point, satisfies

$$R(x) = \frac{dN}{dx} \tag{3.6}$$

with N the number of grid points.

In order to sample the best the chosen function variations, we want to have an uniform density distribution of points:

$$\frac{dN}{du} = \frac{dN}{R(x)dx} = \alpha \tag{3.7}$$

where α is a constant.

The formal solution of the adaptive grid problem would be to invert the equation set resulting from eq. (3.7), i.e. $N(x) - N(0) = \alpha \int_0^x R(y)dy$.

One possible approach is to tabulate the $R(x)$ integral, and interpolate to find equal mass bins to build the new grid, that will from now on be noted x_i'. Since there is no way to know the large variation zone's location "a priori", this method needs a large number of tabulated points to calculate the new grid accurately in regions of steep $R(x)$. We preferred to this the Voronoi tessellation method, which substitutes an iterative approach to the inversion of the function.

3.2.1 Voronoi tessellation method

Our method takes seed in Cappellari & Copin (2003), where the Voronoi tessellation is used to rebin 2D images. The central Voronoi tessellation is a division of the space into zones enclosing all the closer points to its associated *generator*, defined as the barycenter of the zone. For any given density function $\rho(\mathbf{r})$ the central Voronoi tessellation bins, or zones, are naturally smaller where the density is higher, but the mass in each bin is not constant.

It has been proven in 1D and conjectured in n dimensions (the Gersho conjecture) that if d is the typical size of the central Voronoi tessellation bin, then d and ρ are related by

$$d \propto \rho^{\frac{-1}{2+n}} \tag{3.8}$$

where "density" and "mass" are generic names used for quantities related in n dimension by the relation $m = \rho d^n$.

In 1D the "mass" enclosed in each bin is $m \approx \rho d$, or, using eq. (3.8) $m \approx \rho^{2/3}$. If we define $\rho' = \rho^3$, the associated bin mass, according to eq. (3.8) in 1D will be $m \approx \rho\rho'^{-1/3} = 1$: in the approximation of large number of bins, the central Voronoi tessellation corresponding to ρ' has constant mass zones for the density ρ.

The modified Lloyd method described in Cappellari & Copin (2003) has the central Voronoi tessellation as fixed point. We can then iteratively calculate the grid optimally close to the asymptotic situation of high number of bins we are interested in by using the following procedure:

1. First guess for the grid, noted x_i.
2. Calculate the mass centroids $z(i)$ of each bin using the density $\rho' = R^3$
3. Calculate the new grid $x'(i)$, where the $x'(i)$ are the boundaries of the Voronoi tessellation using the $z(i)$ as generators. The $x'(i)$ points are therefore the middle of the segments $[z(i+1), z(i)]$.
4. Go back to (2) and iterate until the $x'(i)$ don't move anymore.

This simple algorithm is easy to implement in 1D, and the Gersho conjecture makes it

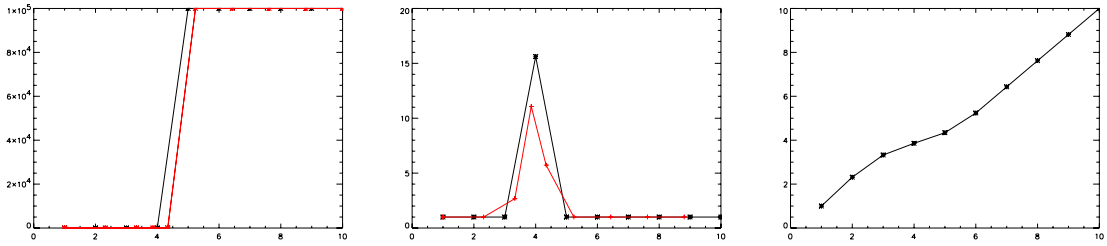

Figure 3.1: ***Left:*** *Step function. In black before the adaptive grid, in red after the adaptive grid.* ***Center:*** *the R function calculated with only this function.* ***Right:*** *New grid in function of the old one.*

generalizable to higher dimensions, which is an interesting feature since 3D PHOENIX is actually in development.

3.3 Tests

3.3.1 Step function

The step function was used to tests if the grid points moved toward the poorly sampled step, but also to ensure that some points remained in the constant zones, since we do not want any large variation to accrete all the grid points.

In our algorithm, the maximal derivative is bound to be lower than $\Delta_{max}f/\Delta_{max}x$, which is not the case with spline derivatives. The uses of spline fits proved not to be a good choice, since it did not include the natural "viscosity"of grid point drift when using the linear derivative. If the real function happens to have a steeper front than detected with the linear derivatives, the next PHOENIX iteration will show it, and our adaptive grid algorithm will continue to drag points toward this zone.

Fig. 3.1 displays the case of a step function. The right hand side picture shows that grid points are dragged toward the discontinuity without totally depleting the constant zones as expected. Moreover, the left hand side function shows that since we use two point logarithmic interpolation when possible, the error on the resampled function is less than it would be with a simple linear interpolation.

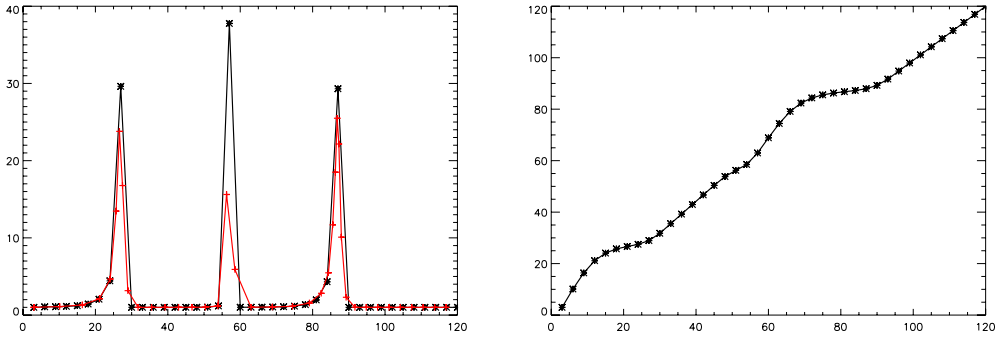

Figure 3.2: ***Left:*** *R function calculated with 3 tangent functions. In black before the adaptive grid, in red after the adaptive grid.* ***Right:*** *The new grid in function of the new one.*

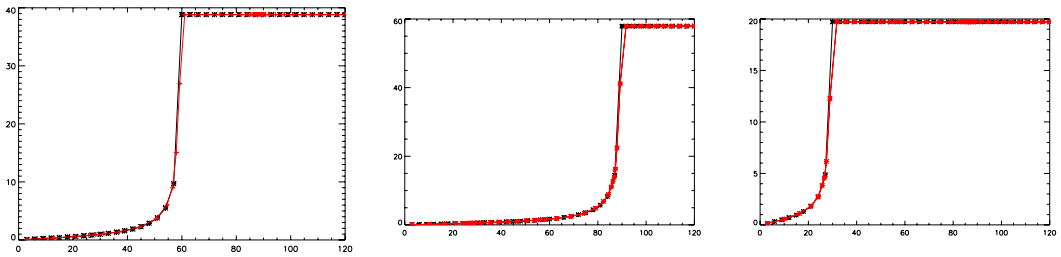

Figure 3.3: *The three "tangent" functions used.*

3.3.2 Multiple functions

To test how this procedure worked with different functions, we chose three tangent functions peaking at different points. The adaptive grid procedure needed 364 iterations to converge the new grid, using a negligible amount of CPU time, showing that the grid adaptation will be possible at each PHOENIX iteration.

In Fig. 3.2 we display the R function and the new grid obtained plotted in function of the new one. The relative heights of the peaks only depend on the slope and not on the absolute values of the functions, as expected. The right hand side of the figure shows that the points are dragged toward the large derivative zones, again without depleting the constant regions.

3.4 Adaptive grid in PHOENIX

3.4.1 Test on a converged model

Once the adaptive grid procedure was shown to work, we integrated it into PHOENIX. We implemented the automatic quickly varying function detection following what has been previously explained.

As a first test we ran 10 iterations on an already converged model. In Fig. 3.4, Fig. 3.6, and Fig. 3.5 we display the partial pressures of the most important species found: electrons, CII and OII.

As expected the electron pressure has a steady decreasing slope with increasing velocity, causing more points to be dragged toward the inside of the supernova. This function is not redundant with partial pressures, since its main variation results from density and temperature variation more than from drastic ionization changes.

OII and CII partial pressure display steep slopes and large peaks that are a combination of ionization and density effects. We display in Appendix I section 8.2 the abundance profiles of W7 model, which already show thin large peaks. But differentiating between both effects is not crucial as what impacts on the optical depth and source functions are the partial pressures of the chemical species.

The red curves and points are *not* the interpolation of the black curve on the new grid: they are the electron pressure after the next PHOENIX calculation on the new grid. The left hand side figures for electron, OII and CII partial pressures show that more points are indeed added where the steep variations of these functions are. Moreover, these figures also show the large changes the re-griding can have on a new PHOENIX iteration. It is hard to predict how strongly these changes will impact the spectrum. The variation due to the electron pressure occurs deep inside of the supernova where the mean continuum optical depth is between 0.6 and 1.5. As all continuum opacity source directly depend on the free electrons abundance, this change will repercute on the mean opacity in a physical region where $\tau \approx 1$, i.e. where it's effect on the spectrum formation should be large.

The center and right hand side figures show that after the first large change, the grid and the calculated functions stabilize.

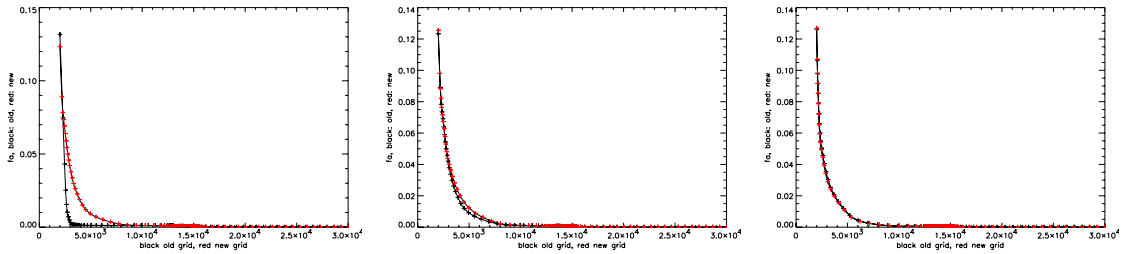

Figure 3.4: *Electron pressure, grid evolution: first, second, and tenth iteration. Black is the starting point of the iteration, red is the next calculation result done on this new grid.*

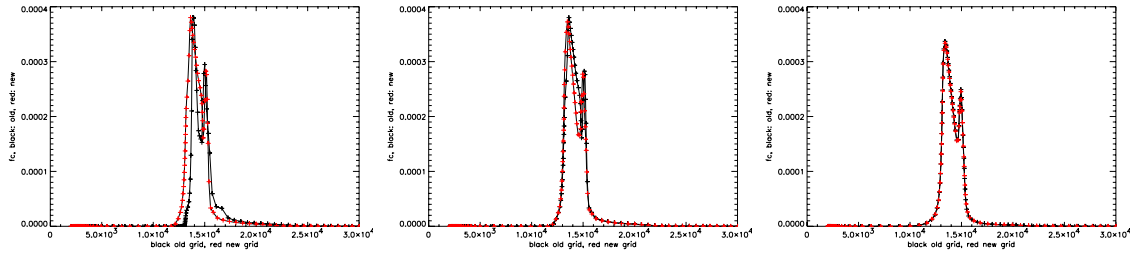

Figure 3.5: *OII ionization front, grid evolution: first, second, and tenth iteration Black is the starting point of the iteration, red is the next calculation result done on this new grid.*

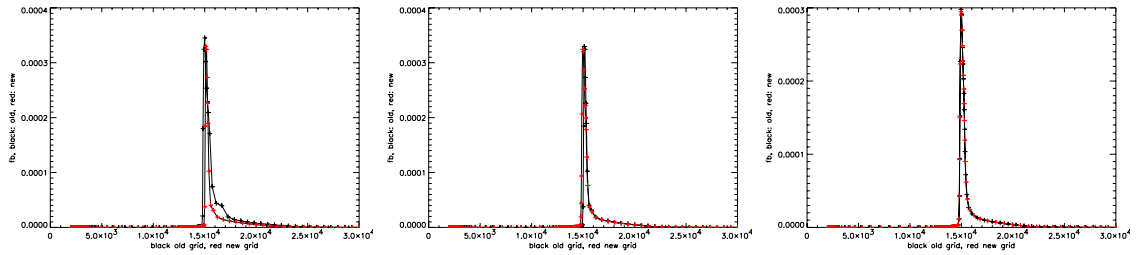

Figure 3.6: *CII ionization front, grid evolution: first, second, and tenth iteration Black is the starting point of the iteration, red is the next calculation result done on this new grid.*

The adaptive grid method we developed detects automatically the larger partial pressure gradients, and the grid accordingly adapted. The calculation time added to a PHOENIX iteration is negligible, and the grid convergence was robust to steep slopes. The grid change did not deplete the regions where the chosen functions leading the regriding do not vary much. We where able to run over 10 PHOENIX iterations on different models. The larger ionization fronts where always detected and the ionization structure changes coming from the regriding always stabilized, which was not *a priori* obvious.

Chapter 4

Colors and Arnett law

4.1 Arnett's law

In a series of papers, D. Arnett presented a parameterized approach of SNeIa light curves of SNeIa based on the assumption that the density and the opacity could be written as:

$$\rho(\mathbf{r},t) = \rho(0,0)\eta(x)\left(\frac{R(0)}{R(t)}\right)^3 \quad (4.1)$$

$$\kappa(x) = cte \quad (4.2)$$

following Arnett (1982) notations, the mean free path of the photons being $\lambda = \frac{1}{\kappa\rho}$, and $x = \frac{r}{R(t)}$, a dimensionless radial coordinate which follows the expansion of the matter. D.Arnett also assumes :

1. *Homologous expansion*

2. *Radiation pressure dominant*: the equation of state is therefore $E = aT^4V$, $P = \frac{E}{3V}$.

3. *Presence of* ^{56}Ni with a distribution *somewhat peaked toward the center of the ejected mass*[1].

[1] from D.Arnett himself

He then uses the first law of thermodynamics and the Eddington diffusion approximation to calculate the energy balance:

$$\dot{E} + P\dot{V} = -\frac{\partial L}{\partial m} + \epsilon \tag{4.3}$$

$$\frac{L}{4\pi r^2} = -\left(\frac{\lambda c}{3}\right)\frac{\partial (aT^4)}{\partial r} \tag{4.4}$$

where ϵ is the energy release per unit mass from radioactive decay and $\lambda = \frac{1}{\rho\kappa}$ is the mean free path of the photons.

From there D.Arnett derives a separable differential equation on the temperature, rewritten as:

$$T(\mathbf{r},t)^4 = \psi(x)\phi(t)T(0,0)^4\left(\frac{R(0)}{R(t)}\right)^4 \tag{4.5}$$

where $x = \frac{r}{R(t)}$ is a dimensionless radial coordinate which follows the expansion of the matter.

Coupling the opacity decrease due to the expansion through the density evolution, and the energy deposition through ^{56}Ni and ^{56}Co decay, D.Arnett is able to devise a function that reproduces the temperature, and thus the luminosity evolution of type Ia supernovæ around maximum light:

$$L = \epsilon_{Ni} M_{Ni} \Lambda(x,y) \tag{4.6}$$

$$\Lambda(x,y) = e^{(-x^2)}\int_0^x e^{(-2sy+z^2)} 2z dz \tag{4.7}$$

with $x = t/\tau_m$, $y = \frac{\tau_m}{2\tau_{Ni}}$, $\tau_m = 2\tau_0 R(0)/v_{sc}$ and τ_{Ni} is the mean half life of ^{56}Ni. The total mass of nickel is denoted M_{Ni} and ϵ_{Ni} is the energy of radioactive decay of ^{56}Ni per unit mass divided by the mean life time τ_{Ni}. This luminosity function has been shown to reproduce SNeIa blue light curve shape, including the universality of the Phillips relation (Arnett (2001)).

In order for the diffusion approximation to hold, the optical depth must be of order $1/\epsilon$, where ϵ is the thermalization factor. Given $\epsilon \approx 0.05$, the overall shape of the spectrum forms deep inside of the supernova where the FeIII lines have been shown to blend and form a large optical depth zone. As the opacities of the iron lines are larger in the $\lambda > 5000$Å wavelength

region, the D.Arnett approximation is expected to work better for the B and V band than for larger wavelength.

4.2 PHOENIX & real supernovæ colors

The PHOENIX line list has been extended in 2004, to improve the accuracy of the computed opacities. As the overall shape of the spectrum is dominated by the numerous iron line blends at the epochs we simulated, the new set of lines will result into an improved matching of the simulated colors to the observed ones.

To compare PHOENIX results to reality we used real supernovæ colors published in Hamuy et al. (1996) and we calculated the UBVRI PHOENIX simulated spectra colors using the same filters. The color calculation was done by a simple integration including the filters transmission function.

The list of the Calan Tololo survey supernovæ we used (called CTIO supernovæ from now) and their luminosities can be found in table 4.1. We also used the ones published in Phillips (1993) which luminosities are listed in tab. 4.2.

As PHOENIX does not include the time evolution of the light curve, it is not possible to relate self consistently the different epochs of our simulations. In the following we will compare real supernovæ magnitudes to PHOENIX magnitudes for each of the luminosity sequences we simulated. For this purpose and in order to study the spectral formation in SNeIa, we converged a grid of LTE PHOENIX simulations sampling the luminosity and date within the W7 model. We simulated day 10, day 15, day 20 and day 25 after maximum light luminosity sequences with bolometric luminosities ranging from -18.0 to -19.7, and the complete grid can be found in appendix 8.2

4.3 Comparison with reality

We display in the left hand side of Fig. 4.1 the V band magnitude of all the spectra of our grid as well as the CTIO ones. In the right hand side of the same figure we display B versus R magnitudes calculated on the same PHOENIX spectra compared to the R colors of the supernovæ listed in tab. 4.2. Fig. 4.2 displays the CTIO and the PHOENIX I versus B

name	mB	mV	mI	Δ_{m15}	*name*	mB	mV	mI	Δ_{m15}
90O	-19.40	-19.41	-19.02	0.96	92bk	-19.03	-19.03	-18.83	1.57
90T	-19.17	-19.21	-18.98	1.15	92bl	-19.13	-19.13	-18.85	1.51
90Y	-18.56	-18.89	-18.65	1.13	92bo	-18.76	-18.77	-18.65	1.69
90af	-18.95	-19.00	—	1.56	92bp	-19.40	-19.35	-19.03	1.32
91S	-19.24	-19.28	-18.98	1.04	92br	-18.66	-18.70	—	1.69
91U	-19.49	-19.55	-19.37	1.06	92bs	-18.96	-19.03	—	1.13
91ag	-19.40	-19.48	-19.16	0.87	93B	-19.04	-19.16	-18.87	1.04
92J	-18.92	-19.04	-18.78	1.56	93H	-18.45	-18.68	-18.74	1.69
92K	-17.72	-18.46	-18.61	1.93	93O	-19.23	-19.14	-18.91	1.22
92P	-19.34	-19.31	-19.03	0.87	93ag	-19.10	-19.13	-18.81	1.32
92ae	-19.07	-19.18	—	1.28	93ah	-19.28	-19.24	-18.93	1.30
92ag	-18.98	-19.11	-18.98	1.19	37C	-19.56	-19.54	—	0.87
92al	-19.47	-19.42	-19.13	1.11	72E	-19.69	-19.64	-19.26	0.87
92aq	-18.89	-18.99	-18.57	1.46	80N	-18.74	-18.79	-18.53	1.28
92au	-19.03	-19.08	-18.83	1.49	81B	-19.07	-19.17	—	1.10
92bc	-19.64	-19.56	-19.22	0.87	86G	-18.08	-18.43	-18.45	1.73
92bg	-19.36	-19.32	-19.04	1.15	90N	-19.26	-19.28	-19.05	1.07
92bh	-18.89	-18.97	-18.79	1.05	91bg	-16.62	-17.38	-17.81	1.93
92A	-18.43	-18.45	-18.20	1.47	94D	-19.00	-18.96	-18.75	1.32

Table 4.1: *Calan Tololo survey supernovæ* as published in Hamuy et al. (1996)

name	mB	mV	mR	Δ_{m15}	name	mB	mV	mR	Δ_{m15}
71T	-17.2	-17.52	—	1.64	90N	-18.74	-18.82	—	1.01
80N	-18.53	-18.58	-18.32	1.28	91T	-18.96	-19.1	-19.04	0.94
81B	-18.47	-18.54	—	1.1	91b	-16.38	-17.13	-17.57	1.88
86G	-17.72	-18.12	-18.21	1.73	92A	-18.05	-18.1	-17.85	1.33
89B	-18.5	-18.5	-18.3	1.31					

Table 4.2: *Phillips supernovæ* from Phillips (1993)

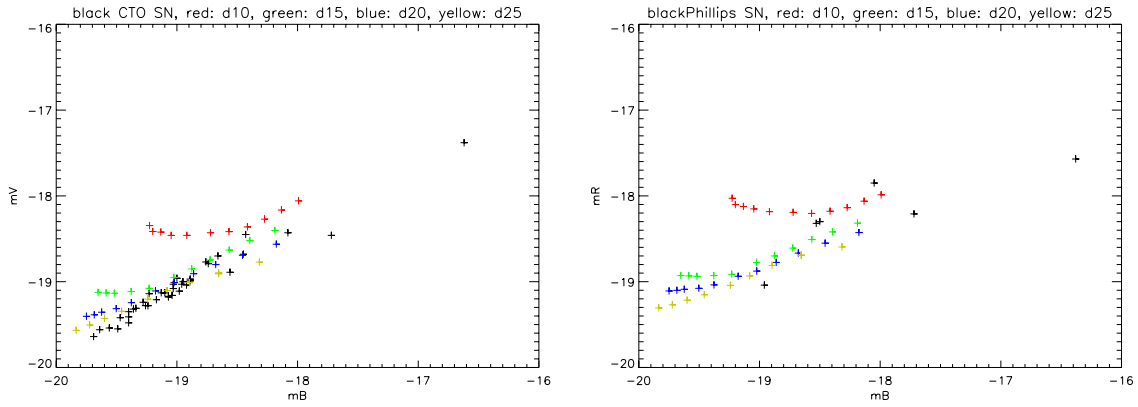

Figure 4.1: ***Left:*** *Calan Tololo supernovæ* M_B *and* M_V *versus* PHOENIX M_B *and* M_V. *Real* SNeIa *in black,* PHOENIX *ones are colored. 10 days after explosion in red, 15 in green, 20 in blue and 25 in yellow.* ***Right :*** *idem but for* M_B *and* M_R

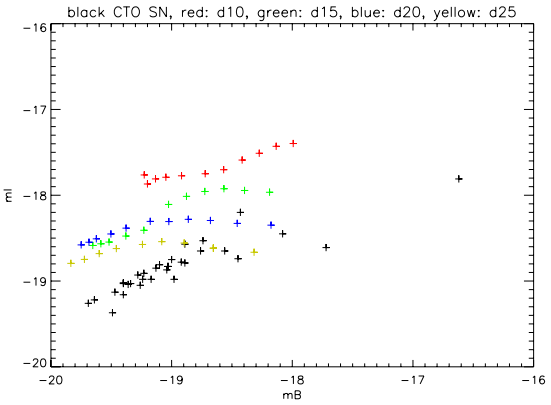

Figure 4.2: *Calan Tololo supernovæ* M_B *and* M_I *versus* PHOENIX M_B *and* M_I. *Real* SNeIa *in black,* PHOENIX *ones are colored. 10 days after explosion in red, 15 in green, 20 in blue and 25 in yellow.*

band magnitudes.

The PHOENIX and real spectra agree for both B vs V and V vs R for dates ranging from 15 days to 25 days after explosion. Day 10 spectra are too blue compared to maximum light real spectra until $M_B > -18.4$. This corroborates the assumption of the maximum light time to be ≈ 20 days after explosion, earlier spectra being expected to be bluer as they correspond to hotter denser objects.

The agreement of 10 days after explosion for lower luminosities can be explained by the cooling driving inwards the region where the overall shape of the spectrum is formed. When it reaches a region with high enough optical depth and of low enough velocity to be insensitive to an ≈ 5 days expansion dilution, the color curves of day 10 and day 15 merge.

Moreover, since day 15 to day 25 after explosion supernovæ have similar colors, probably insensitive to the details of the density profile. In the "multi-layered spectrum formation" picture that will be developed later, with deep layers dominated by iron lines, once their optical depth is $>> 1$ a change of density has little effect on the flux transfer. The colors are more sensitive to a composition change which will modify the opacity distribution with wavelength.

The comparison in the B vs I, Fig. 4.2 shows that the PHOENIX spectra are systematically lacking flux in the I band except at faint luminosities for day 20 and day 25 after explosion. There is a general lack of flux transfer from the blue toward the red in the W7 model. The decrease of the opacity as a function of wavelength is probably too steep. When the flux transfer from the blue toward the red is dominated by Doppler effect on scattering, a steep density decrease would imply a steep optical depth diminution, causing a smaller flux transfer than a shallower one. The agreement with reality of day 25 B vs I for $M_B > -19$ corroborates this explanation. At this later epoch the layer where the overall shape of the spectrum forms has been driven inwards where the velocities are lower and thus the density decrease with radius shallower. At higher luminosities, even for day 25 after explosion, the overall shape of the spectrum is formed further out, where the higher velocities make the FeIII dominated region thiner and the flux transfered from the UV thus smaller.

Fig. 4.3 and Fig. 4.4 display the B-V, V-R and V-I behavior of both the synthetic and the real supernovæ. The real and synthetic spectra agree but for the V-I case where

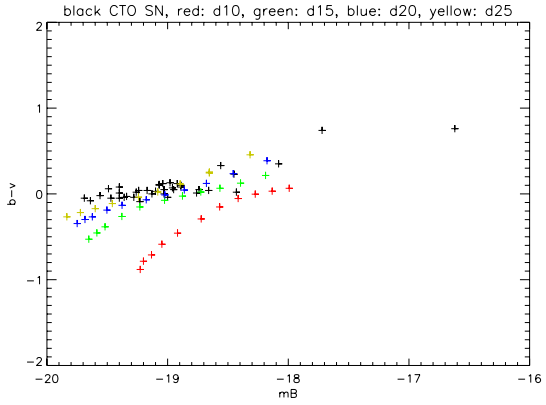

Figure 4.3: *Calan Tololo and* PHOENIX $B-V$ *vs* M_B. *Real* SNeIa *in black,* PHOENIX *ones are colored. 10 days after explosion in red, 15 in green, 20 in blue and 25 in yellow.*

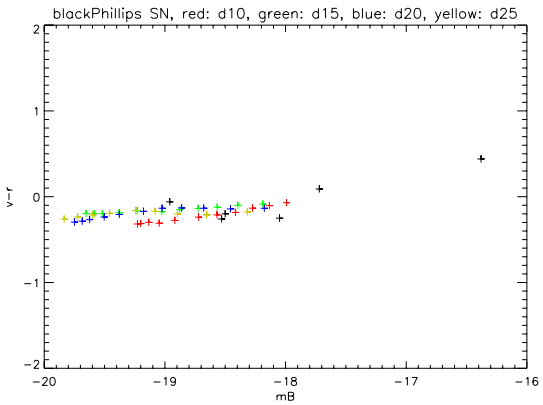

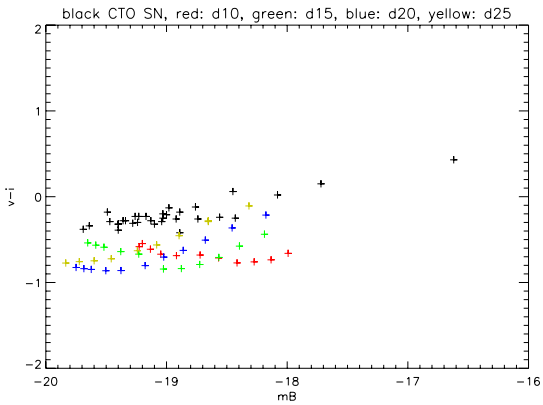

Figure 4.4: ***Left :*** *Calan Tololo and* PHOENIX $V-R$ *and* $V-I$. *Real* SNeIa *in black,* PHOENIX *ones are colored. 10 days after explosion in red, 15 in green, 20 in blue and 25 in yellow.* ***Right :*** *Idem for V-I*

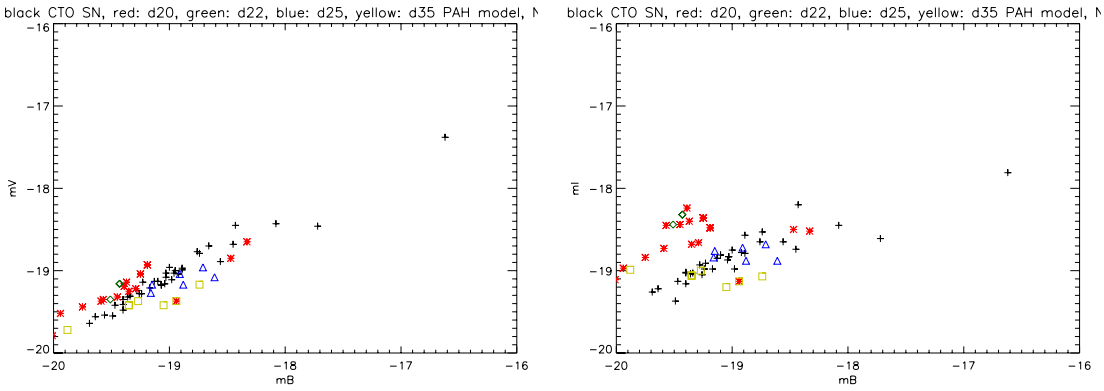

Figure 4.5: *P.Höflich models at different times and luminosities. Each date is from the explosion time. Red: day20. Green: day 22. Blue: day 25. Yellow: day 35*

the PHOENIX spectra systematically lack I flux as previously stated. The trend of the evolution as the blue magnitude increases also departs from the real supernova trend. On the other hand, even if the V and R magnitudes for the day 10 after explosion of the synthetic spectrum disagree with reality, the V-R color is in perfect agreement.

Even though it is difficult to give a detailed explanation for this effect, the present results suggest that the color formation is based on *global* properties of the SNeIa: in presence of the optically thick iron core, the detailed abundance structure has little effect on the BVRI magnitudes and even less on the colors.

The colors of P.Höflich models, with a shallower density profile, are displayed in Fig. 4.5 and Fig. 4.6. The B vs V plot is very similar to the W7 model one, stressing the point that these colors depend on the deep iron core of the models and are not sensitive to the details of the nucleosynthesis.

The I and $V - I$ plots are however in better agreement with reality than W7 model, which corroborates the hypothesis of a too steep density profile being the reason why W7 model fails to transfer enough flux from the UV. We calculated the difference of U band flux between W7 model at day 20 after explosion and the P.Höflich models to be ≈ 0.5 magnitude lower which corresponds to a 50% larger U band luminosity for W7 model.

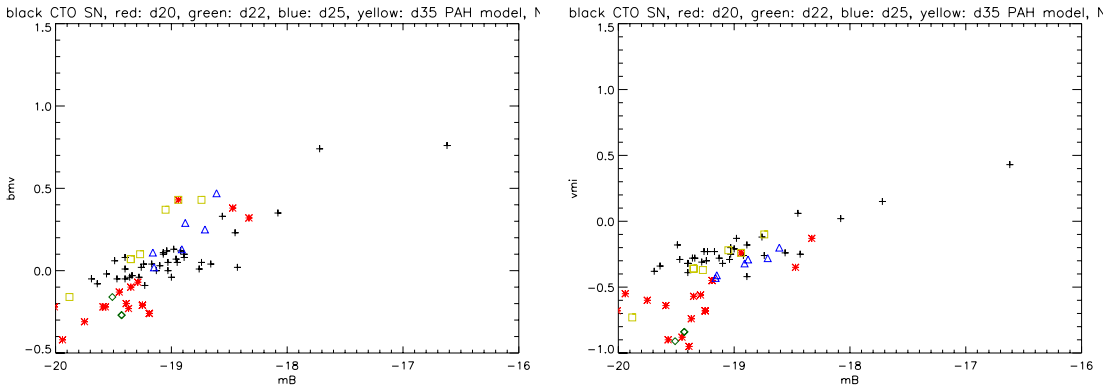

Figure 4.6: *P.Höflich models colors at different times and luminosities. Each date is from the explosion time. Red: day20. Green: day 22. Blue: day 25. Yellow: day 35*

4.4 Addendum

In (Reindl et al., 2005), a new study of the SNeIa magnitude corrections for the host extinction is discussed. The new magnitudes are listed in tab. 4.3, and show a global increase with respect to the ones we used before.

Table 4.3: Supernovæ magnitudes from (Reindl et al., 2005)
(continued on next pages)

SN	M_B	M_V	M_I	SN	M_B	M_V	M_I
SN 1937C	-19.7170	-19.7050		SN 1995D	-19.6060	-19.5970	-19.2330
SN 1960F	-19.7230	-19.6890		SN 1995E	-19.4730	-19.5190	
SN 1972E	-19.5960	-19.5900	-19.2730	SN 1995ak	-19.4160	-19.3130	-19.0820
SN 1972J	-19.2640	-19.3770		SN 1995al	-19.6670	-19.6920	-19.3310
SN 1974G	-19.5540	-19.5550		SN 1996C	-19.6600	-19.6500	-19.3890
SN 1980N	-19.4160	-19.4460	-19.1130	SN 1996X	-19.4280	-19.4240	-19.1740
SN 1981B	-19.5380	-19.5430		SN 1996Z	-19.5050	-19.4680	
SN 1981D	-19.5790	-19.5550		SN 1996ab	-19.7100	-19.6970	
SN 1982B	-19.6130	-19.6700		SN 1996bk	-19.1290	-19.2320	
SN 1983G	-19.4820	-19.4170		SN 1996bl	-19.5800	-19.5460	-19.3220
SN 1984A	-19.5710	-19.5470		SN 1996bo	-19.4120	-19.4480	

SN 1989B	-19.4250	-19.4320	-19.2770	SN 1996bv	-19.7070	-19.7150	-19.4070
SN 1990N	-19.6200	-19.5800	-19.2820	SN 1997E	-19.3840	-19.3770	-19.1750
SN 1990O	-19.6490	-19.6560	-19.2710	SN 1997Y	-19.5160	-19.4440	-19.3170
SN 1990T	-19.6470	-19.4950	-19.3910	SN 1997bp	-19.6480	-19.6350	-19.1880
SN 1990Y	-19.4850	-19.5630	-19.1630	SN 1997bq	-19.5300	-19.6460	-19.3080
SN 1990af	-19.2410	-19.2680		SN 1997dg	-19.5700	-19.5240	-19.3180
SN 1991S	-19.6300	-19.6110	-19.3080	SN 1997do	-19.6370	-19.6200	-19.3370
SN 1991U	-19.5990	-19.5350	-19.3650	SN 1997dt	-19.5950	-19.6020	-19.4220
SN 1991ag	-19.6710	-19.7060	-19.3390	SN 1998V	-19.6110	-19.5700	-19.3840
SN 1992A	-19.3240	-19.3410	-19.0990	SN 1998aq	-19.5570	-19.5350	
SN 1992J	-19.1730	-19.2090	-18.9790	SN 1998bu	-19.4920	-19.5470	-19.3620
SN 1992P	-19.6180	-19.5770	-19.3090	SN 1998dh	-19.4280	-19.4990	-19.1950
SN 1992ae	-19.4420	-19.4300		SN 1998dk	-19.5750	-19.5910	-19.2950
SN 1992al	-19.6020	-19.5490	-19.2770	SN 1998dm	-19.6240	-19.5600	-19.3920
SN 1992aq	-19.2030	-19.1930	-19.0500	SN 1998dx	-19.3120	-19.2670	-19.1280
SN 1992au	-19.1450	-19.2130	-18.8700	SN 1998ec	-19.5560	-19.5700	-19.2800
SN 1992bc	-19.7230	-19.6620	-19.4300	SN 1998ef	-19.6870	-19.6230	-19.4000
SN 1992bg	-19.5680	-19.5030	-19.2820	SN 1998eg	-19.5610	-19.5150	-19.3090
SN 1992bh	-19.5610	-19.5280	-19.3010	SN 1999X	-19.5580	-19.5470	-19.3050
SN 1992bk	-19.2520	-19.1830	-19.1150	SN 1999aw	-19.7170	-19.7500	-19.3670
SN 1992bl	-19.2790	-19.2700	-19.0770	SN 1999cc	-19.3270	-19.3360	-19.0990
SN 1992bo	-19.1960	-19.1960	-19.0590	SN 1999dk	-19.4380	-19.4500	-19.0790
SN 1992bp	-19.3300	-19.2830	-19.0730	SN 1999ee	-19.6180	-19.6830	-19.3030
SN 1992br	-19.1740	-19.2080	28.2960	SN 1999ef	-19.5490	-19.6020	-19.2030
SN 1992bs	-19.5460	-19.5210	28.8860	SN 1999ek	-19.5070	-19.5490	-19.2390
SN 1993B	-19.4820	-19.4090	-19.1760	SN 1999gd	-19.5350	-19.5370	-19.3480
SN 1993H	-19.1310	-19.2190	-19.1030	SN 1999gh	-19.1630	-19.2110	-19.0470
SN 1993L	-19.3500	-19.3240		SN 2000B	-19.2900	-19.3560	-19.0510
SN 1993O	-19.5250	-19.4330	-19.2740	SN 2000E	-19.6670	-19.6450	-19.3320
SN 1993ac	-19.4840	-19.4510	-19.3170	SN 2000bk	-19.2620	-19.1690	-19.1480

SN 1993ae	-19.3890	-19.3080	-19.2020	SN 2000ce	-19.5530	-19.6560	-19.3840
SN 1993ag	-19.4180	-19.4430	-19.1400	SN 2000cf	-19.4490	-19.4540	-19.1850
SN 1993ah	-19.3680	-19.3310	-19.0450	SN 2000cn	-19.1930	-19.2940	-19.0970
SN 1994D	-19.4740	-19.4120	-19.2660	SN 2000dk	-19.2470	-19.2820	-19.0580
SN 1994M	-19.3600	-19.3310	-19.1280	SN 2000fa	-19.6500	-19.6030	-19.3190
SN 1994Q	-19.6570	-19.6850	-19.3480	SN 2001V	-19.6370	-19.6260	-19.3190
SN 1994S	-19.6220	-19.6030	-19.3210	SN 2001el	-19.5850	-19.5230	-19.2480
SN 1994T	-19.3120	-19.3560	-19.1060	SN 2002bo	-19.4570	-19.5750	-19.1920
SN 1994ae	-19.7030	-19.6900	-19.3080	SN 2002er	-19.4010	-19.4270	-19.1710

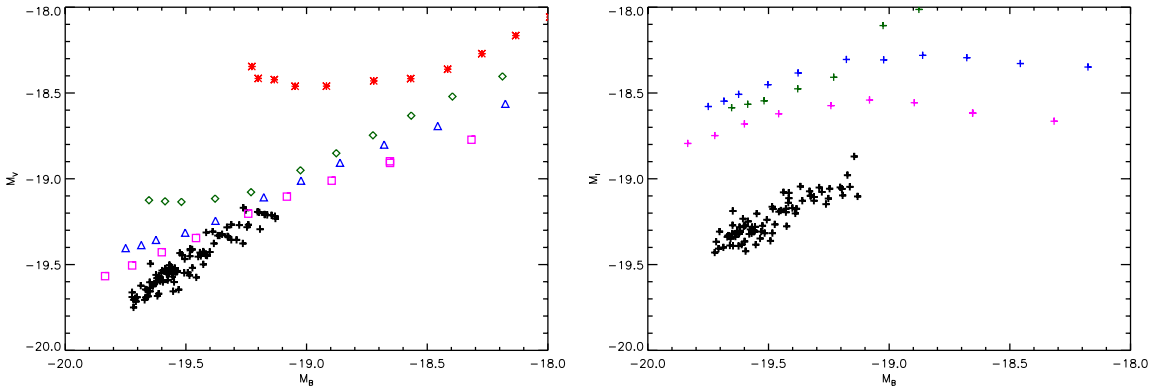

Figure 4.7: ***Left:*** *M_B and M_V versus* PHOENIX *M_B and M_V. Real* SNeIa *in black,* PHOENIX *ones are colored. 10 days after explosion in red, 15 in green, 20 in blue and 25 in yellow.* ***Right :*** *idem but for M_B and M_I*

We display in fig. 4.7, fig. 4.8, fig. 4.9, fig. 4.10 and fig. 4.11 the same plots as in the previous sections where the real supernovæ luminosities have been replaced by the ones from (Reindl et al., 2005).

Each one of these plots shows smaller SNeIa dispersion after the new corrections for host extinction are applied.

The general conclusions from the previous section are not changed by the new set of magnitudes, although if the luminosity range where the W7 model correctly reproduces the real SNeIa colors has decreased.

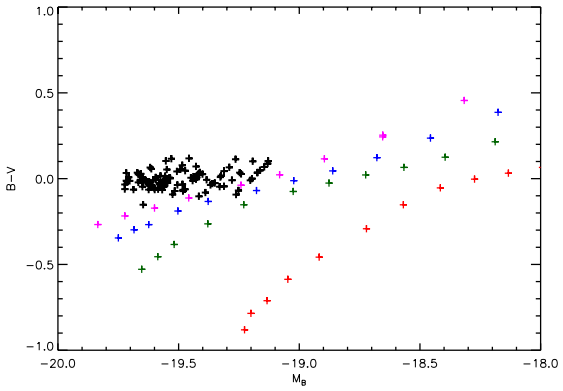

Figure 4.8: *Real and* PHOENIX $B-V$ *vs* M_B. *Real* SNeIa *in black,* PHOENIX *ones are colored. 10 days after explosion in red, 15 in green, 20 in blue and 25 in yellow.*

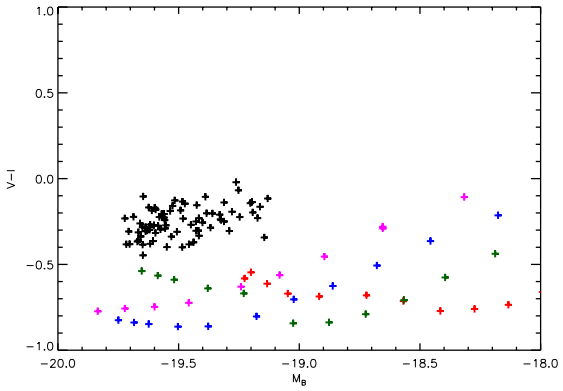

Figure 4.9: *Real and* PHOENIX $V-I$. *Real* SNeIa *in black,* PHOENIX *ones are colored. 10 days after explosion in red, 15 in green, 20 in blue and 25 in yellow.*

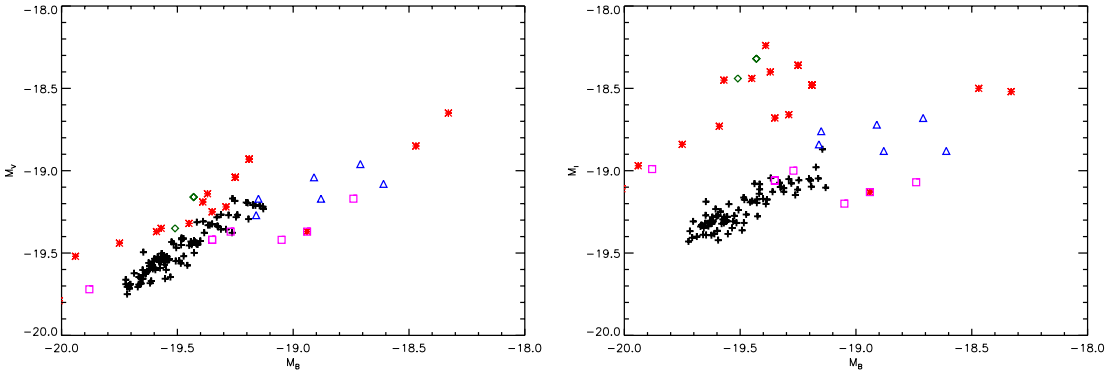

Figure 4.10: *P.Höflich models at different times and luminosities. Each date is from the explosion time. Red: day20. Green: day 22. Blue: day 25. Yellow: day 35.* ***Left:*** M_V *vs* M_B. ***Right:*** M_I *vs* M_B

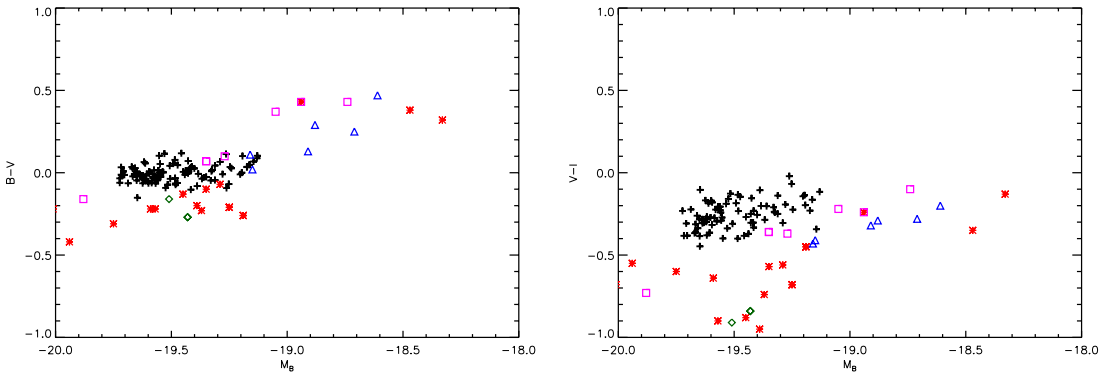

Figure 4.11: *P.Höflich models at different times and luminosities. Each date is from the explosion time. Red: day20. Green: day 22. Blue: day 25. Yellow: day 35.* ***Left:*** $M_B - M_V$ *vs* M_B. ***Right:*** $M_V - M_I$ *vs* M_B

Chapter 5

Some empirical spectral ratio correlated to luminosity

In this chapter we shall redefine some spectroscopic luminosity indicators first presented in (Nugent et al. (1995)). We shall also define a new indicator of higher accuracy. And finally, we will simulate the expected accuracy on SNeIa luminosity measures in the SNAP/JDEM context using these spectroscopic ratios.

5.1 $\Re_{Si}$ and $\Re_{Ca}$:

5.1.1 Definitions:

$\Re_{Si}$ and $\Re_{Ca}$, are empirical line ratios that were first defined in (Nugent et al. (1995)). They are called after the main element identified in the considered wavelength zones.

	$\Re_{Si}$ zones lower wavelength in Å	$\Re_{Si}$ zones higher wavelength in Å
First maximum	6200	6450
Second maximum	5850	6000
Third maximum	5500	5700
6355 Å minimum	6050	6250
5979 Å minimum	Variable	Variable

Table 5.1: $\Re_{Si}$ *definition zones*

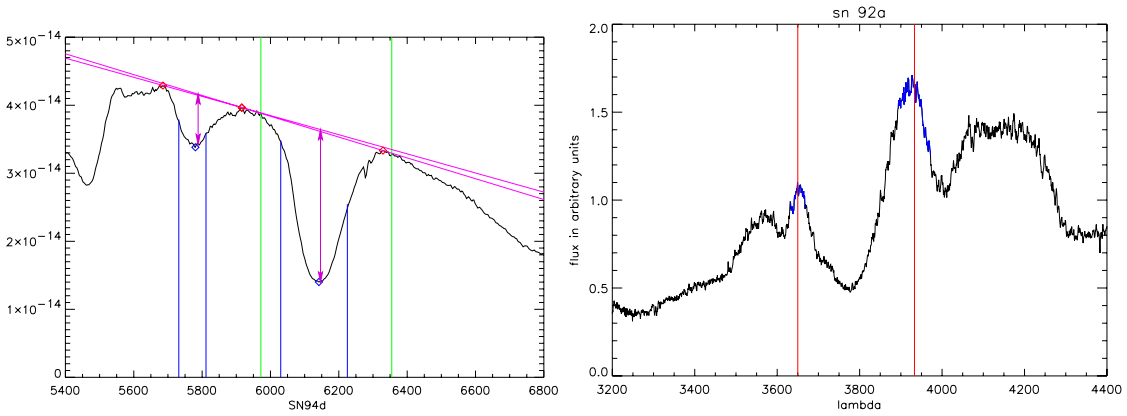

Figure 5.1: ***Left:*** *Green lines locate the* 6355 *Å and* 5979 *Å* Si II *lines. The blue lines locate the regions where the minima are searched for. The red diamonds locate the three maxima used to draw the two purple reference lines, and the two purple arrows represent* d_{red} *and* d_{blue} *used to compute* $\Re_{Si}$. ***Right:*** *Red lines locate the* $3650Å$ *and the* $3933Å$ *Ca* II *lines. The maxima used to calculate* $\Re_{Ca}$ *are searched in the two blue colored regions.*

$\Re_{Si}$ definition:

$\Re_{Si}$ is named after the characteristic Si II trough found at $\approx$ 6100Åand usually associated to the absorption part of the 6355 Å Si II line P-Cygni feature.

In the left hand side of Fig. 5.1, the green lines label the 6355 Å and 5979 Å Si II lines rest wavelengths. The red diamonds locate the maxima and the blue diamonds the minima found in the wavelength zones defined in tab. 5.1.1.

The 6355 Å minimum band is centered on the 6355 Å line blueshifted of approximately 10000km.s^{-1}[1]. It corresponds to the average velocity at which the Si II line is supposed to form. The $\approx$ 200Å wide wavelength zone where we search for the second minimum is noted as "variable" because it is centered on the 5979 Å line blueshifted by the same actual velocity than the 6355 Å minima. This to ensure to find the right trough assumed to be at least partly created by the 5979 Å Si II line, which should thus form in the same physical region.

$\Re_{Si}$ is defined as the ratio of the vertical distances between each minima and the reference lines drawn between two consecutive maxima d_{blue} and d_{red}, as shown in Fig. 5.1.

[1]Because of the homologous expansion, it is usual to use equivalently velocities or Å when analyzing supernovæ spectra.

$$\Re_{Si} = \frac{d_{blue}}{d_{red}} \tag{5.1}$$

This definition differs slightly from the one of Nugent et al. (1995), where tangents to the spectrum were manually selected instead of the reference lines between two consecutive maxima. These two methods mainly differ when the zones searched for maxima only display inflection points, but our method was easier to automatize, and we shall turn to such cases later.

Finally, because is is defined as the distance between points of the spectrum and references linearly coupling points of the spectrum, $\Re_{Si}$ is independent of the absolute flux calibration. Moreover, as it is calculated within a wavelength region only ≈ 1000Å wide, the relative flux calibration is not critical.

$\Re_{Ca}$ definition:

Following Nugent et al. (1995), we defined two zones in the 3000Å 5000Å region of the spectra, centered on the CaII 3650Å and 3933Å lines, as shown in the right hand side of Fig. 5.1. $\Re_{Ca}$ is defined as the ratio of the $\approx$ 3933Å maximum ($max_{3933\text{Å}}$) over the $\approx$ 3650Å one ($max_{3650\text{Å}}$).

$$\Re_{Ca} = \frac{max_{3933\text{Å}}}{max_{3650\text{Å}}} \tag{5.2}$$

The width of the zones searched for these maxima are displayed in tab. 5.2.

The maxima are almost *never* found at the exact CaII lines wavelength. This was to be expected since even if we had pure CaII, non-scattering effects could move the feature's maximum wavelength. Moreover, we shall show that these lines are line blends, and not pure CaII features.

$\Re_{Ca}$ Central wavelength in Å	Zones half width in Å
3650	40
3933	65

Table 5.2: $\Re_{Ca}$ *maximum zones*

When studying these line blends with PHOENIX, we also noted that the dominating elements in the wavelength zones considered behave mostly in the same way with respect to

a luminosity change. This lead us to define an integral ratio we named $\Re_{CaS}$ [2] as

$$\Re_{CaS} = \frac{\int_{3868\text{Å}}^{3998\text{Å}} F_\lambda d\lambda}{\int_{3610\text{Å}}^{3690\text{Å}} F_\lambda d\lambda} \tag{5.3}$$

Both $\Re_{Ca}$ and $\Re_{CaS}$ ratios, like $\Re_{Si}$, are independent of the absolute flux calibration, and not too sensitive to the relative calibration quality.

Dealing with the noise:

The main merit of $\Re_{CaS}$ over $\Re_{Ca}$ is the increased signal to noise ratio. On the other hand, $\Re_{Ca}$ and $\Re_{Si}$ will be highly sensitive to noise since they rely on maxima and minima detections. In order to minimize this effect, we fit each wavelength zone considered with a 6^{th} degree polynomial and search for their local maximum or minimum.

We need to search a wavelength range wide enough to ensure finding the right maxima and minima, but in these large zones the spectral features shapes are more complex than second degree polynomial. On the other hand, the noise may generate oscillations for too high degrees. A 6^{th} degree polynomial empirically proved to be a good compromise between these two effects.

5.1.2 Correlation with luminosity:

name	Day after max	Blue absolute magnitude
SN 1981B	0	-19.07
SN 1986G	-1, -3, -5, 1, 3	-18.08
SN 1989B	-1, -5	-18.58
SN 1991bg	0, -2	-16.62
SN 1991T	-3, 0	-19.44
SN 1992A	0, -1, -5, 3, 5	-18.48
SN 1994D	2, 3, 4, 5, -3, -4, -5	-19.0

Table 5.3: *Supernovæ used in our simulation. Absolute magnitudes from Hamuy et al. (1996) and Nugent et al. (1995)*

We applied these definitions to the public supernovæ spectra we were able to gather, listed in tab. 2 and plotted in Appendix 8.2.

[2] The S standing for Surface. And also for SNURP since SNURP RULES!

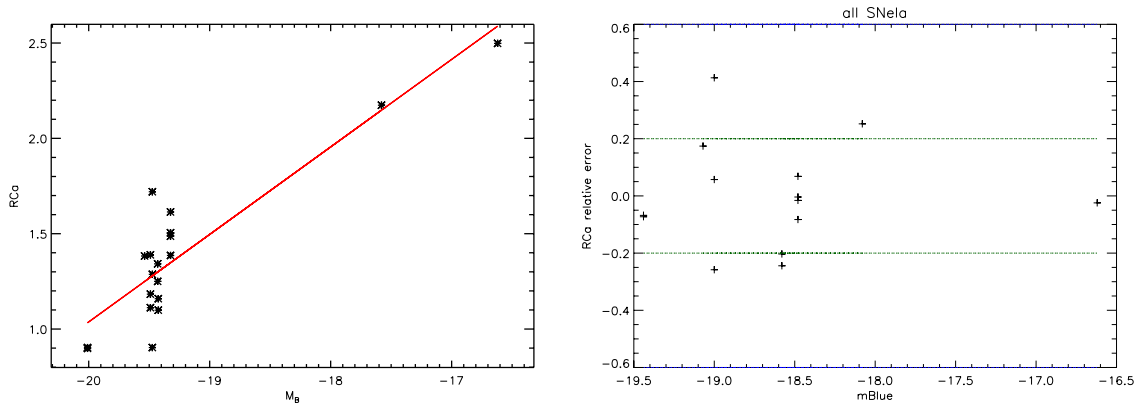

Figure 5.2: ***Left:*** *$\Re_{Ca}$ calculated on tab 2 supernovæ,* ***Right:*** *$\Re_{Ca}$ relative dispersion*

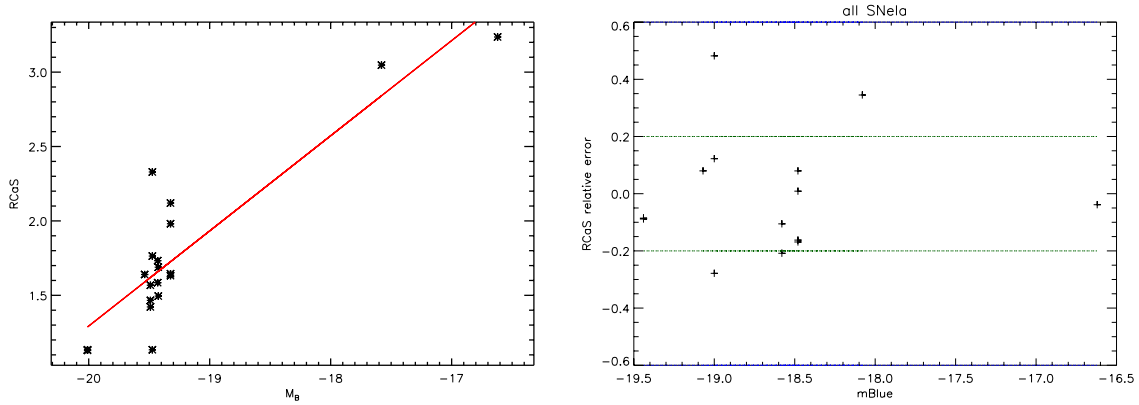

Figure 5.3: ***Left:*** *$\Re_{CaS}$ calculated on tab 2 supernovæ,* ***Right:*** *$\Re_{CaS}$ relative dispersion*

Even though $\Re_{Si}$ and $\Re_{Ca}$ were originally defined for SNeIa spectra at maximum light, we used spectra ranging from 5 days prior to maximum to 5 days after maximum.

We relaxed the time constraint in order to show whether or not the date of the spectra has a critical impact on the ratios correlation with luminosity. Moreover, since space program like SNAP/JDEM will only take one spectrum per supernova, we wanted to quantify the time window where spectra are usable for luminosity measures with line ratios.

On the other hand the rise time for supernovæ at $z \approx 1$ is twice slower in the observer rest frame. Relaxing the time constraint to ± 5 days around maximum was thus conservative.

$\Re_{Ca}$ & $\Re_{CaS}$ correlation with luminosity:

	Slope	Constant	Variance
$\Re_{Ca}$	0.56	11.94	0.25
$\Re_{CaS}$	0.75	15.89	0.37

Table 5.4: *$\Re_{Ca}$ and $\Re_{CaS}$ linear regression on the real supernovæ with sufficient wavelength coverage*

Calibration of the correlation relation: Some of the supernovæ listed in tab. 2 lacked the wavelength coverage needed to calculate $\Re_{Ca}$ and $\Re_{CaS}$. For the other ones, we plotted the values obtained in Fig. 5.2 and Fig. 5.3.

The $\Re_{Ca}$ values for maximum light spectra agree with Nugent et al. (1995) to within a few %. In order to calibrate the luminosity relations, we computed the linear regression of $\Re_{Ca}$ and $\Re_{CaS}$ values with respect to blue magnitude.

$$\Re_{Ca} = a_{\Re_{Ca}} M_B + b_{\Re_{Ca}} \tag{5.4}$$

$$\Re_{CaS} = a_{\Re_{CaS}} M_B + b_{\Re_{CaS}} \tag{5.5}$$

We list the resulting parameters in tab. 5.4. Since we have no information on the spectra signal to noise, we had no way to estimate the errors, and forced them to be arbitrary all equal to 1.

We also calculated the variance for $\Re_{Ca}$ and $\Re_{CaS}$, defined as the quadratic mean of the distance of each supernova with the linear regression, and found it to be:

$$\sigma_{\Re_{Ca}} \approx 0.25 \tag{5.6}$$

$$\sigma_{\Re_{CaS}} \approx 0.37 \tag{5.7}$$

$$\tag{5.8}$$

We checked that taking out either one or both of the non "Branch Normal" supernovæ did not improve the quality of the calibration, i.e. did not decrease the variances. We recall that the non "Branch Normal" supernovæ refer to SN 1991T and SN 1991bg in our sample.

Time evolution: We plotted in Fig. 5.4 the $\Re_{Ca}$ and $\Re_{CaS}$ time dependence for each supernova. When enough points where available, we interpolated the $t = 0$ point using a

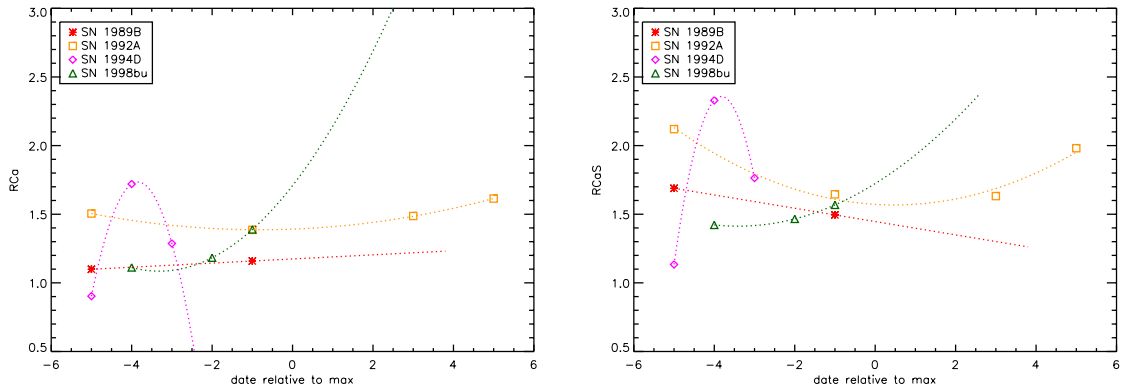

Figure 5.4: ***Left:*** *$\Re_{Ca}$ and $\Re_{CaS}$ time evolution*

	Slope	Constant	Variance
$\Re_{Ca}$	0.55	11.7	$\sigma_{\Re_{Ca}} = 0.24$
$\Re_{CaS}$	0.73	15.29	$\sigma_{\Re_{CaS}} = 0.41$

Table 5.5: *$\Re_{Ca}$ and $\Re_{CaS}$ linear regression on the real supernovæ with sufficient wavelength coverage using the $t = 0$ interpolated values*

2^{nd} degree polynomial. For the cases with two points only, we used a linear regression.

The supernova SN 1994D had enough points for a 2^{nd}order polynomial interpolation, but since all of them are for $t \leq -3$ days, and since the trend is different from the other supernovæ, we considered the $t = 0$ point to be too much of an extrapolation to be used. Whether or not SN 1994D $\Re_{Ca}$ or $\Re_{CaS}$ dispersion is intrinsic or due to uncertainties measures is still an open question, but we checked that it does not comes from our calculation.

Replacing each $\Re_{Ca}$ and $\Re_{CaS}$ by the corresponding $t = 0$ calculated value, we recomputed the linear regression, and the associated variance, this time defined as the quadratic mean of the distances between the regression and the extrapolated $t = 0$ values. These results are shown in tab. 5.5.

More spectra are needed in order to show if there is any kind of time sequence in the $\Re_{Ca}$ or $\Re_{CaS}$ evolution, but there is nothing as simple as a single time evolution for all the SNeIa. Until more data becomes available, as the $t = 0$ interpolation or extrapolation almost did not change, the calibration, we decided to stay on the conservative side and treat $\Re_{Ca}$ and $\Re_{CaS}$ time dependence as an uncontrolled dispersion. Note that $\Re_{CaS}$ does not reduce the dispersion with respect to $\Re_{Ca}$, since the signal to noise of the spectra we used is

always high enough for the intrinsic dispersion to dominate. Therefore, even if $\Re_{CaS}$ would be more robust to Poisson noise and thus decrease the correspondent dispersion with respect to $\Re_{Ca}$, this is not the case here where the noise is negligible.

Luminosity measure precision using $\Re_{Ca}$ or $\Re_{CaS}$: With the linear regression calibration of $\Re_{Ca}$ and $\Re_{CaS}$ with respect to blue magnitude and the associated variance, we where able to estimate the luminosity precision measure using these ratios as follows:

$$\Re_{Ca} = a_{\Re_{Ca}} M_B + b_{\Re_{Ca}} \tag{5.9}$$

$$\sigma_{\Re_{Ca}} = a_{\Re_{Ca}} \Delta M_B \tag{5.10}$$

$$\Delta M_B = \frac{\sigma_{\Re_{Ca}}}{a_{\Re_{Ca}}} \tag{5.11}$$

$$\frac{\Delta_L}{L} \approx \frac{\sigma_{\Re_{Ca}}}{a_{\Re_{Ca}}} \tag{5.12}$$

We display in tab. 5.6 the measurement accuracy on the blue magnitude as estimated for $\Re_{Ca}$ and $\Re_{CaS}$. We find $\Delta M_B \approx \pm 0.4$ for $\Re_{Ca}$ and $\Delta M_B \approx 0.5$ for $\Re_{CaS}$. This is twice the $\Delta M_B \approx \pm 0.2$ dispersion of the "Branch Normal" SNeIa luminosity measure with the light curve method. On the other hand these line ratio provide an independent method which, together with a sufficient number of supernovæ, could be used to constrain the evolutionary effects of SNeIa explosions.

	Dispersion	slope	Blue magnitude accuracy
$\Re_{Ca}$	$\sigma_{\Re_{Ca}} \approx 0.24$	0.56	± 0.4
$\Re_{CaS}$	$\sigma_{\Re_{CaS}} \approx 0.37$	0.75	± 0.5

Table 5.6: *Estimate of the luminosity measure precision using $\Re_{Ca}$ and $\Re_{CaS}$*

Since we did not use the $t = 0$ extrapolated values, the variances $\sigma_{\Re_{Ca}}$, and $\sigma_{\Re_{CaS}}$ account for both the time and intrinsic supernovæ dispersion. On the other hand, since the $t = 0$ extrapolation hardly changes the results, we conclude that for our data, the variance is dominated by the intrinsic and not the time dispersion.

$\Re_{Si}$ correlation with luminosity:

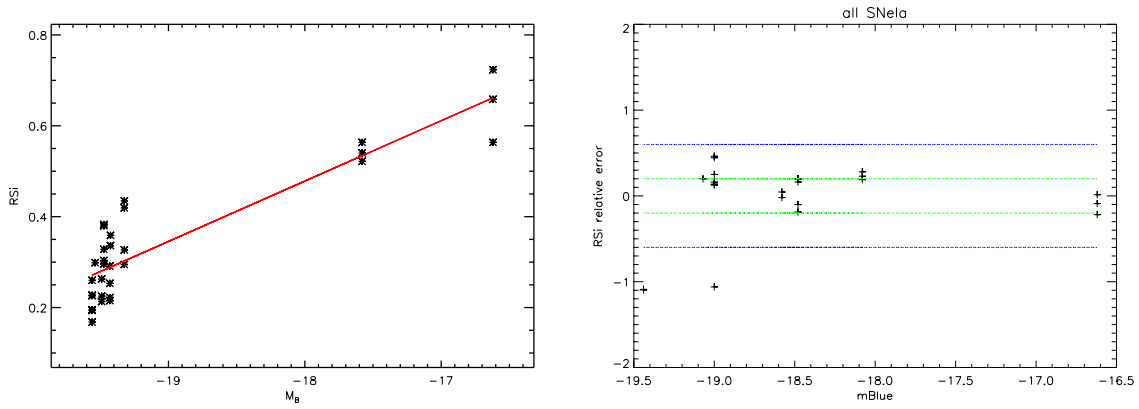

Figure 5.5: ***Left:*** *$\Re_{Si}$ calculated on tab 2 supernovæ,* ***Right:*** *$\Re_{Si}$ relative dispersion*

The correlation calibration We plot in Fig. 5.5 the $\Re_{Si}$ values calculated on the supernovæ from tab. 2. The two $\Re_{Si}$ negative values correspond to the peculiar SN 1991T spectrum, and the 5 days prior maximum light SN 1994D spectrum, for which the blue through associated to the 5979 Å line does not exist.

The $\Re_{Si}$ ratio is of course mathematically well defined even in this peculiar case, but since these points fall out of the general trend and increase the $\Re_{Si}$ slope, we removed them from the linear regression. This selection is compatible with observational constraints, as such spectra are easily identified when the signal to noise allows to measure $\Re_{Si}$.

The linear regression and the corresponding relative dispersion for this selection of supernovæ is shown in Fig. 5.6.

$$\Re_{Si} = a_{\Re_{Si}} M_B + b_{\Re_{Si}} \tag{5.13}$$

We also calculated the associated variance, defined as the quadratic mean of the distances between the measured $\Re_{Si}$ and the linear regression, and found it to be

$$\sigma_{\Re_{Si}} \approx 0.06 \tag{5.14}$$

At this point this variance includes the time as well as the intrinsic dispersion of the supernovæ.

Time evolution: We plot in Fig. 5.7 $\Re_{Si}$ time dependence of the supernovæ we dispose of. We calculated a quadratic regression for each supernova presenting three or more $\Re_{Si}$ values.

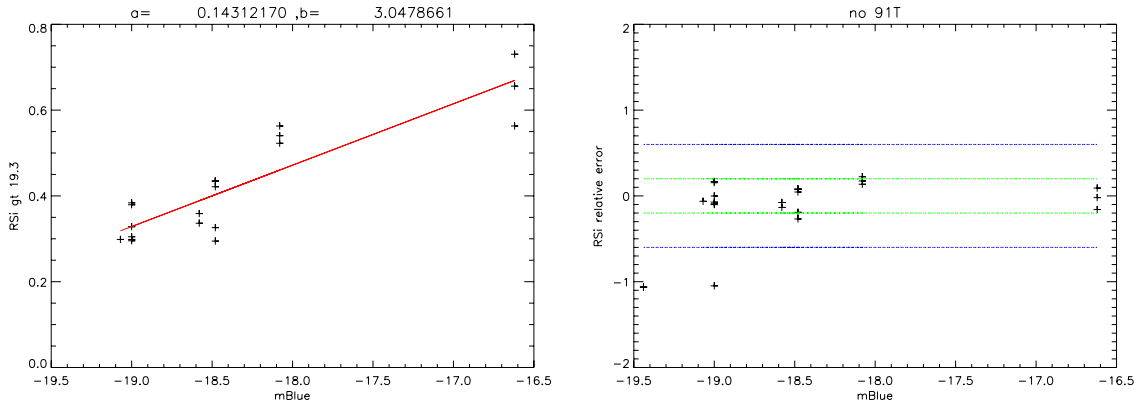

Figure 5.6: ***Left:*** *$\Re_{Si}$ calculated on tab 2 supernovæ,* ***Right:*** *$\Re_{Si}$ relative dispersion. SN 1991T and SN 1994D 5 days prior to maximum spectra have been excluded of the regression.*

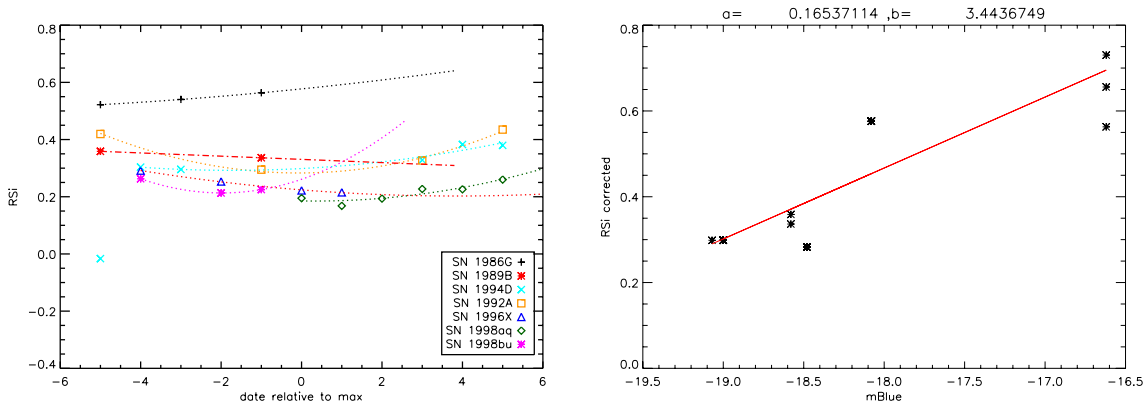

Figure 5.7: ***Left:*** *$\Re_{Si}$ time dependence.* ***Right:*** *$\Re_{Si}$ correlation with $t = 0$ interpolated values.*

We then replaced *each* $\Re_{Si}$ value by the corresponding $t = 0$ interpolated or extrapolated value. The new linear regression calculated for $\Re_{Si}$ correlation with luminosity is also plotted in Fig. 5.7.

The variance calculated with respect to this new regression, still removing the events with negative $\Re_{Si}$, is now:

$$\sigma_{\Re_{Si}} \approx 0.08 \tag{5.15}$$

This dispersion is the distance between the extrapolated values for $t = 0$ and the linear regression. If we calculate it with respect the uncorrected values distances to the linear regression done on the $t = 0$ extrapolated values, the variance is left to be $\sigma_{\Re_{Si} \approx 0.08}$. It

proves the variance to be dominated by the intrinsic dispersion of the supernovæ for $\Re_{Si}$. Moreover, the left hand side of Fig. 5.7 also shows that there is no general time dependence trend for our supernovæ sample.

Luminosity measure precision: As in 5.1.2 we estimate the accuracy of the luminosity determination using $\Re_{Si}$ directly from the dispersion with respect to the linear regression. Table 5.7 summarizes the results.

	Dispersion	slope	Blue magnitude accuracy
$\Re_{Si}$, no $\Re_{Si} < 0$	$\sigma_{\Re_{Si}} \approx 0.06$	0.14	± 0.4
$\Re_{Si}$, no $\Re_{Si} < 0$	$\sigma_{\Re_{Si}} \approx 0.08$	0.16	± 0.5
$t = 0$ extrapolation			

Table 5.7: *Estimate of the luminosity measure precision using* $\Re_{Si}$.

The accuracy of the luminosity measure with $\Re_{Si}$ is twice as large as the dispersion of normal SNeIa measured with the light curve method, and the $t = 0$ extrapolation does not improve its accuracy because of the dominant intrinsic dispersion. On the other hand we now dispose with $\Re_{Ca}/\Re_{CaS}$ of two independent luminosity spectral indicators, one on the blue and one on the red part of the spectrum, which gives an improved leverage to constrain the evolutionary effects of SNeIa.

5.2 A new spectral indicator: $\Re_{SiS}$

5.2.1 $\Re_{SiS}$

Definition

The $\Re_{Si}$ zone, because of the $\Re_{Si}$ correlation with luminosity, has been particularly studied in this thesis work. More will be said about the line formation in this spectral region in chapter 6, but the clarification of the spectrum formation process allowed us to devise a new line ratio indicator which we called $\Re_{SiS}$.

$\Re_{SiS}$ is defined as the ratio of two maxima. The first maximum is the one used in $\Re_{Si}$ calculation, located around 6355 Å, and the second one is the bluer peak of $\Re_{Si}$ located in the $5600 - 5700$Å region. The zones where we look for these maxima are recalled in

	$\Re_{SiS}$ zones lower wavelength in Å	$\Re_{SiS}$ zones higher wavelength in Å
First maximum	6200	6450
Third maximum	5500	5700

Table 5.8: $\Re_{SiS}$ *definition zones*

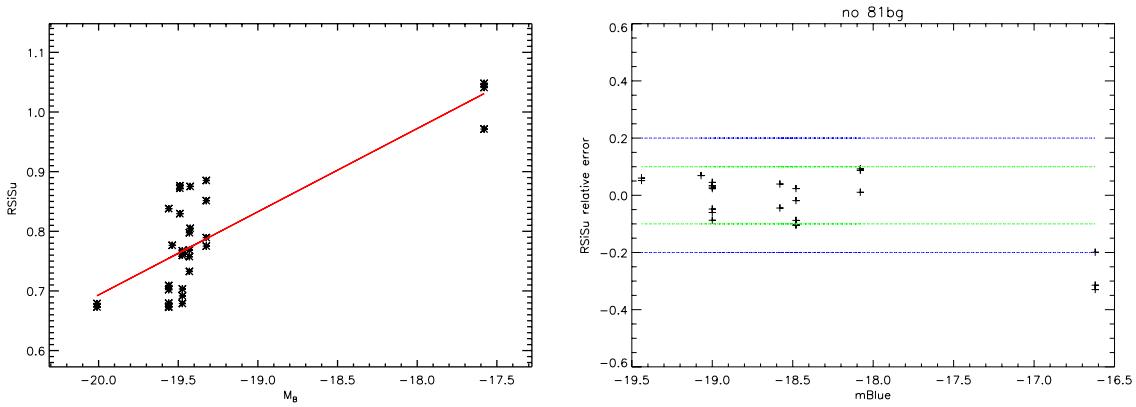

Figure 5.8: ***Left:*** $\Re_{SiS}$ *calculated on the supernovæ of tab 2.* ***Right:*** $\Re_{SiS}$ *relative dispersion. The SN 1991bg has been excluded of the linear regression.*

tab. 5.2.1. As for $\Re_{Si}$ and $\Re_{Ca}$, we used 6^{th} order polynomial to fit the regions searched for the maxima, in order to increase the ratio robustness with respect to Poisson noise.

We also define the integral ratio $\Re_{SiSS}$ as:

$$\Re_{SiSS} = \frac{\int_{5500\text{Å}}^{5700\text{Å}} F_\lambda d\lambda}{\int_{6450\text{Å}}^{6200\text{Å}} F_\lambda d\lambda} \tag{5.16}$$

Once again, the simplicity of this integral ratio calculation and its robustness to noise makes it an interesting alternative to the line fitting method.

Correlation with luminosity

Correlation calibration To compute the linear regression of the $\Re_{SiS}$ correlation with luminosity, we excluded the peculiar subluminous SN 1991bg supernova. This selection increased the quality of the calibration and is consistent with the line forming process, as it shall been shown later.

We plot the linear regression of $\Re_{SiS}$ correlation with luminosity in the left hand side

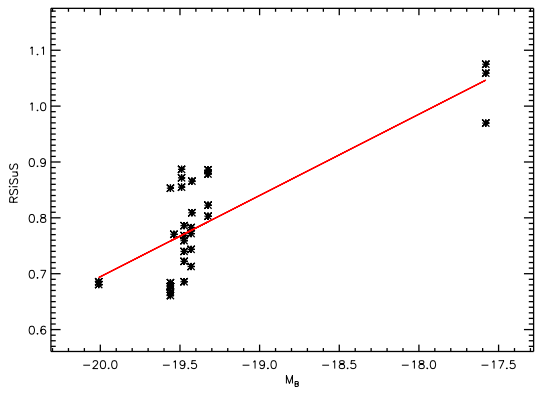

Figure 5.9: $\Re_{SiSS}$ *calculated on the supernovæ of tab 2.*

	Slope	Constant	Variance
$\Re_{SiS}$ all SNeIa	0.1	2.6	$\sigma_{\Re_{SiS}} = 0.08$
$\Re_{SiS}$ no 91bg	0.25	5.4	$\sigma_{\Re_{SiS}} = 0.05$
$\Re_{SiSS}$ all SNeIa	0.1	2.7	$\sigma_{\Re_{SiSS}} = 0.08$
$\Re_{SiSS}$ no 91bg	0.25	5.5	$\sigma_{\Re_{SiSS}} = 0.05$

Table 5.9: $\Re_{SiS}$ *and* $\Re_{SiSS}$ *linear regression on the real supernovæ with sufficient wavelength coverage using the* $t = 0$ *interpolated values*

of Fig. 5.8. The right hand side of the same figure shows the dispersion of $\Re_{SiS}$, smaller than $\Re_{Si}$ and $\Re_{Ca}$ dispersions for all but the peculiar subluminous supernova SN 1991bg. We also plot in Fig. 5.9 $\Re_{SiSS}$ correlation with luminosity. Its dispersion, almost identical to $\Re_{SiS}$ is not displayed. Table 5.9 summarizes the results for both quantities.

Time dependence In Fig. 5.10 and Fig. 5.11 we plot the time dependence of $\Re_{SiS}$ and $\Re_{SiSS}$ as well as the linear regression calculated on the values at $t = 0$ interpolated or extrapolated with quadratic fits. The three supernovæ with sufficient data do not display a common time evolution, making doubtful the existence of an universal $\Re_{SiS}$ or $\Re_{SiSS}$ time correction.

The variances calculated as the quadratic mean of the distance of all but the SN 1991bg supernova $\Re_{SiS}$ and $\Re_{SiSS}$ to the linear regression calculated with the extrapolated $t = 0$

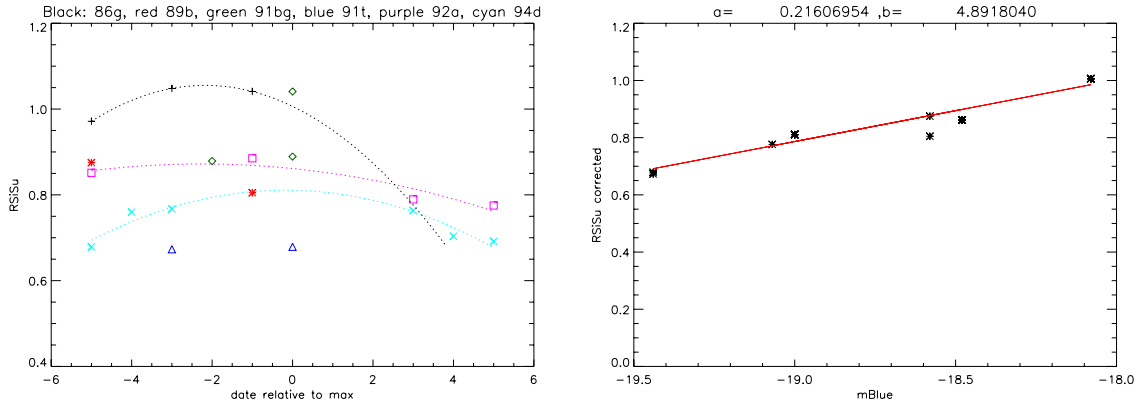

Figure 5.10: ***Left:*** *$\Re_{SiS}$ time evolution,* ***Right:*** *$\Re_{SiS}$ corrected for the time dependence.*

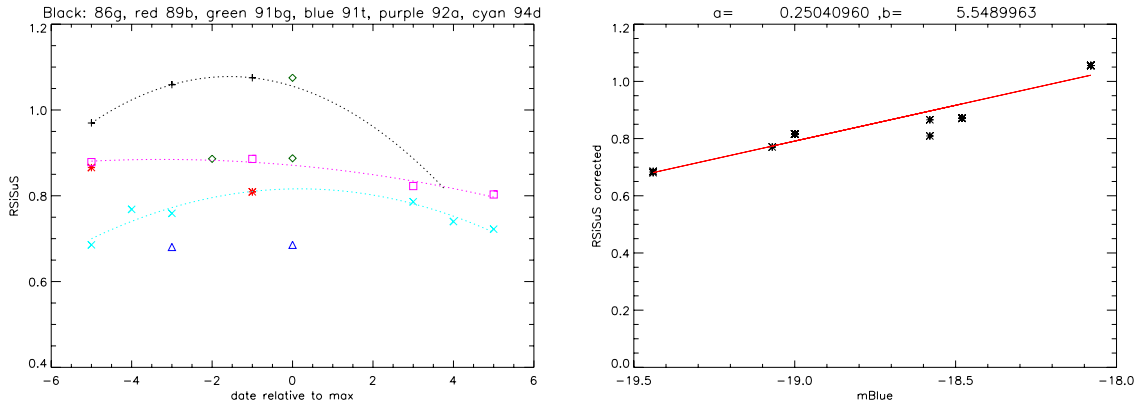

Figure 5.11: ***Left:*** *$\Re_{SiSS}$ time evolution,* ***Right:*** *$\Re_{SiSS}$ corrected for the time dependence.*

values are:

$$\sigma_{\Re_{SiS}} = 0.06 \quad (5.17)$$

$$\sigma_{\Re_{SiSS}} = 0.06 \quad (5.18)$$

$$(5.19)$$

Whereas the variance of the estimated values of $\Re_{SiS}$ and $\Re_{SiSS}$ for $t = 0$ with respect to the $t = 0$ extrapolated linear regression are:

$$\sigma_{\Re_{SiS}} = 0.04 \quad (5.20)$$

$$\sigma_{\Re_{SiSS}} = 0.04 \quad (5.21)$$

$$(5.22)$$

Correcting for the time evolution can thus increase the $\Re_{SiS}$ and $\Re_{SiSS}$ efficiency, the drawback being the need of at least three points to interpolate or extrapolate the $t = 0$ value with a quadratic fit. Since there is no common trend for the three supernovæ fitted, this correction remains purely empirical. Still, the intrinsic dispersion can be estimated to be $\sigma \approx 0.04$, and the time & intrinsic dispersion to be $\sigma \approx 0.06$ for both $\Re_{SiS}$ and $\Re_{SiSS}$.

Luminosity measure precision In tab. 5.10 we summarize the different slopes and dispersion values for $\Re_{SiS}$ and $\Re_{SiSS}$ calculated with or without the time dispersion correction. In each case the subluminous SN 1991bg has been excluded.

	Dispersion	slope	Blue magnitude precision
$\Re_{SiS}$	$\sigma_{\Re_{SiS}} \approx 0.05$	0.25	± 0.2
$\Re_{SiS}$ $t = 0$	$\sigma_{\Re_{SiS}} \approx 0.04$	0.23	± 0.17
$\Re_{SiSS}$	$\sigma_{\Re_{SiSS}} \approx 0.05$	0.25	± 0.2
$\Re_{SiSS}$ $t = 0$	$\sigma_{\Re_{SiSS}} \approx 0.04$	0.25	± 0.16

Table 5.10: *Estimate of the luminosity measure precision using* $\Re_{SiS}$ *and* $\Re_{SiSS}$

With this spectral indicator family even without time correction, we have augmented the blue magnitude accuracy by a factor of two compared to $\Re_{Si}$ and $\Re_{Ca}$, reaching the intrinsic "Branch Normal" supernovæ dispersion. Since $\Re_{SiS}$ and $\Re_{Si}$ can not be considered

BLUE				RED			
λ in Å	$\frac{\lambda}{\Delta\lambda}$	λ in Å	$\frac{\lambda}{\Delta\lambda}$	λ in Å	$\frac{\lambda}{\Delta\lambda}$	λ in Å	$\frac{\lambda}{\Delta\lambda}$
4000	295.	7500	95.	10000.	78.	14000.	86.
4500	235.	8000	90.	10500.	77.	14500.	90.
5000	185.	8500	85.	11000.	77.	15000.	93.
5500	155.	9000	80.	11500.	78.	15500.	97.
6000	130.	9500	78.	12000.	79.	16000.	100.
6500	115.	10000	75.	12500.	80.	16500.	105.
7000	105.			13000.	82.	17000.	110.
				13500.	84.		

Table 5.11: SNAP/JDEM *blue and red* $\Delta\lambda$ *bin size*

as independent, we still have only two independent spectral indicators. But one of them is as accurate as the light curve method, and with a sufficient number of supernovæ they will definitely allow to constrain the evolutionary effects.

5.3 $\Re_{Si}$, $\Re_{Ca}$ and $\Re_{SiS}$ used in SNAP/JDEM context

In order to estimate the luminosity measure accuracy of these spectral indicators in a cosmological context, we simulated SNAP/JDEM exposures at different redshifts. We used them to estimate the accuracy on the determination of the mean luminosity of "Branch Normal" supernovæ, which is the value needed to devise the Hubble diagram and the determination of cosmological parameters.

5.3.1 SNAP/JDEM simulator

The SNAP/JDEM spectrometer

To simulate SNAP/JDEM spectrometer, we assumed 50% optical and 70% CCD efficiencies. We considered the mirror surface to be $\pi\ m^2$ and implemented the rebinning of the supernovæ spectra to SNAP/JDEM binning in the observer rest frame. The red and blue channel resolution of SNAP/JDEM we used are summarized in table 5.11.

As the two spectrograph channels separation is not precisely defined yet, we trxeated the spectra as if the red and the blue detector properties where the same. But as the edges of the spectral range are harder to calibrate, their location can impact the final results.

readout noise/pixel	$\sqrt{2} \cdot 5 \cdot 1.e$
slow drift contribution	$7 \cdot 1.2 \cdot 1.e$
Leakage current fluct. for 2000s	$6e$
Total electronic noise per pixel:	$10e$
Presence of a cosmic (20% of cases)	$12e$
Total Electronic noise per $\Delta\lambda$ (3 spatial pixels)	17 e

Table 5.12: *Noise per pixel per 2000 s.*

z	Blue filter $N_\gamma/s/cm^2$	exposure time
0.5	$1.1\ 10^{-3}$	$588s$
1.5	$1.84\ 10^{-4}$	$18000s$
1.7	$1.48\ 10^{-4}$	$36000s$

Table 5.13: *The number of photons does not take into account the* $0.5 * 0.7$ *efficiency. It is calculated here for a* $M_B = -18.48$ SNIa. *Black curves are only the supernova, red curves include Poisson and electronic noise.*

The simulated supernovæ

In order to simulate SNAP/JDEM exposures, we calibrate the photon flux of each supernovæ to its absolute blue magnitude and then redshift it to the desired z.

$$N_\gamma(z) = N_\gamma(0)(1+z)\frac{d_0^2}{d^2_{luminosity}} \tag{5.23}$$

Eq. (5.23) shows how the number of photons per unit of time and of surface in the B band in the supernova rest frame at z $N_\gamma(z) = \int_{B(z)} \frac{dN_\gamma(z)}{d\lambda} d\lambda$ is related to $N_\gamma(0) = \int_{B(0)} \frac{dN_\gamma(0)}{d\lambda} d\lambda$, the number of photons per unit of time and of surface in the B band at rest in the supernova rest frame for a supernova at $10Pc$.

The flux dilution factor for a supernova at z is $\frac{d_0^2}{d^2_{luminosity}}$ where $d_0 = 10Pc$, but the number of photon takes into account the length dilatation applying to the wavelength through the suppression of a factor $(1+z)$ included in d_L^2.

Finally, we included a procedure to noise the spectra according to tab. 5.3.1.

The electronic noise for each $2000s$ exposure was calculated using eq. (5.24)

$$n^2_{electronic} = 17^2 \cdot \frac{t}{210^3} \tag{5.24}$$

and assumed to be a Gauss function of mean zero. The Poisson noise of the signal was also included for each of the $2000s$ exposures needed to complete the total exposure time.

Name	date	M_{Blue}
SN 1981B	0	-19.07
SN 1986G	-1	-18.08
SN 1989B	-1	-18.58
SN 1991bg	0	-16.62
SN 1991T	0	-19.44
SN 1992A	-1	-18.48
SN 1994D	-3	-19.0

Table 5.14: *Supernovæ simulated in* SNAP/JDEM *context.*

In tab. 5.13 we display the number of photons per second expected in the B Bessel filter for a SNIA of absolute blue magnitude $M_B = -18.48$, not accounting for the CCD and optical transmission. The exposure time we use have been assumed to follow a a $(1+z)^7$ power law with 10 hours for $z = 1.7$.

5.3.2 Results at $z = 1.5$

We display in Fig. 5.12 the standard supernova SN 1992A number of photons per bin simulated for $z = 1.5$ and $z = 1.7$. This quantity differs from the usual flux per Å , which explains the flatter shape of the spectrum as there is a $1/\lambda$ factor difference between them. For $z = 1.7$, the wavelength coverage will be too small to allow the calculation of $\Re_{Si}$ and $\Re_{SiS}$.

We simulated 100 exposures for each one of the supernovæ listed in table 5.14 and calculated the spectral indicators previously defined on each one of them. We then calculated the variance of these measures and, using the linear regression calibrations previously calculated, we estimated the accuracy of the associated luminosity measures.

In order to concentrate on the accuracy of the spectroscopic indicators in SNAP/JDEM, and as at redshifts of ≈ 1 the time dilatation doubles the evolution time of the light curve, we assumed that the spectra will be taken almost at the maximum light time. We thus selected in our sample only the supernovæ spectra that were the closer to the light curve maximum time.

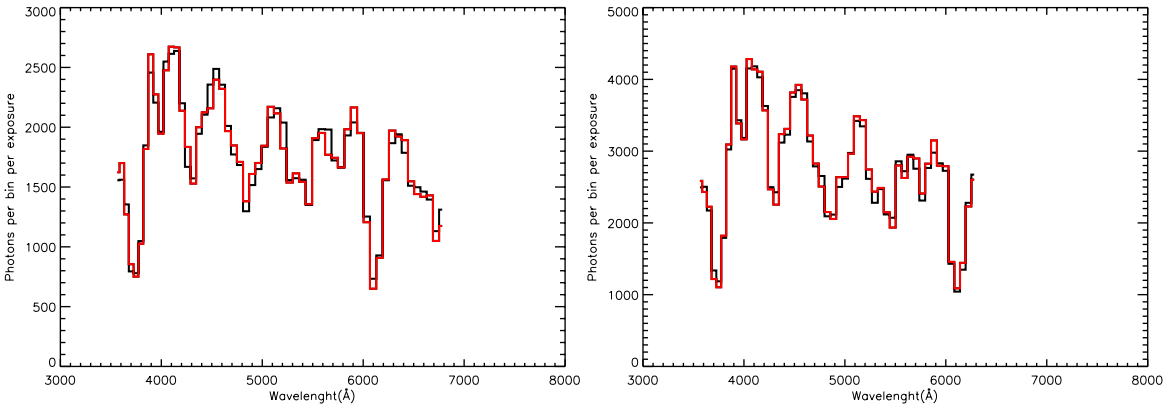

Figure 5.12: ***Left:*** SNAP/JDEM *SN 1992A* $z = 1.5$ *simulated exposure.* ***Right:*** SNAP/JDEM *SN 1992A* $z = 1.7$ *simulated exposure.*

Name	$\Re_{Si}$ mean	$\sigma_{\Re_{Si}}$	measured M_B	ΔM_B	$t=0$ M_B	$t=0$ ΔM_B
SN 1981B	0.318	0.049	-19.10	0.34	-18.94	0.30
SN 1986G	0.312	0.146	-19.14	1.02	-18.97	0.89
SN 1989B	0.352	0.052	-18.86	0.36	-18.73	0.32
SN 1991bg	0.626	0.220	-16.95	1.54	-17.07	1.33
SN 1991T	1.207	0.742	-12.88	5.19	-13.55	4.50
SN 1992A	0.225	0.063	-19.75	0.44	-19.50	0.38
SN 1994D	0.282	0.077	-19.35	0.54	-19.15	0.47

Table 5.15: $\Re_{Si}$ *simulated for z=1.5 and the corresponding blue magnitudes calculated with the previous linear regression. The* $t = 0$ *values have been calculated with the* $t = 0$ *extrapolated linear fits.*

$\Re_{Si}$

We list in tab. 5.15 the luminosities measured on the simulated supernovæ without any selection cut on the simulated $\Re_{Si}$ values. For half of the supernovæ, the $\Re_{Si}$ dispersion due to the noise is of the same order than the intrinsic dispersion calculated previously. We recall that it was $\sigma\Re_{Si} \approx 0.06$, corresponding to $\Delta M_B \approx 0.4$. The distance between the mean blue magnitude measured and the real blue magnitude are listed in tab. 5.16.

The peculiar SN 1991T and SN 1991bg have higher dispersions, and would hinder the global accuracy of the method unless extracted of the sample. Doing so spectroscopically would be feasible with a large SNeIa spectra library, thus preventing the need to use the light curves, keeping this method completely independent.

The total variance of $\Re_{Si}$ can be estimated to be $\sigma_{tot} \approx \sqrt{2}\ \sigma_{\Re_{Si}}$, where $\sigma_{\Re_{Si}}$ stands for

Name	Distance of measured M_B to true M_B	Distance of time corrected M_B to true M_B
SN 1981B	0.03	0.13
SN 1986G	1.06	0.89
SN 1989B	0.28	0.15
SN 1991bg	0.33	0.45
SN 1991T	6.56	5.89
SN 1992A	1.27	1.02
SN 1994D	0.35	0.15

Table 5.16: $\Re_{Si}$ *measured* M_B *distance to the true* M_B

the dispersion due to the noise, the $\sqrt{2}$ factor coming from the intrinsic dispersion being of the same order than the one due to the noise.

z	0.6	0.7	0.8	0.9	1.0	1.1	1.2	1.3	1.4	1.5	1.6	1.7
SNAP	150	171	183	179	170	155	142	130	119	107	94	80

Table 5.17: *Number of supernovæ expected in function of redshift for* SNAP/JDEM.

As shown in tab. 5.17, SNAP/JDEM is expected to find ≈ 107 SNeIa at $z = 1.5$. The accuracy expected on the luminosity measure with $\Re_{Si}$ would then be statistically improved by a factor of $\sqrt{107} \approx 10$. The resulting blue magnitude dispersion for the "Branch Normal" supernovæ using the 107 spectra expected by SNAP/JDEM at $z = 1.5$ will thus be $\sqrt{2}/\sqrt{107}\sigma_{M_B}$, ranging from ≈ 0.06 to ≈ 0.27, for the time corrected calibration. The SN 1991T would even have a dispersion as hight as $\sigma_{M_B} \approx 0.85$

The time correction decreases the distance between the measured and real blue magnitude, and also increases the accuracy of the measure by increasing the slope of the correlation. In order to take full advantage of this luminosity measure, we need spectra as close as possible to the maximum light time, which will be feasible at $z = 1.5$ since the elapsed time between -1 and $+1$ days around maximum is $2.5 \cdot 2 = 5$ days.

$\Re_{SiS}$

Calculating $\Re_{SiS}$, it appeared that $\Re_{SiSS}$ was not improving results as expected from the previous section. This is due to the SNAP/JDEM large wavelength binning that already transforms $\Re_{SiS}$ in an "integral" ratio compared to the 10Å binning we previously used. We thus displayed in tab. 5.18 only $\Re_{SiS}$, $\Re_{SiSS}$ results being almost identical, and some

Name	$\Re_{SiS}$ mean	$\sigma_{\Re_{SiS}}$	measured M_B	ΔM_B	$t=0$ M_B	$t=0$ ΔM_B
SN 1981B	0.774	0.020	-18.86	0.09	-19.0627	0.096
SN 1986G	1.059	0.040	-17.65	0.17	-17.7442	0.185
SN 1989B	0.828	0.035	-18.63	0.15	-18.8119	0.163
SN 1991bg	0.862	0.115	-18.48	0.49	-18.6550	0.532
SN 1991T	0.668	0.019	-19.31	0.08	-19.5546	0.090
SN 1992A	0.878	0.039	-18.41	0.17	-18.5795	0.185
SN 1994D	0.766	0.027	-18.89	0.12	-19.0990	0.129

Table 5.18: $\Re_{SiS}$ *simulated for z=1.5 and the correspondent blue magnitudes calculated with the previous linear regression. The* $t=0$ *values have been calculated with the* $t=0$ *extrapolated linear regression.*

Name	Distance of measured M_B to true M_B	Distance of time corrected M_B to true M_B
SN 1981B	0.21	0.01
SN 1986G	0.43	0.34
SN 1989B	0.95	0.23
SN 1991bg	1.86	2.03
SN 1991T	0.13	0.11
SN 1992A	0.07	0.1
SN 1994D	0.11	0.1

Table 5.19: $\Re_{SiS}$ *measured* M_B *distance to the true* M_B

times a bit worse because the larger SNAP/JDEM binning tended to include more of the FeII ≈ 5600Å peak into the integral, hindering its quality.

Table tab. 5.18 lists the measured blue magnitudes with 100 supernovæ, and the dispersion due to the noise. Besides from SN 1991bg that has been excluded from the calibration, the luminosity measure dispersion is always lower than 0.2 blue magnitudes.

As can be seen from tab. 5.19, the intrinsic dispersion of the supernovæ is of the same order than the variance due to the noise for this line ratio, multiplying the error on the blue magnitude by $\approx \sqrt{2}$. Using all the supernovæ expected to be found by SNAP/JDEM at $z = 1.5$ would again allow to increase the accuracy on the mean blue magnitude determination by a factor of $1/\sqrt{107}$. The resulting dispersion taking into account the time correction will then range from $\Delta M_B \approx 0.017$ to $\Delta M_B \approx 0.037$, which is within the requirements for SNAP/JDEM to measure ω_0 and ω_1 independently, and constrain the evolution of SNeIa.

Name	$\Re_{Ca}$ mean	$\sigma_{\Re_{Ca}}$	measured M_B	ΔM_B	Distance to real M_B
SN 1981B	1.196	0.053	-19.05	0.09	0.97
SN 1989B	1.059	0.041	-19.29	0.07	0.71
SN 1991bg	2.474	0.633	-16.78	1.12	0.16
SN 1991T	0.877	0.022	-19.61	0.03	0.17
SN 1992A	1.279	0.061	-18.90	0.10	0.42
SN 1994D	1.279	0.048	-18.90	0.08	0.1

Table 5.20: $\Re_{Ca}$ *simulated for z=1.5 and the corresponding blue magnitudes calculated with the previous calibrations.*

$\Re_{Ca}$

As for $\Re_{SiSS}$, $\Re_{CaS}$ has a smaller dispersion due to the noise, but a larger calibration error because of the too coarse SNAP/JDEM binning. We thus only display $\Re_{Ca}$ results in this section.

Table 5.20 summarizes the luminosity measure precision estimated for $\Re_{Ca}$. Besides from SN 1991bg and SN 1981b, the dispersion due to the noise is much lower than the $\sigma\Re_{Ca} \approx 0.25$ intrinsic dispersion estimated previously. The last column of the table even shows the mean intrinsic dispersion is $\sigma_{\Re_{Ca}} \approx 0.5$. The accuracy of a luminosity measure using $\Re_{Ca}$ is then $\Delta M_B \approx 0.95$ for the "Branch Normal" supernovæ. Using the 107 supernovæ SNAP/JDEM is supposed to find at $z = 1.5$, the final accuracy of the $\Re_{Ca}$ luminosity measure will thus be $\Delta M_B \approx 0.09$ which is not enough for the cosmological requirements, even if it remains a good way to probe the evolution effects, as the final result on the mean blue magnitude is of the same order of the intrinsic dispersion of the "Branch Normal" supernovæ.

5.3.3 Evolution with z

As was show earlier, SNAP/JDEM wavelength coverage does not allow to use $\Re_{Si}$, nor $\Re_{SiS}$ for $z = 1.7$. On the other hand $\Re_{Ca}$ will be measurable. Moreover, since the exposure time has been calculated so that the number of photons per bin will remain almost the constant, the signal to noise will not be degraded too much. The dispersion due to the noise can be seen in tab. 5.21 to remain small compared to the intrinsic dispersion of the supernovæ.

$\Re_{Ca}$ blue magnitude accuracy remains dominated by the intrinsic dispersion of the supernovæ corresponding to $\Delta M_B \approx 1$. This result can again be improved by using the 80

Name	$\Re_{Ca}$ mean	$\sigma_{\Re_{Ca}}$	measured M_B	ΔM_B	Distance to real M_B
SN 1981B	1.34	0.037	-18.79	0.07	0.71
SN 1989B	1.05	0.037	-19.28	0.07	0.7
SN 1991bg	2.87	0.83	-16.07	1.48	0.55
SN 1991T	0.80	0.01	-19.74	1.43	0.3
SN 1992A	1.36	0.05	-18.75	0.09	0.27
SN 1994D	1.25	0.04	-18.94	0.07	0.06

Table 5.21: $\Re_{Ca}$ *simulated for z=1.7 and the corresponding blue magnitudes calculated with the previous calibrations.*

Table 5.22: Results for the new regressions using the (Reindl et al., 2005) magnitudes and the $-19.6 > M_B > 19.0$ SNeIa sub sample.

	Slope(a)	Variance (σ)	$\sigma_{M_B} = \sigma/a$
$\Re_{Ca}$	2.13	0.22	0.10
$\Re_{CaS}$	3.15	0.31	0.10
$\Re_{Si}$	0.75	0.05	0.07
$\Re_{Si}$ $t = 0$ extrapolation	0.79	0.06	0.07
$\Re_{SiS}$	0.67	0.06	0.09
$\Re_{SiS}$ $t = 0$ extrapolation	0.66	0.03	0.04
$\Re_{SiSS}$	0.73	0.06	0.09
$\Re_{SiSS}$ $t = 0$ extrapolation	0.80	0.04	0.05

supernovæ expected. The blue magnitude precision would then be $\Delta M_B \approx 0.11$, which is still of the same order of the intrinsic dispersion of the "Branch Normal" blue magnitude.

5.4 Addendum

As discussed in chapter 4.4, (Reindl et al., 2005) propose a new set of absolute magnitudes for the supernovæ with improved host reddening corrections which decrease the "Branch normal" supernovæ luminosity scatter. The magnitudes we quoted do *not* include any SNeIa standardization, i.e. do not correct for any intrinsic properties of the supernovæ.

In this addendum we restrict ourselves to the $-19.6 > M_B > -19.0$ range, excluding the "91T like" and "91bg like" supernovæ presenting more uncertain corrections. This is, as already pointed out, consistent with observational constraints since the "91T and 91bg like" supernovæ have specific spectral characteristics.

We also use the favored -19.16 blue magnitude for SN 1986G from (Reindl et al., 2005), as it lies within our luminosity range.

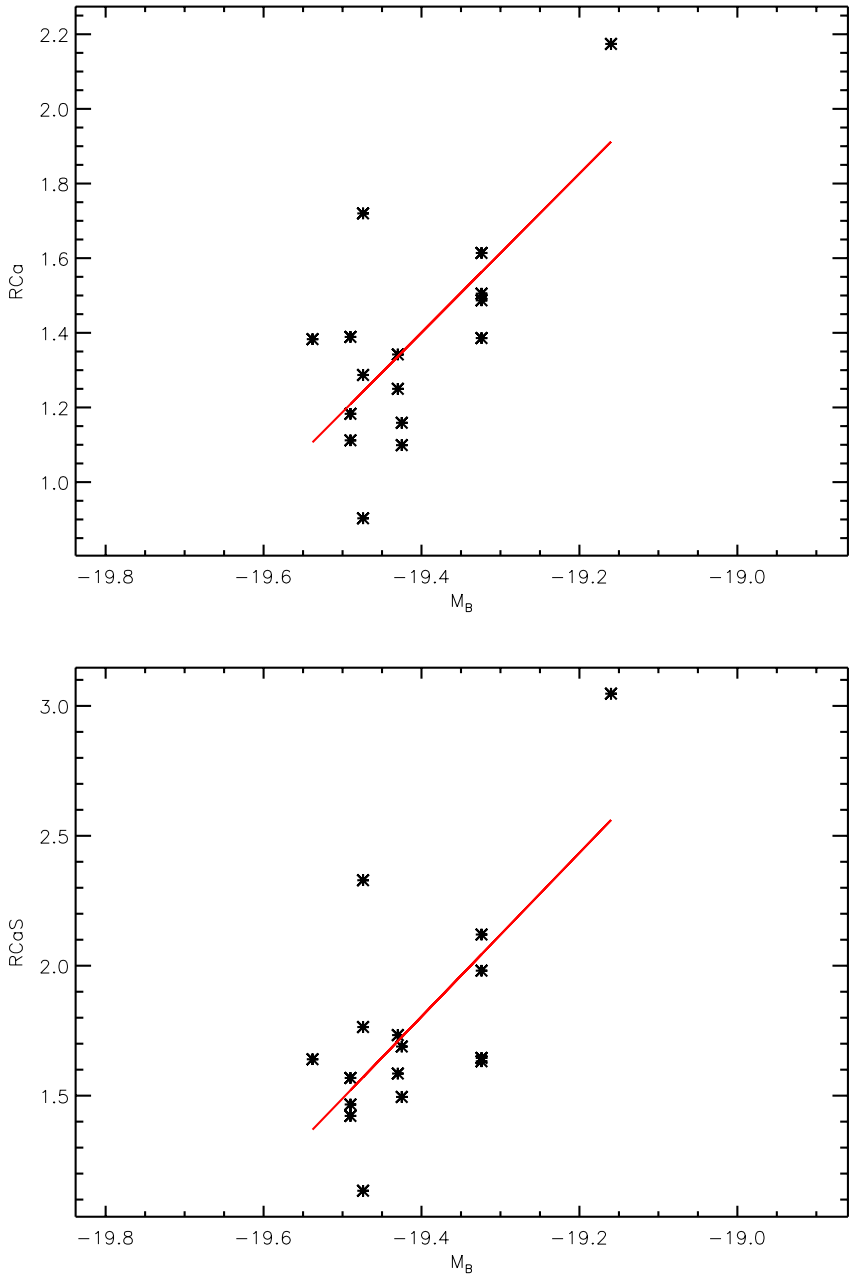

Figure 5.13: $\Re_{Ca}$ calculated using the sub sample of thesupernovæ listed in Table 2 corresponding to $-19.6 < M_B < -19$(Top panel). Idem for $\Re_{CaS}$ (Bottom panel).

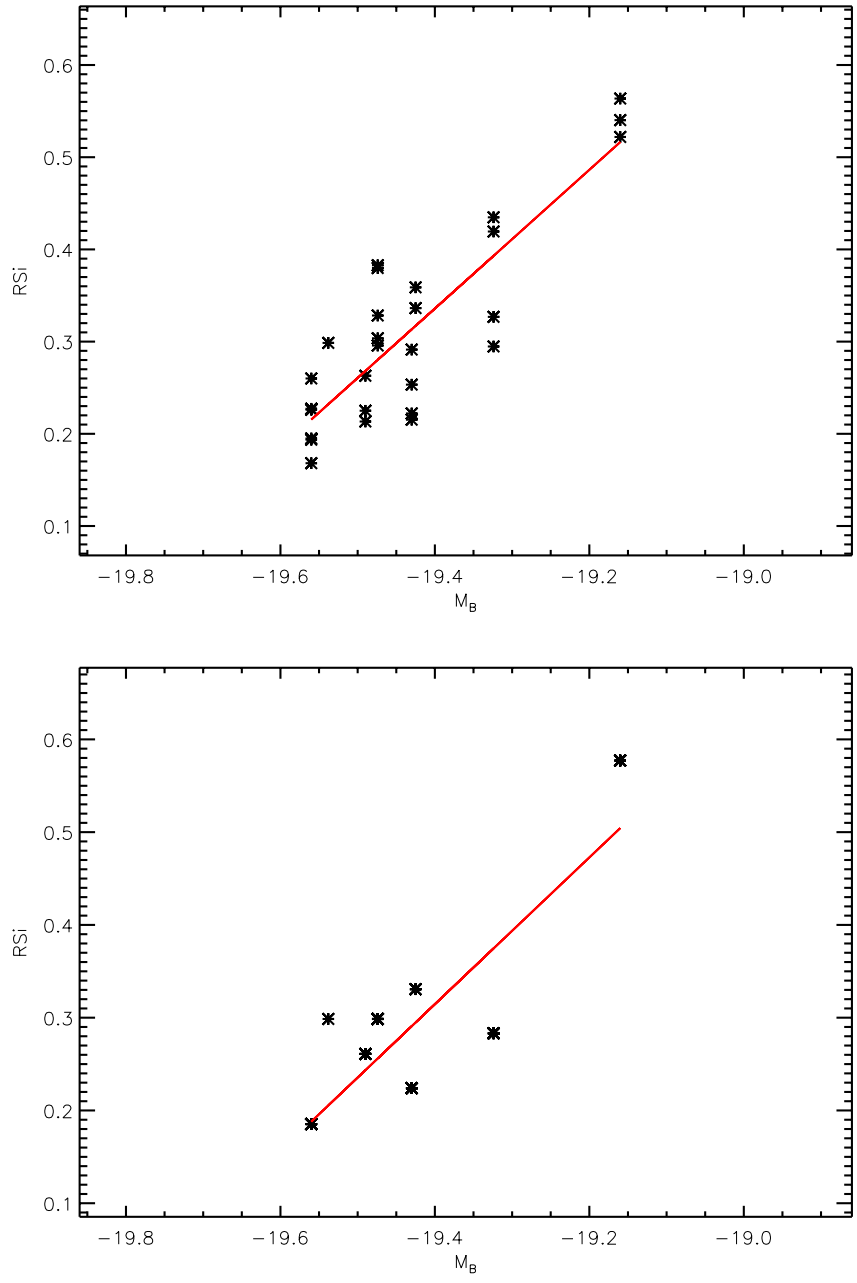

Figure 5.14: $\Re_{Si}$ calculated using the sub sample of thesupernovæ listed in Table 2 corresponding to $-19.6 < M_B < -19$(Top panel). Idem for $\Re_{Si}$ with $t = 0$ extrapolated values (Bottom panel).

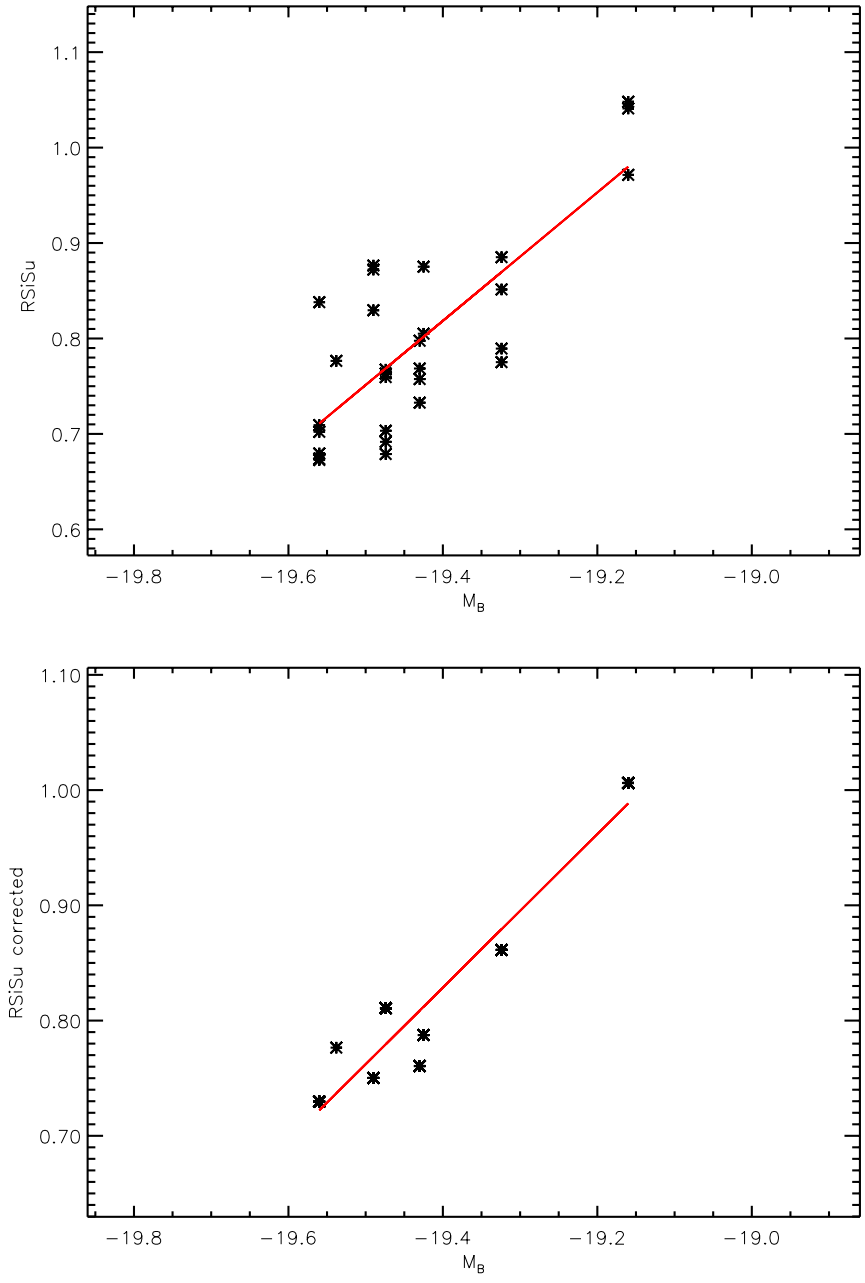

Figure 5.15: $\Re_{SiS}$ calculated using the sub sample of thesupernovæ listed in Table 2 corresponding to $-19.6 < M_B < -19$(Top panel). Idem for $\Re_{Si}$ with $t = 0$ extrapolated values (Bottom panel).

We display in fig. 5.13, fig. 5.14 and fig. 5.15 the linear regressions calculated on this subsample. Table 5.22 lists the new slopes, variances and accuracy on the blue magnitude measures using these ratios. As the slopes are systematically larger, the accuracy of the method improved for all the ratios and is lower than ± 0.1 blue magnitude in each case.

It is seen in fig. 5.13 and fig. 5.14 that the correlation hinges on the inclusion of SN 1986G at $M_B = -19.16$. The case of $\Re_{SiS}$ in fig. 5.15 is stronger, as its linear regression would not suffer too much from the exclusion of SN 1986G.

In the SNAP/JDEM context, the increase in the slopes leads to better accuracy too. For $\Re_{Si}$ the accuracy becomes $\sigma_{M_B} \approx 0.1$, for $\Re_{Ca}$ it $\sigma_{M_B \approx 0.14}$ and for $\Re_{SiS}$ $\sigma_{M_B \approx 0.06}$ blue magnitudes.

The dispersions quoted include both the noise and the intrinsic SNeIa dispersion. With a statistic of ≈ 100 supernovæ observed, each one of these ratio can be used for cosmological studies within SNAP/JDEM requirements.

The luminosity range may be extended in the future, but no significant loss of statistics is expected from the restriction to $-19.6 < M_B < -19.0$. In this restricted range $\Re_{Ca}$ and $\Re_{Si}/\Re_{SiS}$ are independent luminosity indicators with an accuracy comparable to the stretch/Δm_{15} one, and, $\Re_{SiS}$ remains potentially twice as accurate as $\Re_{Si}$.

Chapter 6

Line formation, study of the $\Re_{Si}$ region

In this chapter we shall investigate the line formation process in type Ia supernovæ around blue maximum light using day 20 after explosion PHOENIX spectra from our simulated grids. We remind that for the full grid, the date ranges from 10 to 25 days after explosion, and the luminosity from -18.17 to to -19.7 blue magnitude. In this chapter we will concentrate on the solutions corresponding to 20 days after explosion as this date is the canonical maximum light time, and it has been shown in Lentz et al. (2001) that it is the time after explosion at which PHOENIX reproduces the best SN 1994D maximum light spectrum with W7 model.

We also dwell on the -18.17 blue magnitude spectrum because our starting point was the TiII effects on $\Re_{Si}$, and TiII is know to be more important in lower luminosities supernovæ.

6.1 The TiII issue in the $\Re_{Si}$ zone

The existence of the $\Re_{Si}$ correlation with luminosity incites to think of the 5500Å-6500Å region as a possible "Rosetta stone" for the line formation analysis since a change in the blue magnitude is correlated to the observed spectrum in that wavelength range.

In Fig. 6.1 we display the $\Re_{Si}$ region, the two green lines marking the 6355 Å and 5979 Å SiII emission lines. Attributing the 6100Å &5800Å troughs to the P-Cygni profiles of

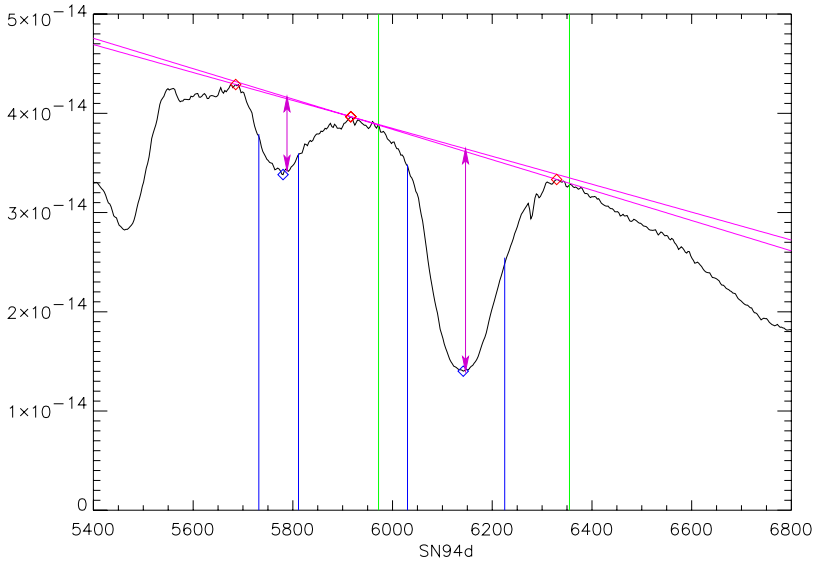

Figure 6.1: $\Re_{Si}$ *region. Green lines label the* 6355 *Å and* 5979 *Å lines.*

these two lines is therefore very appealing. These two lines however share the 4P level, the 6355 Å line as the 4S-4P transition and the 5979 Å as the 4P-5S one.

Their optical depth can be estimated in the Sobolev approximation using eq. (6.1) from Hatano et al. (1999), where n_l and n_u stand for the number densities of the lower and upper level associated to the transition, f for its oscillator strength, t for the time since explosion, g_l and g_u for the level degeneracy state, and λ for the wavelength.

$$\tau = (\frac{\pi e^2}{mc}) f \lambda t n_l [1 - \frac{g_l n_u}{g_u n_l}] \tag{6.1}$$

The ratio of the SiII 6355 Å line optical depth (τ_{red}) over the SiII 5979 Å line optical depth (τ_{blue}), using the Boltzmann level population equation, and the fact that they share the intermediate 4P level becomes:

$$\frac{\tau_{red}}{\tau_{blue}} \propto \frac{e^{\frac{\Delta_{E_{red}}}{k_B T}} - 1}{1 - e^{\frac{\Delta_{E_{blue}}}{k_B T}}} \tag{6.2}$$

Where ΔE is the difference between the transition upper and lower level's energy.

This optical depth ratio decreases monotonically with respect to a temperature increase. We display this effect in Fig. 6.2, where we used SYNOW to compute SiII spectra for

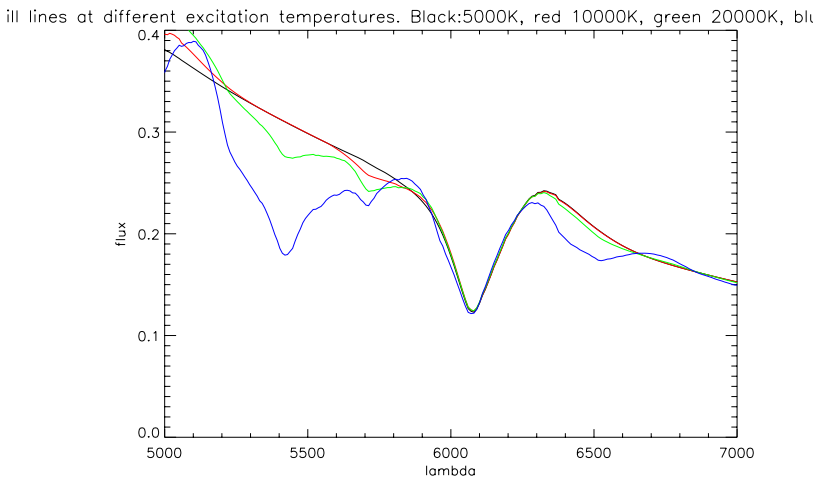

Figure 6.2: *Si*II *in* SYNOW *with different excitation temperatures. Black* $5000K$*, red* $10000K$*, green* $20000K$*, blue* $40000K$*.*

excitation temperatures ranging from $5000K$ to $40000K$.

Since P-Cygni troughs become deeper with increasing optical depth, a higher SiII excitation temperature will affect the ≈ 5700Å / ≈ 6100Å depth ratio, causing $\Re_{Si}$ to increase. If SNeIa at higher luminosities have higher SiII excitation temperatures[1] $\Re_{Si}$ should then increase and not decrease with luminosity as observed for real supernovæ.

Fig. 6.3 displays the temperature evolution in the 9000-16000km.s^{-1} region, where SiII is found, and shows that the physical temperature increases with bolometric luminosity as one would expect. In LTE this means that the SiII excitation temperature increases with luminosity, which we will consider to be the case for real supernovæ, even if we cannot exclude NLTE effects, or less intuitive temperature behaviors with different abundance structures.

SiII lines alone are thus unable to explain the trend of the $\Re_{Si}$ correlation with luminosity. Garnavich et al. (2001) proposed the TiII line, which P-Cygni trough would form at the same place than the 5979 Å SiII line, as an alternate explanation.

6.1.1 SYNOW fit of a PHOENIX spectra

In order to investigate the line formation process in the $\Re_{Si}$ 5500Å -6400Å region, we applied to the -18.17 bolometric luminosity spectrum of our PHOENIX synthetic spectra

[1]Which might not be the case, if for example the luminosity increase makes the temperature structure much steeper, or if NLTE effect enter the game.

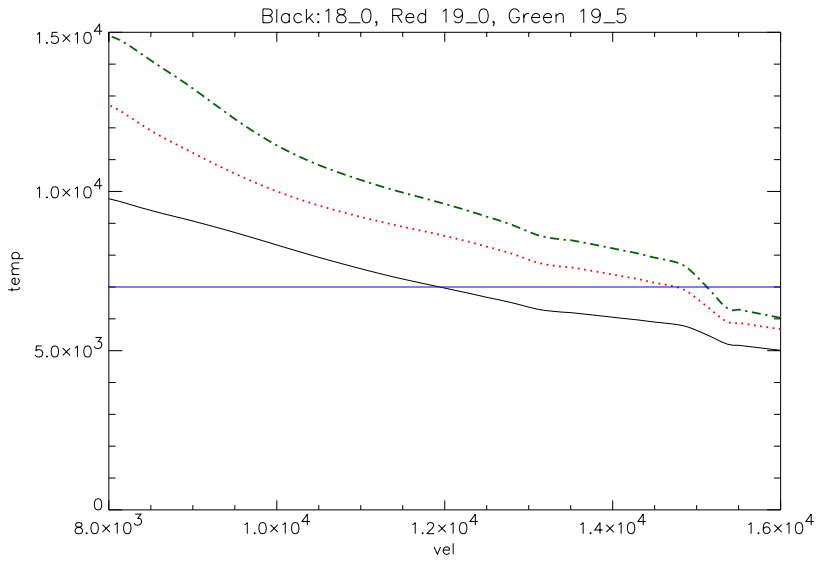

Figure 6.3: *Temperature evolution for* -18.17*(black),* -19.17*(red) and* -19.5*(green) blue luminosities* PHOENIX *spectra in the* 8000-16000$km.s^{-1}$ *region where Si*II *ions are found.*

grid for 20 days after maximum the method usually used for real supernovæ.

We fitted this wavelength zone with SYNOW, first using only SiII lines, and then adding TiII lines. The results are plotted in Fig. 6.4. For SiII lines alone we concentrated on the ≈ 6100Å trough fit, and for TiII lines alone on the ≈ 5600Å one.

On the top three panels of Fig. 6.4, we see that the ≈ 6100Å trough is well fitted, and that there are no worrying features for a more complete fits. In the SYNOW fit procedure, a "worrying feature" is a deep absorption trough not present in the fitted spectrum. Since SYNOW only treats pure scattering, these troughs are known to be usually impossible to fill up with other chemical species. The ≈ 9000Å absorption feature could be one of these, but as the PHOENIX spectrum drops steeply after 9000Åwe considered it not to be critical issue.

The same remark applies to the lower three panels, as we find no optical depth and excitation temperature combination for TiII lines that allowed to fit the ≈ 5600Å trough without the ≈ 9300Å absorption feature.

The final parameter values for these fits are summarized in tab. 6.1.1. While it has not been possible to fit both the ≈ 6100Å and the ≈ 5600Å trough with only SiII lines,

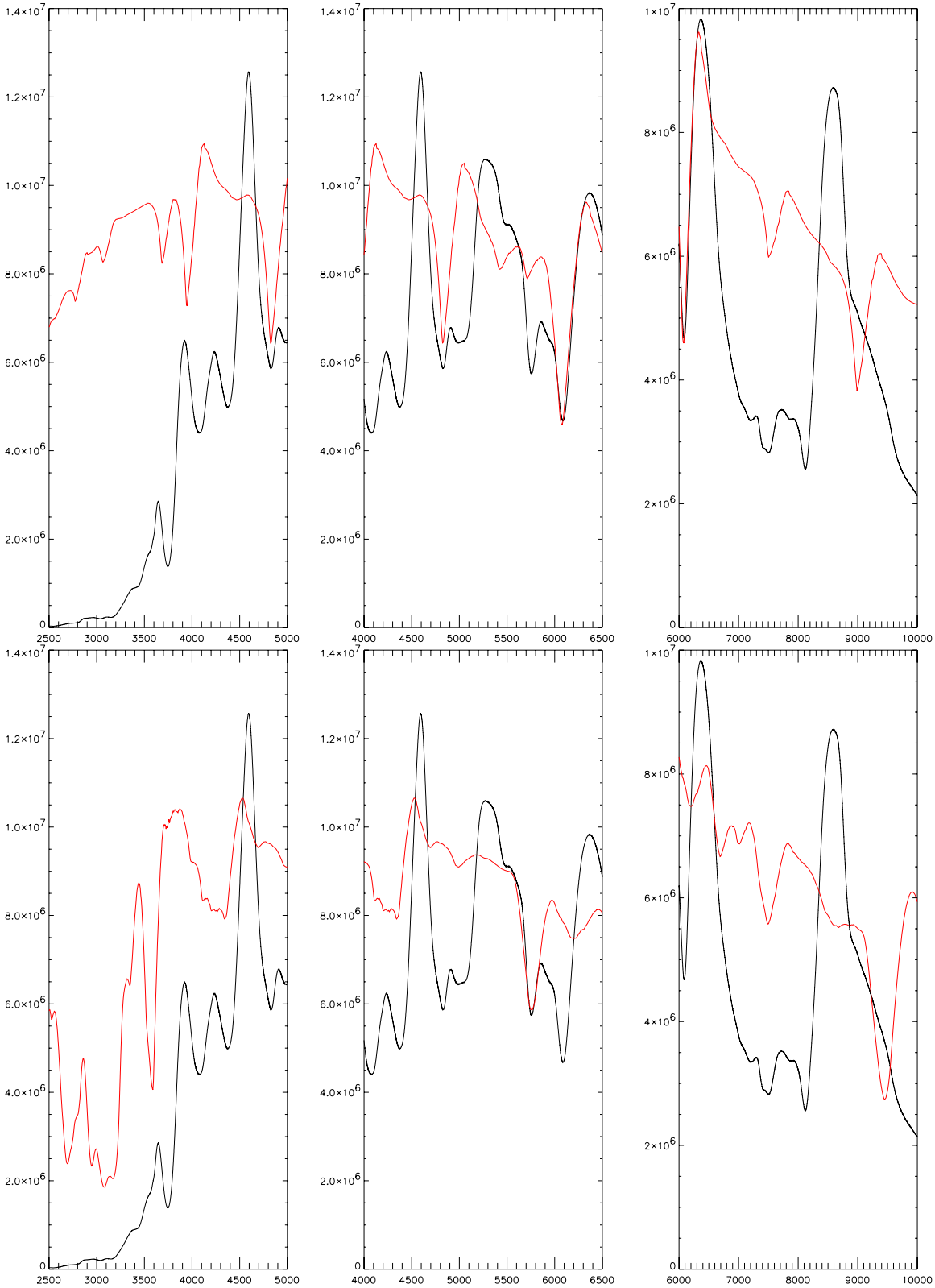

Figure 6.4: *Black curve:* PHOENIX *spectra. Red curve* SYNOW *fit. Top: only* Si II *lines used to fit the* $\approx 6100\mathring{A}$ *trough. Bottom: only* Ti II *lines used to fit the* $\approx 5600\mathring{A}$ *trough*

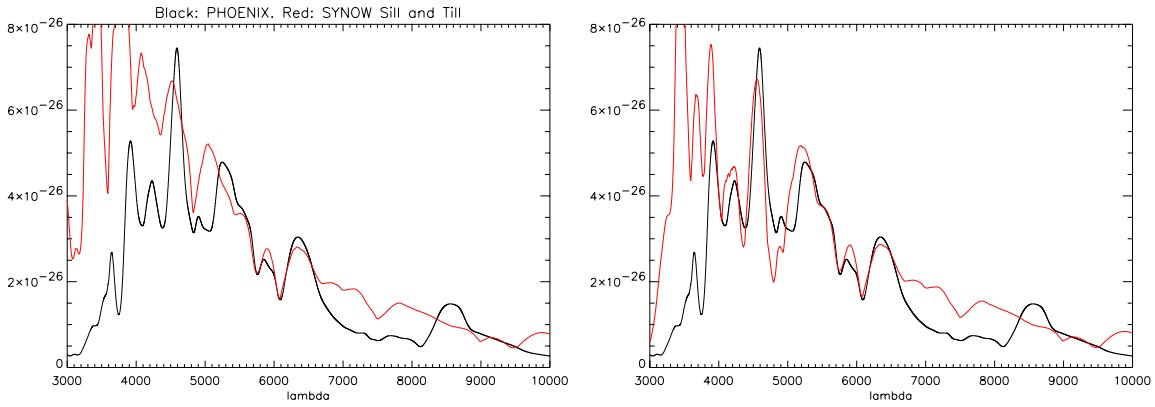

Figure 6.5: ***Left:*** *Black curve:* PHOENIX *spectra. Red curve* SYNOW *fit of the* $5500-6500\AA$ *wavelength region with* Ti II *and* Si II. ***Right:*** *Black curve:* PHOENIX *spectra. Red curve* SYNOW *fit with* Ti II Si II *and* Fe II.

combining them to Ti II reproduced qualitatively this wavelength region as can be seen in Fig. 6.5. We also display in the right hand side of the same figure that the fit is improved by adding Fe II lines, in particular around the $\approx 5300\text{Å}$ peak and the $4000-5000\text{Å}$ wavelength region.

Photosphere velocity	14000km.s^{-1}
Black body temperature	$12000K$
$\tau_{Si\,II}$	9
Si II excitation Temperature	$9000K$
$\tau_{Ti\,II}$	8
Ti II excitation Temperature	$18000K$
$\tau_{Fe\,II}$	1.5
Fe II excitation Temperature	$12000K$
$\tau_{Ca\,II}$	60
Ca II excitation Temperature	$14000K$
$\tau_{Co\,II}$	4
Co II excitation Temperature	$7000K$

Table 6.1: SYNOW *fit parameters*

Ti II is thus a good candidate to explain the $\Re_{Si}$ correlation with luminosity, since as stated in Garnavich et al. (2001) its 5979 Å line strength increases with temperature, and since the combination of Si II and Ti II lines reproduce well the $\Re_{Si}$ spectral region. The poor quality of the fit at $\lambda < 4000\text{Å}$ shows that we miss some contribution which will be shown to be a non trivial problem. But we have shown that Si II and Ti II lines *can* be used to fit well the $\Re_{Si}$ wavelength region. We shall now proceed with PHOENIX to show that such an assignement is erroneous.

6.1.2 Single Element spectra

Since the fitted spectrum was not a real supernova but a PHOENIX synthetic spectrum, the output also contained all the detailed information pertinent to the line formation issue. In particular it allowed us to compute "single element spectra" as follows.

Using the converged output of the PHOENIX simulation, we artificially turn off *all* but the continuum and one single element lines opacities. We recall that the "continuum opacities" denote all the bound-free and free-free opacities as well as the electron scattering and the Rayleigh scattering. We can also compute "multiple element spectra" where we turn off all but two or more elements lines opacities, but we will abusively group all these different spectra in the same "single element spectra" denomination.

Once the chemical species selected, we recalculate the solution of the radiative transfer equation in order to get the spectrum, with the level populations and free electrons number kept fixed. Since the solution of the scattering problem is recalculated, the"single element spectra" is *not* the exact contribution of the element to the complete spectrum[2]. The relative strength of the absorption features give a good indication on each line optical depth, but since the source functions change, the features are *not* expected to look exactly the same as in the complete spectrum. True emission ,depending only on the level populations kept fixed, will not change, while the scattering part of the emission peaks will. The ratio of true emission over scattering is thus different in the "single element spectra".

As the overall opacity is decreased in the "single element spectrum", the flux transfer to the red due to scattering will be underestimated, and the "single element spectra" will tend to appear bluer than the complete spectrum.
With only a single iteration over the radiative equation loop, the energy conservation is not enforced anymore, since the opacities changed so dramatically, and the "single element spectra" can not be considered as normalized consistently in flux anymore.

The TiII issue

[2]Ergo, the complete spectrum is NOT the linear combination of all the single element spectra.

TiII and SiII single element spectra: In Fig. 6.1.2 we display the -18.17 blue magnitude spectrum together with the corresponding "only SiII" and "only TiII" single element spectra. The "single element spectrum" where all the element lines have been turned off is also plotted as a reference, and more will be said about this case in sec 6.2.1. Compared to this "only continuum opacity" spectrum, the "only TiII lines" spectrum shows that there are no significant TiII lines in the $\Re_{Si}$ 5300-6500Å wavelength zone for the PHOENIX spectrum, even though SYNOW fitted this region adequately with TiII and SiII.

In Fig. 6.7 we display the 6355 Å SiII and the 5979 Å TiII line optical depth. The 6355 Å SiII line optical depth is five times higher than the 5979 Å SiII one which peaks at $\tau \approx 20$. It results into a larger scattering power, which we see in Fig. 6.1.2, where for comparable underlying continuum level, the redder line emission peak is higher and wider than the bluer one.

Since the 5979 Å SiII line optical depth peaks at $\tau \approx 20$, and since it forms in the same velocity range than the TiII line, $\tau_{\rm TiII}$ would have to be of comparable magnitude to have a direct impact on the ≈5979 Å wavelength region. In the considered situation, this line is thus not only too weak to appear in the spectrum, but also completely shielded by the 5979 Å SiII line.

Many TiII lines appear in the < 5000Å region of Fig. 6.1.2, proving that their lack of contribution to the ≈ 5300Å wavelength region is neither an abundance nor an ionization effect. There is enough titanium in the TiII ionization stage for its lines to show up in the spectrum.

Fig. 6.7 shows the TiII ≈5979 Å line to form in the 12000km.s^{-1}/15000km.s^{-1} velocity range at a temperature of $\approx 7000K$, as read on the black curve of Fig. 6.3. Garnavich et al. (2001) have shown the TiII 5979 Å line to become stronger than the SiII one for $T \geq 7000K$, and claimed it to become preponderant in lower temperature spectra.

We display in Fig. 6.8 the TiII and SiII lines "single element PHOENIX spectra", and the SYNOW simulations with the same physical parameters as in the complete fit, with only the same corresponding element. We see that SiII SYNOW and PHOENIX spectra are qualitatively close, whereas the TiII spectra only qualitatively agrees at $\lambda < 5000$Å .

We fitted the TiII PHOENIX "single element spectrum" with SYNOW. Fig. 6.9 displays

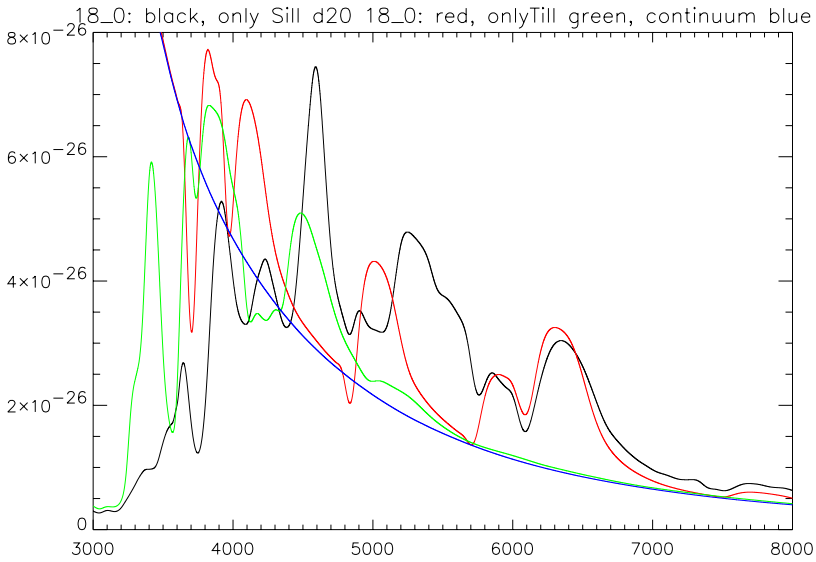

Figure 6.6: *Black curve:* PHOENIX *spectrum. Red curve* PHOENIX *only Si*II *spectrum. Green curve* PHOENIX *only Ti*II *spectrum. Blue curve* PHOENIX *only continuum lines spectrum*

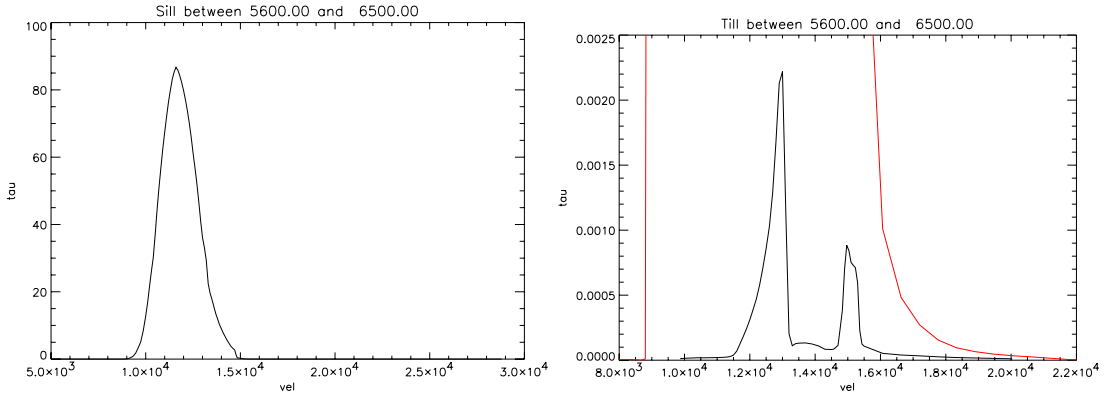

Figure 6.7: ***Left:*** *Si*II 6355 *Å line optical depth.* ***Right:*** *Si*II *and Ti*II *and* 5979 *Å line optical depth*

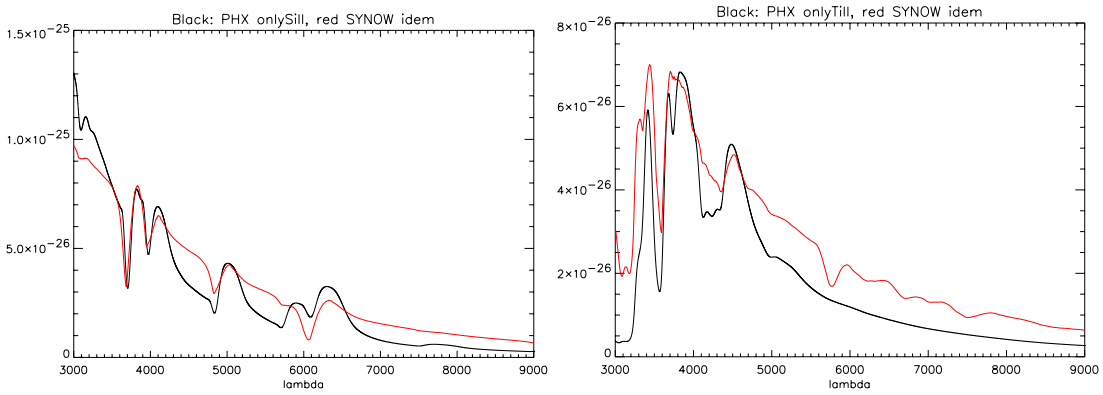

Figure 6.8: *Si*II *only(left) and Ti*II *only(right) for* PHOENIX *(black) and* SYNOW *(red).*

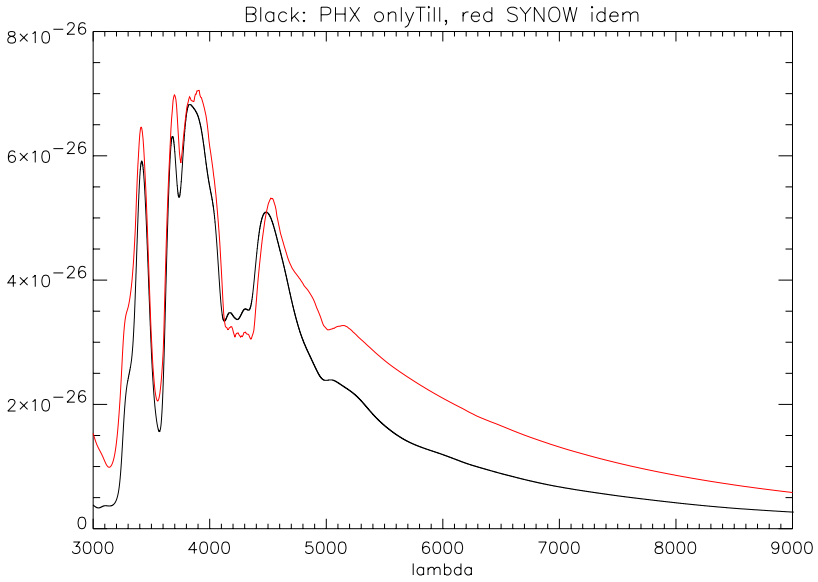

Figure 6.9: *Ti*II SYNOW *and* PHOENIX *spectra,* $\tau_{TiII=120}$, $T_{ex} = 6000K$.

the result where $\tau_{\rm TiII} = 120$ and $T_{ex} = 6000K$, in complete agreement with PHOENIX physical parameters, since the TiII reference line in SYNOW is $\lambda_{TiII} = 3349.408$Å . The fit is of good quality for the whole spectrum, besides from the systematic too high SYNOW flux above 4300Å , due to the absence of energy conservation equation in SYNOW.

At the excitation temperature of $6000K$, the ≈5979 Å TiII line is negligible in SYNOW too, even though the excitation temperature is lower than $7000K$. Even if the TiII 6013Å line strength relative to the SiII 6355 Å one increases when the temperature decreases as stated in Garnavich et al. (2001), it does not mean that the TiII 6013Å line has to show up in the spectrum, since the 6355 Å SiII line strength decreases along with temperature.

Even though TiII can fit the ≈ 5800Å $\Re_{Si}$ trough in SYNOW, it needs different physicals condition than in the the converged PHOENIX simulation. Since we were able to correctly fit the TiII "single element" spectrum with SYNOW, the conclusion is *not* that SYNOW is wrong, but that its use for line identification requires some care, especially when only one spectral feature is fitted.

6.2 The "multi-layered spectrum formation"

Now that TiII line contribution to the ≈ 5800Å $\Re_{Si}$ trough has been ruled out, we shall investigate the line formation process in the PHOENIX computation.

6.2.1 Line formation in the $\Re_{Si}$ zone for the -18.17 blue magnitude PHOENIX spectrum

The continuum opacity spectrum

We display in Fig. 6.10 the spectrum calculated with all but the continuum opacities have been turned off. This spectrum forms at ≈ 5300km.s^{-1} where the mean continuum optical depth is approximately equal to one and the temperature equal to $13700K$ as can be read from Fig. 6.3.

We plot in the same figure the associated black body spectrum and the full PHOENIX spectrum. The black body and the continuum "single element spectrum" are normalized to the full spectrum integral. Since for "single element spectra" we only recalculate the

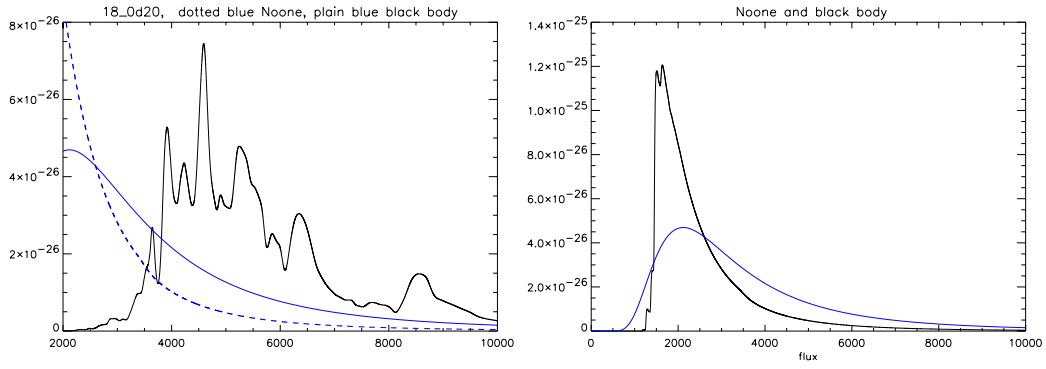

Figure 6.10: ***Left:*** *Full* PHOENIX *spectrum in black, continuum "single element spectrum" in dotted blue,* $13685K$ *black body in plain blue.* ***Right:*** *continuum "single element spectrum" in dotted blue, and* $13685K$ *black body in plain blue.*

radiative transfer equation solution with the temperature structure fixed, the bolometric luminosity is not the same as for the full PHOENIX spectrum. Nevertheless, reconverging the temperature structure would be too much of a change for the "single element spectra" to then be interpreted.

The left hand side of Fig. 6.10 shows that even as deep as 5300km.s^{-1} where the continuum "single element spectrum" form there is no such thing as a *photospheric black body.* This figure emphasizes the flux transfer toward the red in rapidly expanding atmospheres, showing against intuition that type Ia supernovæ spectra are not at first order a black body spectrum carved by some atomic lines.

The right hand side of the same figure displays only the black body and the continuum "single element spectrum" stresses the fact that even at continuum optical depth $\tau_{continuum} \approx 1$, the spectrum is *not* a Planck function. The continuum opacity sources can even display what looks like line features, as can be seen at ≈ 2000Å and ≈ 1900Å.

FeIII lines

The elements presenting strong individual lines or lines blends, forming at approximately the same velocity than the continuum "single element spectrum" modify its shape. FeIII is a major contributor to this next "layer" of the spectrum formation with both strong and numerous weak lines. All their optical depth peak at $v_{\text{FeIII}} \approx 6000\text{km.s}^{-1}$ as shown for the particular strong 5128Å line in the left hand side of Fig. 6.11. A distinction has to be made

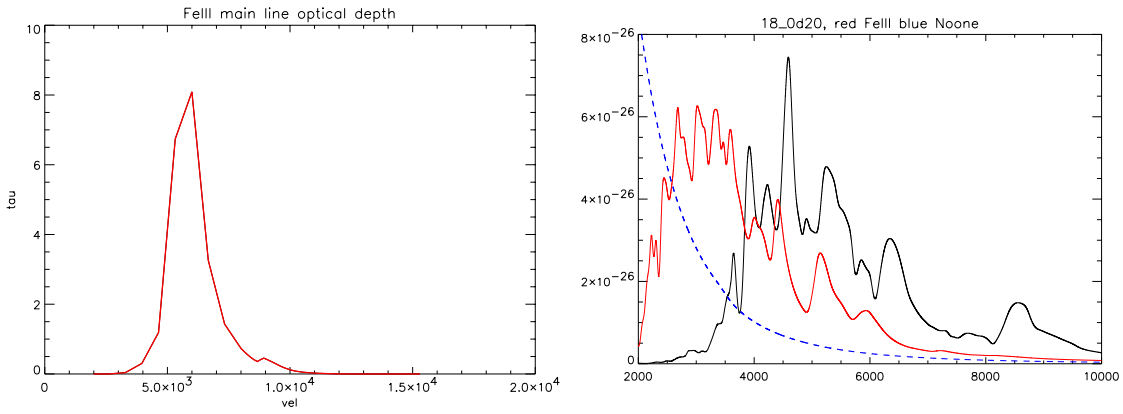

Figure 6.11: ***Left:*** *FeIII 5128Å line optical depth.* ***Right:*** *full spectrum in black. Red: FeIII single element spectrum. Blue: continuum single element spectrum*

between weak line blends and strong single lines. As can be seen in the left hand side of the figure, $\tau_{5128\text{Å}\approx 1}$ at a velocity $\approx 9000\text{km.s}^{-1}$. The strong FeIII lines thus form at higher velocity than the weak line blends which form where the optical depth is maximal.

We can then picture the line formation process as the continuum opacity spectrum blending with the numerous FeIII weak lines, creating a first "layer" on top of which the strong FeIII lines form.

We display in the right hand side of Fig. 6.11 the FeIII single element spectrum scaled to the full PHOENIX spectrum integral. This is the second layer of what we call the "multi-layered line formation", the first one being the continuum "single element spectrum". We are very far from the photospheric picture, where line form by scattering light from an underlying black body. The canonical photospheric velocity in SYNOW is $\approx 13000\text{km.s}^{-1}$ for SNeIa around maximum light, which is 4000km.s^{-1} quicker than the velocity at which this layer forms.

We see from the ≈ 5100Å peak that some of the spectral features of this layer can make they way through to the final spectrum, while some other regions are completely dominated by other lines forming on top of it, as for example for $\lambda < 4000$Å.

FeII lines

On top of the FeIII layers we find a more complex region mainly dominated by FeII lines and single ionized silicon family elements. Other metals also contribute but their role in the

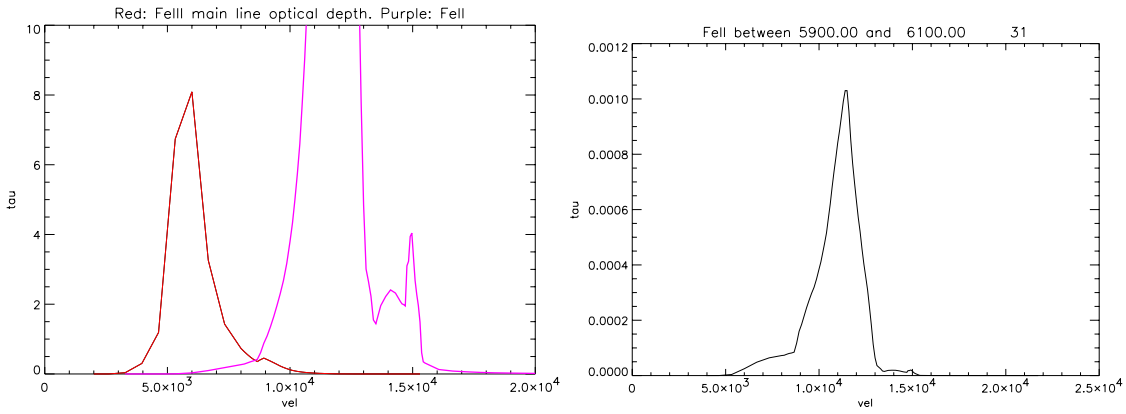

Figure 6.12: ***Left:*** *FeII 5170Å line optical depth.* ***Right:*** *Typical weak FeII line optical depth shape.*

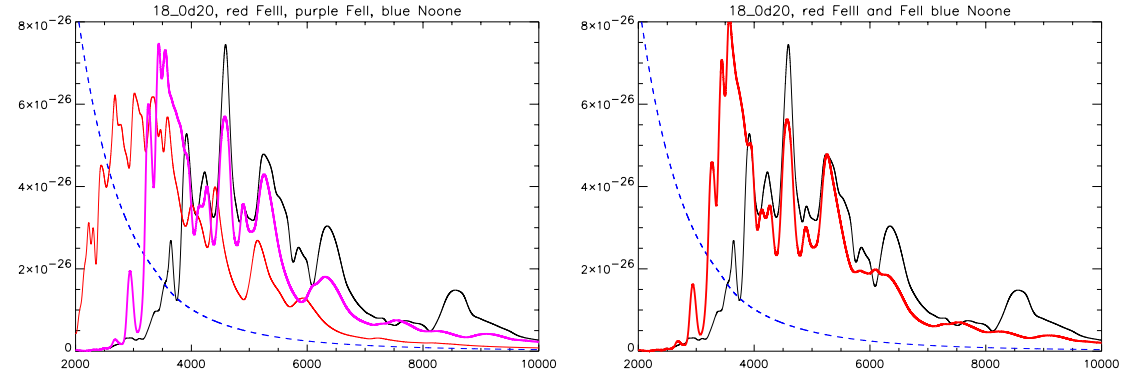

Figure 6.13: ***Left:*** *FeIII single element in red, FeII single element in pink, full spectrum in black and continuum single element spectrum in blue.* ***Right:*** *Full spectrum in black, continuum single element spectrum in blue, FeII and FeIII "single element" spectrum*

$\lambda > 5000$Å is of second order. We thus concentrated on FeII because of its large impact in this part of the spectrum.

We display in Fig. 6.12 the strong FeII 5170Å line optical depth as well as one of its weak lines on the right hand side of the same figure. The strong FeII lines form around 15000km.s^{-1}, where their optical depth approaches unity, whereas the weak line blend will have form around 11000km.s^{-1} where their optical depth peaks. We have again two layers of line formation. The weak line blends forms on top of the FeIII layers, whereas the strong lines form farther out.

Fig. 6.13 left hand side displays the FeII and FeIII single element spectra normalized to

the full PHOENIX spectrum integral. On the right hand side we show the FeII and FeIII "single element spectrum". It is calculated in the same way as a regular "single element spectrum" but keeping both FeII and FeIII lines. It is also normalized to the full spectrum integral. Concentrating on the 5300-6500Å wavelength region, we can relate this spectrum to the photospheric model.

Instead of a Planck function, we have what we could abusively call a "multi-layered pseudo-continuum" formed by continuum opacity, and by successive layers of FeIII and FeII lines. On top of it, strong lines like the 5170Å FeII one form.

From the left hand side figure we see that once we merge FeIII and FeII effects, FeII lines dominate the spectrum, completely reshaping the underlying FeIII "layer" that still has a fundamental role, as the right hand side is the *merging* of the two effects.

The "multi-layered line formation" picture is also more complex in that depending on the wavelength region, different depth of the supernovae envelope are seen. For example,in the 6000Å blend, we see the 11000km.s^{-1} region, whereas when looking at the 5170 or 4500Å wavelength zone we see the 15000km.s^{-1} region.

Silicon family elements lines

The silicon family elements lines form in the same layer than the 5170Å FeII line. This is close to the photospheric model with a much more complex "pseudo-continuum" than a Planck function. We use abusively the word "pseudo-continuum" in order to discriminate between the strong, well separated lines forming above 11000km.s^{-1} and the layers blending underneath, even though the resulting shape can be somewhat far from a "continuum".

We show in Fig. 6.14 the FeIII 5128Å(black), FeII 5170Å(red), SiII 6373Å(blue) and SII 5455Å(pink) lines optical depth. The strong SiII line responsible of the $\Re_{Si} \approx 6100$Å trough forms in the same 11000-15000km.s^{-1} region than the strong FeII line, i.e. the region. The SII line forms deeper, emphasizing the fact that the different layers defined are not as rigid as it could seem. They could be considered as part of the underlying "multi-layered pseudo-continuum" or of the lines forming atop as well. We made the choice to label them as part of the upper layer of the line formation because sulfur is part of the silicon family elements.

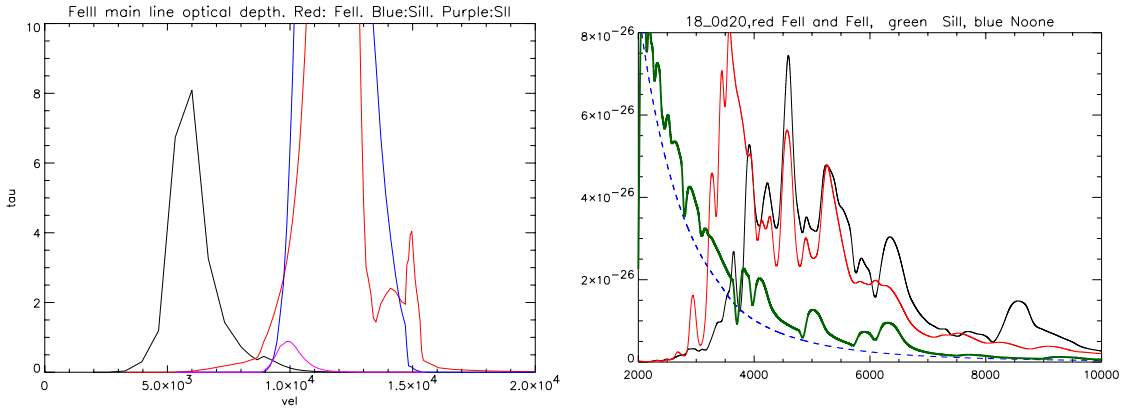

Figure 6.14: ***Left:*** *FeIII 5128Å(black), FeII 5170Å(red), SiII 6373Å(blue) and SII 5455Å(pink) lines optical depth.* ***Right:*** *Full spectrum in black, continuum single element spectrum in blue, FeII and FeIII "single element" spectrum in red, SiII single element in green.*

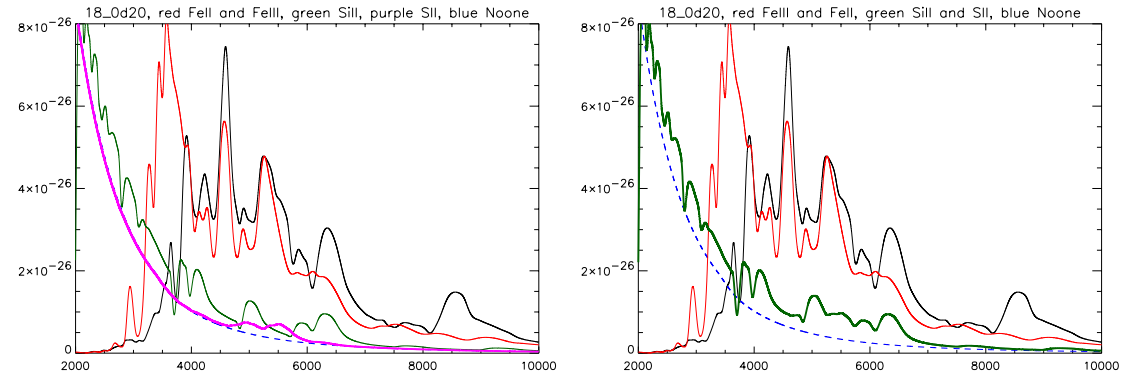

Figure 6.15: ***Left:*** *Black: complete spectrum. Blue continuum single element spectrum. Red FeIII & FeII "single element spectrum". Green: SiII "single element spectrum". Pink: SII "single element spectrum".* ***Right:*** *Black: complete spectrum. Blue continuum single element spectrum. Red FeIII & FeII single element spectrum. Green: SiII & SII single element spectrum.*

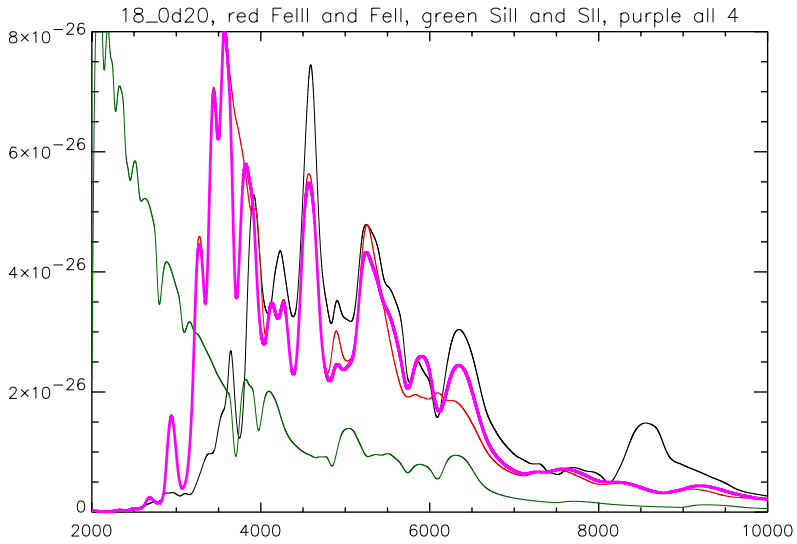

Figure 6.16: *Black: complete spectrum. Blue continuum single element spectrum. Red* FeIII *&* FeII *"single element spectrum". Green:* SiII *&* SII *"single element spectrum". Pink:* FeIII, FeII, SiII *&* SII *"single element spectrum".*

SiII lines: In the right hand side of the same figure we display the SiII single element spectrum which shows that the $\approx$ 6300 peak and the associated trough as well as the red wing of the $\approx$ 5600Å trough can be accounted for by SiII lines. These two features form on top of the almost flat "pseudo-continuum".

The SiII "single element spectrum" is compared to the continuum opacity spectrum in fig. 6.14 and shows that in between of the strong lines, the SiII lines have no effect. This strongly differs from iron behavior, and verifies better the separation condition of the Sobolev approximation, making SiII SYNOW simulation more accurate than the FeII one.

SII lines: We plot in the left hand side of Fig. 6.15 the SII "single element spectrum". Its only significant contribution is the blue wing of the $\approx$ 5600Å trough. The absence of the sulfur "W" is one of the main problem of the LTE PHOENIX simulated spectra with W7 model. Nevertheless, the right hand side of the same figure shows that for this simulated spectrum, the SiII & SII combined lines can account for the $\Re_{Si}$ wavelength region shape. The SII line blend dominates the blue wing of the $\approx$ 5600Å trough even if they form deeper than the strong FeII and SiII lines because there are no other strong lines on top of it.

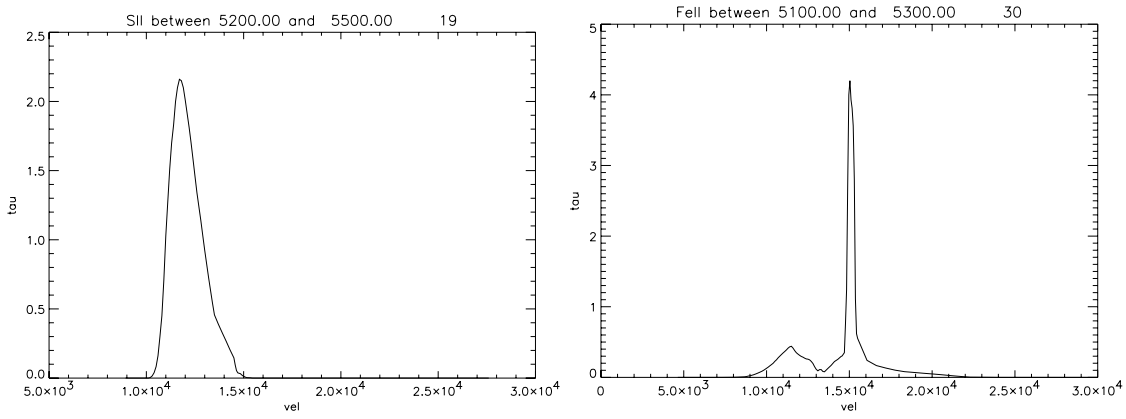

Figure 6.17: ***Left:*** *S*II 5455*Å optical depth.* ***Right:*** *Fe*II 5170*Å optical depth*

This also justifies our choice to identify SiI lines as part of the last layer of the spectrum formation. But the strong FeII 5170Å peak's red wing also strongly impacts on the $\Re_{Si}$ blue trough red wing formation, almost washing out the SiI contribution.

Fig. 6.16 shows the FeIII, FeII, SiII and SiI "single element spectrum" still normalized to the full spectrum integral. The $\Re_{Si}$ 5400-6400Å wavelength zone is well reproduced by these four species. The SiI sulfur line, even if it does not dominate the whole $\approx$ 5500Å peak, is fundamental in reproducing its shape, and dominates the red wing of this FeII 5170Å peak.

6.2.2 Evolution with luminosity, or why $\Re_{SiS}$ works

Higher luminosity PHOENIX spectrum

For a -19.17 blue magnitude PHOENIX spectrum with the same W7 model abundance set, FeII will ionize more into FeIII because of the global temperature increase. The FeII lines will therefore become weaker as the supernovæ luminosity increases, while SiI lines will remain, since SiI is harder to ionize. Moreover, its lines will even become stronger in LTE because of the higher temperature.

The optical depth of the FeII 5170Å and the SiI 5445Å lines are shown in Fig. 6.17. As expected, the sulfur line became stronger while the FeII line maximal optical depth decreases and now peaks in a thiner region only $\approx$ 200km.s^{-1} wide around 15000km.s^{-1}. The SiI 5170Å line now dominates the blue wing of the blue $\Re_{Si}$ trough.

Fig. 6.18 left hand side clearly shows that the FeII lines contribution in the $>$ 5500Å re-

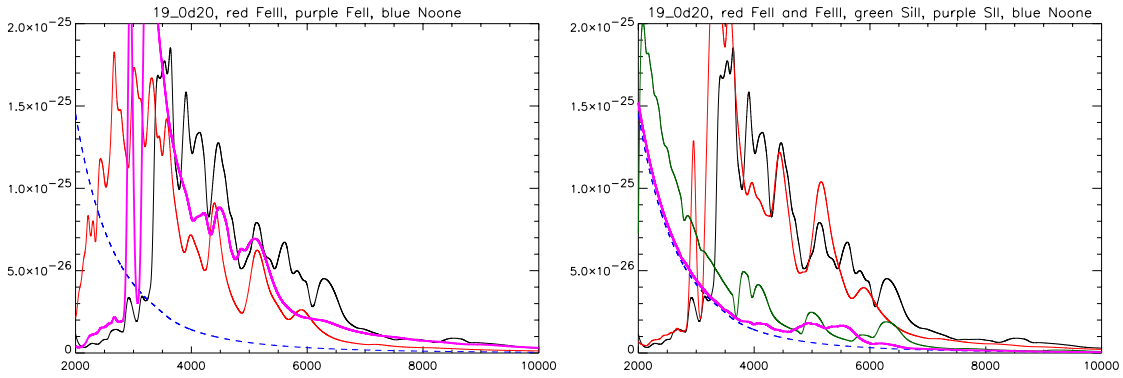

Figure 6.18: ***Left:*** *Black, complete spectrum. Blue, continuum single element spectrum. Red,* FeIII *single element spectrum. Pink,* FeII *single element spectrum.* ***Right:*** *Black, complete spectrum. Blue, continuum single element spectrum. Red,* FeIII *single element spectrum. Green,* SiII *single element spectrum. Pink,* SII *single element spectrum*

gion is now negligible, while the FeIII contribution remains qualitatively unchanged. The "multi-layered line formation" and the "multi-layered pseudo continuum" defined previously still hold here, but the element contributions changed as well as the velocities at which each layer forms.

On the right hand side of Fig. 6.18, the SiII lines that form on top of the FeIII dominated "multi-layered pseudo-continuum" stay strong, but their relative strength changed. The SII "single element spectrum" displayed on the same graph shows that SII lines will now be preponderant in the blue wing of the $\approx$ 5600Å trough.

Fig. 6.19 shows how these lines blend together in order to create the $\Re_{Si}$ wavelength region spectrum. The left hand side figure shows that FeII affects the FeIII dominated pseudo-continuum through line blending and flux transfer toward the red without changing too much its shape. This comes from its numerous blue lines that help to transfer flux toward the red as the light flows out of the supernova. On the other hand, the strong FeII lines are now forming in a much narrower velocity region at $\approx$ 15000km.s^{-1}, and are thus less extended in wavelength too.

The green line shows SiII and SII blend that reproduces well the $\Re_{Si} \approx$ 5600-6300Å shape. The main discrepancy stands in the intermediate $\approx$ 5800Å peak, where the FeIII has its emission like feature. It is hard to tell whether or not it is a true emission since this region is not dominated by a single line but is created by the complex blend of more than 100 FeIII

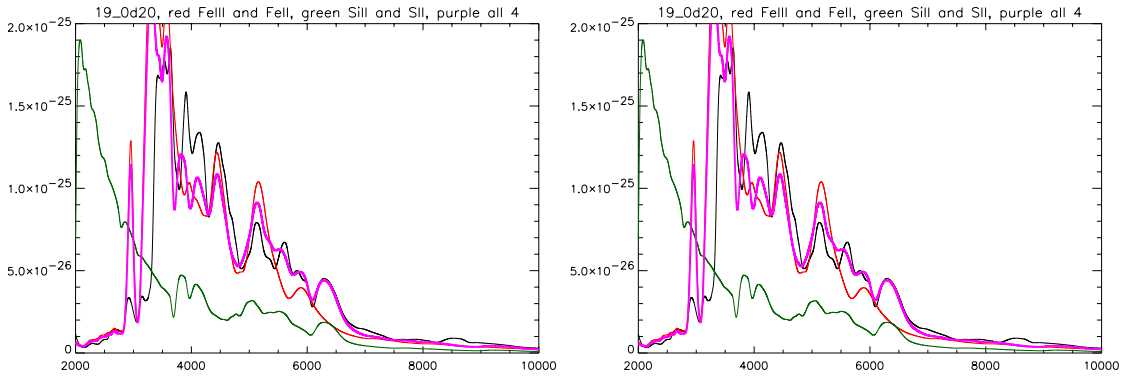

Figure 6.19: ***Left:*** *Black, complete spectrum. Blue, continuum single element spectrum. Red,* FeIII *&* FeII *single element spectrum. Green,* SiII *&* SII *single element spectrum.* ***Right:*** *Black, complete spectrum. Pink,* FeIII*,* FeII*,* SiII *and* SII *single element spectrum. Thick line scaled by an 0.8 multiplicative factor.*

lines.

The right hand side of the same figure shows the FeIII, FeII, SiII and SII "single element spectrum". Like all of the "single element spectra" displayed in this section, we normalized it to the full spectrum total flux. We see that these four elements alone reproduce almost perfectly the $\Re_{Si}$ wavelength zone.

The "multi-layered line formation" picture shows that the depth of the troughs are not the pertinent quantities, since the "absorption" feature are formed by a complex blend of absorptions and emissions. The intermediate ≈ 5900Å $\Re_{Si}$ peak is clearly the more complex feature in this wavelength region, mixing FeIII, FeII and SiII effects. The way $\Re_{Si}$ is calculated couples these three elements plus the SII behavior, making it difficult to understand its correlation with luminosity.

Since above 6000Å the $\Re_{Si}$ region is dominated by SiII lines, while the 5400Å zone is dominated by SII lines, the $\Re_{SiS}$ ratio definition isolates the main contributors to the $\Re_{Si}$ correlation with luminosity, the FeIII dominated layer behaving like a "pseudo-continuum" on top of which these preponderant features form.

As the FeII lines become stronger as the luminosity decreases, its 5170Å emission peak impact on the $\Re_{SiS}$ ratio will also increase. $\Re_{SiS}$ correlation with luminosity is thus expected to change trend for the faint supernovæ, the break point luminosity still having to be found. We shall address this issue again in next chapter, as well as the comparison of the PHOENIX

spectra with reality. We shall then show that the "multi-layered spectrum formation" picture is not only a theoretical construct, but also exists in reality.

Finally, even if it is difficult to compare two different elements lines that form at different places of the supernova, we can propose at least a partial explanation for the $\Re_{SiS}$ correlation with luminosity. In the pure LTE case, the source function of the SiII and SII lines would be Planck functions, and their ratio as the temperature increases would go the wrong way. But PHOENIX does not assume pure LTE. In this situation, the source function can be approximated by a resonant scattering source function (the assumption used in SYNOW) and hence it is proportional to the "dilution factor" corresponding to the "pseudo-photosphere".

The dilution factor W (Mihalas, 1978) is:

$$W = (1 - \sqrt{(}1 - (R_0/R)^2)) \tag{6.3}$$

where R_0 is the radius of the photosphere, and R the radius at which the scatterer is found. It describes the evolution of the solid angle of the photosphere seen by a scatterer at R with radius.

In the PHOENIX models we calculated, R_{SiII}, i.e. the radius at which $\tau_{SiII} \approx 1$ is approximately constant for $-19.0 < M_B < -18.2$ and corresponds to a velocity $v_{SiII} \approx$ 15000km.s^{-1} when the velocity at which the SII line peaks varies from $\approx$ 10000km.s^{-1} for $M_B = -18.2$ to $\approx$ 12000km.s^{-1} for $M_B = -19.0$.

The ratio of the source functions $S_{SII}/S_{SiII} \propto W_{SII}/W_{SiII}$ consequently increases from $M_B = -19.0$ to $M_B = -18.2$ as the $\Re_{SiS}$ ratio requires. This behavior is maintained for 1000km.s^{-1} difference for v_{SII} and a 1000km.s^{-1} decrease in v_{SiII} between $M_B = -19.0$ and -18.2.

Detailed NLTE studies will be required to prove that this effect dominates $\Re_{SiS}$ behavior and to test other more complex radiative transfer effects, but this interpretation is compatible with all observations at present.

Chapter 7

Comparison with reality

In this chapter we will compare real supernovæ to our PHOENIX synthetic spectra. We will compare the spectra as well as the $\Re_{Si}$, $\Re_{Ca}$ and $\Re_{SiS}$ ratio, using our new understanding of the spectrum formation to constrain W7 explosion model.

7.1 $\Re_{Si}$ & $\Re_{SiS}$ comparison with reality

7.1.1 $\Re_{Si}$ & $\Re_{SiS}$ in PHOENIX VS real supernovæ

In Fig. 7.1 we display $\Re_{Si}$ and $\Re_{SiS}$ calculated on synthetic spectra simulated for W7 model 20 days after explosion. We kept the same W7 model throughout the whole luminosity sequence even though it is doubtful that the nickel mass would remain the same for such a wide luminosity range. On the other hand, considering the complexity of the radiative transfer problem in type Ia supernovæ atmospheres, changing only one parameter at a time was mandatory. One has to keep in mind that the supernova composition *must* change along the luminosity sequence.

In the left hand side of Fig. 7.1, the black crosses correspond to the synthetic spectra and the green squares the real supernovæ $\Re_{Si}$. These two correlations with luminosity, if they both exist, are clearly different.

The synthetic spectra display three phases in the evolution with luminosity. First they start with an $\Re_{Si} \approx 0$, which corresponds to the spectra for which the blue $\Re_{Si}$ trough is negligible. Then comes a linearly increasing $\Re_{Si}$ zone as the blue magnitude decreases.

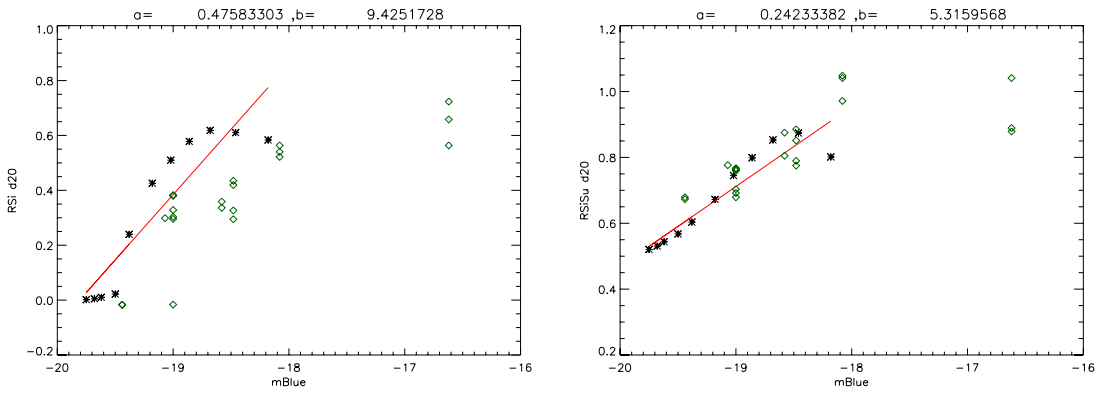

Figure 7.1: ***Left:*** $\Re_{Si}$ *for our* PHOENIX *d20 synthetic spectra. Green: real supernovæ* $\Re_{Si}$. ***Right:*** *idem for* $\Re_{SiS}$. *The red line is the linear regression done on the* PHOENIX *points.*

Finally $\Re_{Si}$ decreases again.

We lack points to sample the evolution of real supernovæ correctly, but the 91T spectrum is clearly in the $\Re_{Si} \approx 0$ region. The linear increase region also exists for real supernovæ, but with a smaller slope than in the PHOENIX simulated spectra. It is hard to decide with 91bg alone if the declining $\Re_{Si}$ region also exists for real supernovæ. This peculiar event is much fainter than the "Branch Normal" supernovæ, and that the nucleosynthesis is unlikely to be the same. It's integration in such a loosely sampled sequence is therefore difficult.

In the right hand side of Fig. 7.1, we display the $\Re_{SiS}$ sequence for both the synthetic spectra simulated with W7 model 20 days after explosion and the real supernovæ. The "Branch Normal" luminosity supernovæ are in good agreement within the real supernovæ dispersion.

However, for the -18.0 bolometric magnitude synthetic spectrum, $\Re_{SiS}$ is not only in disagreement with reality, but it also falls out of the linear regression trend, while the fainter SN 1986G is still in agreement with the linear regression slope. We showed in the previous chapter that the central ≈ 5900Å peak of the $\Re_{Si}$ wavelength region was dominated by FeII and FeIII lines, while $\Re_{SiS}$ was the ratio of SiII and SII dominated features. We also showed that at the contribution of FeII lines on the ≈ 5700Å $\Re_{Si}$ peak increased as the luminosity decreased.

The main difference between $\Re_{Si}$ and $\Re_{SiS}$ comes from the iron lines, which have been

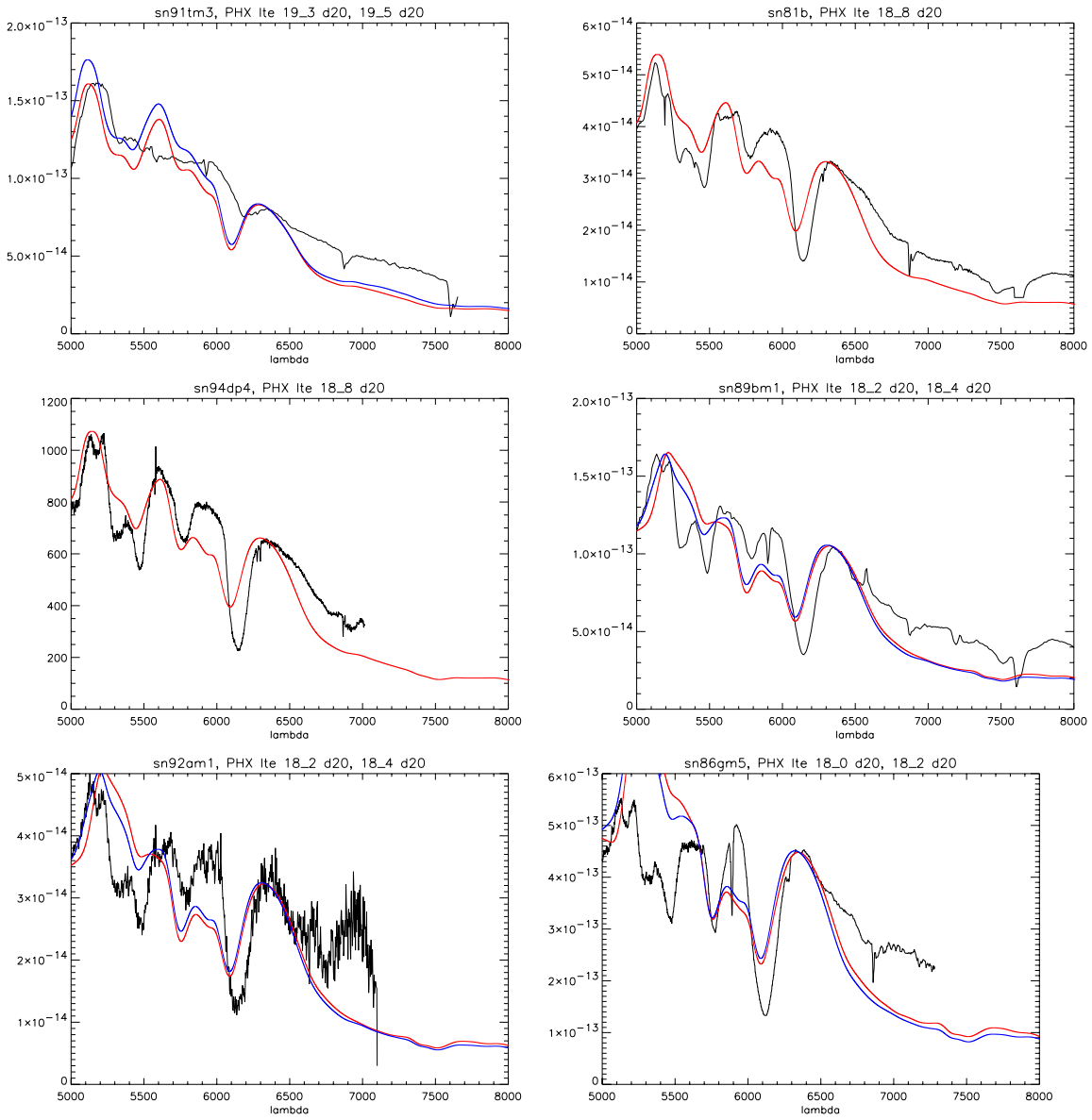

Figure 7.2: $\Re_{Si}$ *zone, black real spectra. From top left to bottom right: 91T, 81b, 94d, 89b, 92a, 86g. The* PHOENIX *spectra with the closer blue magnitude have been chosen.*

excluded from $\Re_{SiS}$ for bolometric magnitudes higher than $M_{Bol} > -18.2$. The discrepancy between $\Re_{SiS}$ calculated on the real supernovæ spectra and on the luminosity sequence spectra for 20 days after explosion happen when these FeII lines become preponderant at lower luminosities.

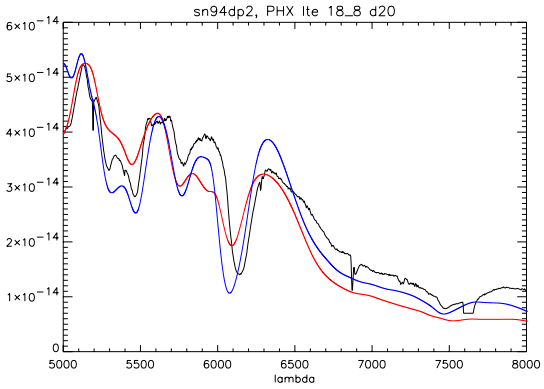

Figure 7.3: $\Re_{Si}$ *zone, black 94d spectrum. Red W7 model, blue P.Höflich model*

We display in Fig. 7.2 the $\Re_{Si}$ wavelength region for the real supernovæ and for the synthetic spectra sequence at day 20 after explosion. We plot for each real supernova the two simulated spectra with the closer $\Re_{SiS}$, normalized to have the same 6400Å flux. The $\approx$ 6100Å trough is in all the cases poorly reproduced, being too wide and its minimum being too blue, besides from the sn86g 5 days prior to maximum light spectrum where the trough is too shallow but of the right width.

The $\approx$ 5900Å peak is too small in each case, while the $\approx$ 5100, 5600 and 6300Å peaks are in good agreement with reality. We showed these three emission features to be dominated by lines forming in the outermost layer of the "multi-layered" line formation process, i.e. at $\approx 11000 - 15000$km.s^{-1}. Moreover, they are dominated by one single element, accordingly FeII, SII and SiII. On the contrary, absorption features are blends of true absorption and emission. Their blue edge is usually dominated by the next emission peak. The wide $\approx$ 6100Å trough shows that the $\approx$ 5900Å peak is not as large as in real spectra.

This feature has been shown to be formed at the FeIII and FeII weak lines layers interface at $\approx$ 10000km.s^{-1}. While the $\approx$ 5100Å emission peak is dominated by optically thick FeII lines, and is thus less sensitive to the deeper abundance structure, the $\approx$ 5900Å one being formed of weaker line is more sensitive, proving W7 model weakness for layers deeper than 11000km.s^{-1}.

If we compare Fig. 7.2 to Fig. 7.3, where we display for sn94d the W7 LTE best fit, as well as P.Höflich "pah_5p0282216" model for day 20 after explosion also calculated in

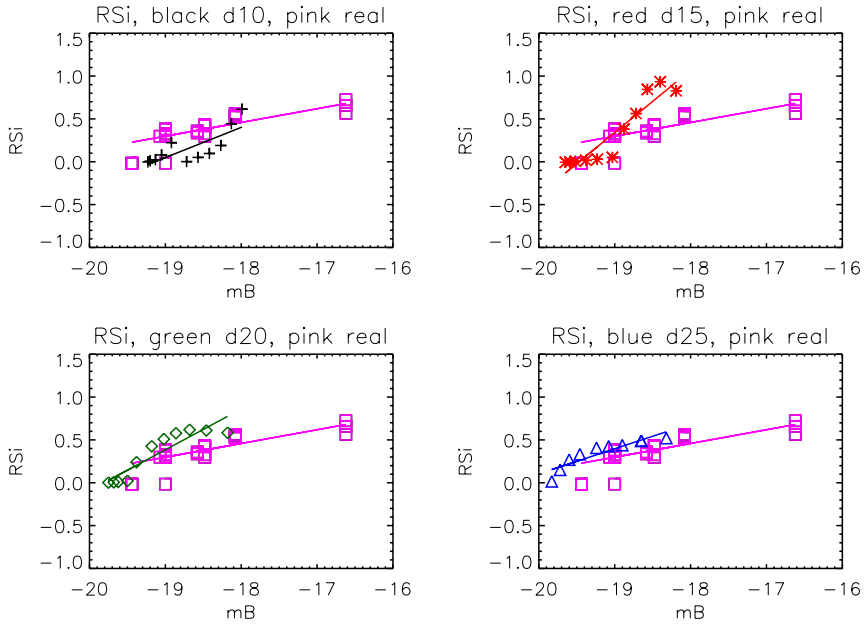

Figure 7.4: $\Re_{Si}$ *time dependence. Pink squares: real supernovæ. Black: day 10 after explosion. Red: day 15 after explosion. Green: day 20 after explosion. Blue: day 25 after explosion.*

LTE, we note the later model better agreement of the ≈ 5900Å peak. The ≈ 6300Å one is not as well reproduced than with W7 model, and the too deep ≈ 6100Å feature shows that this is likely due to an over estimation of SiII in the $11000 - 15000$km.s^{-1} region. We also see that the characteristic "W" sulfur feature is better reproduced by P.Höflich model, showing that its persistent absence from W7 model spectra does come from an abundance structure problem. Moreover, this feature has been reproduced with homogeneous W7 model in Nugent et al. (1997). Homogeneous models in PHOENIX have shallower density structure, as the P.Höflich one. Since the SiII lines form right on top of the thick blended iron lines layer, they are a good indicator of the model global density structure quality, and they suggest that the new models must have smoother densities profiles than W7. As the density is mainly dominated by iron, this clue, in complete agreement with (Baron et al 2005 in preparation) can help to constrain explosion models.

7.1.2 Time dependence

In Fig. 7.4 we display the $\Re_{Si}$ and $\Re_{SiS}$ evolutions with luminosity for each one of the synthetic spectra epochs. The pink squares stand for the real spectra $\Re_{Si}$ and $\Re_{SiS}$.

Fig. 7.5 displays day 10 after explosion spectra $\Re_{Si}$ wavelength region. At blue mag-

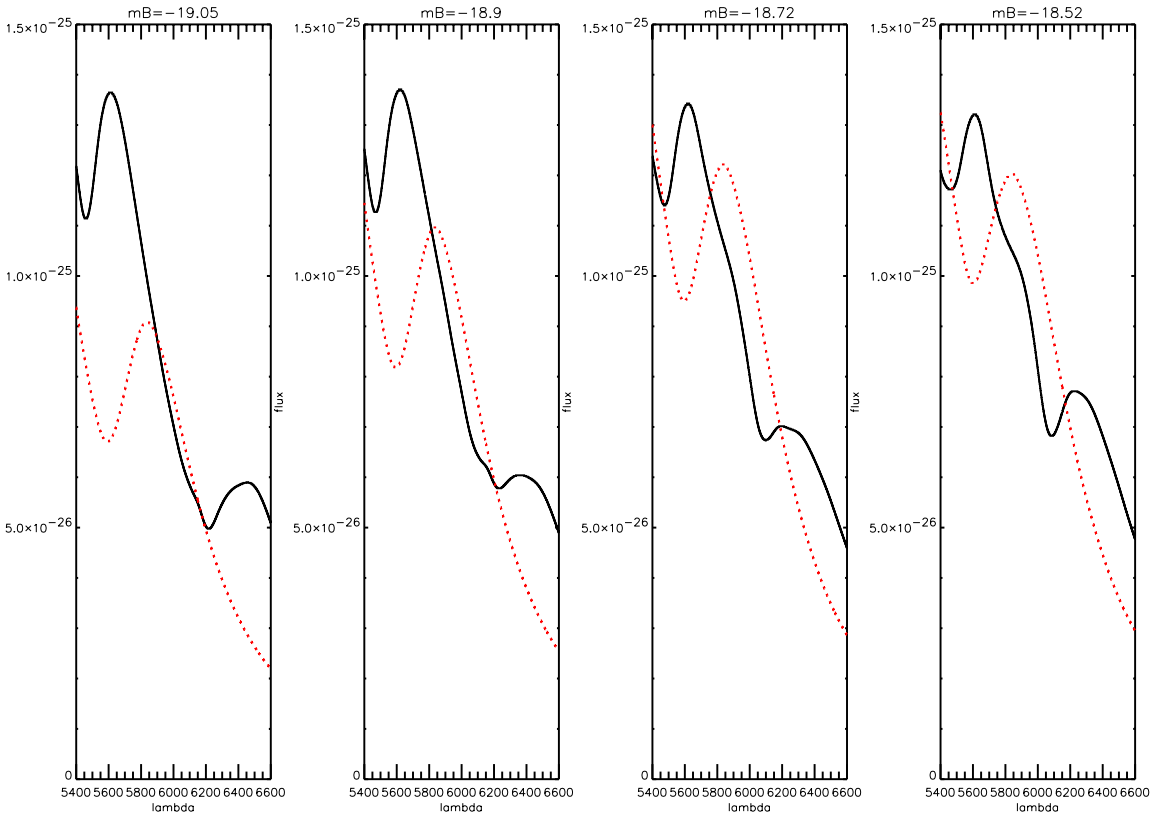

Figure 7.5: $\Re_{Si}$ *zone evolution with luminosity, day* 10 *after explosion. The black curve are the full synthetic spectra, the red curve are only* FeIII *single element spectra.*

nitudes $M_B > -18.9$ we note a complete lack of SiII lines in the spectra. The left hand side of the figure shows that the $\Re_{Si}$ region at this epoch is dominated by FeIII lines for $M_B = -19.05$. Then, as the luminosity decreases, the ≈ 6200Å peak is replaced by the 6355 Å SiII P-Cygni absorption profile.

At day 10 after explosion the supernova is hotter than at day 20. Iron is thus ionized into FeIII further out, pushing its line formation layer forward and shielding the SiII lines forming at $\approx 11000 - 15000 \mathrm{km.s}^{-1}$. As the luminosity decreases the temperature drops letting FeIII to recombine into FeII which as was previously shown has a lower impact on the $\approx 5800 - 6400$Å region. When this happens, the SiII lines contribution to the spectrum quickly rises, explaining the break between the $\Re_{Si}$ FeIII and the $\Re_{Si}$ SiII/SII dominated evolutions.

At day 15 after explosion, the supernova is cold enough to have the FeIII line formation

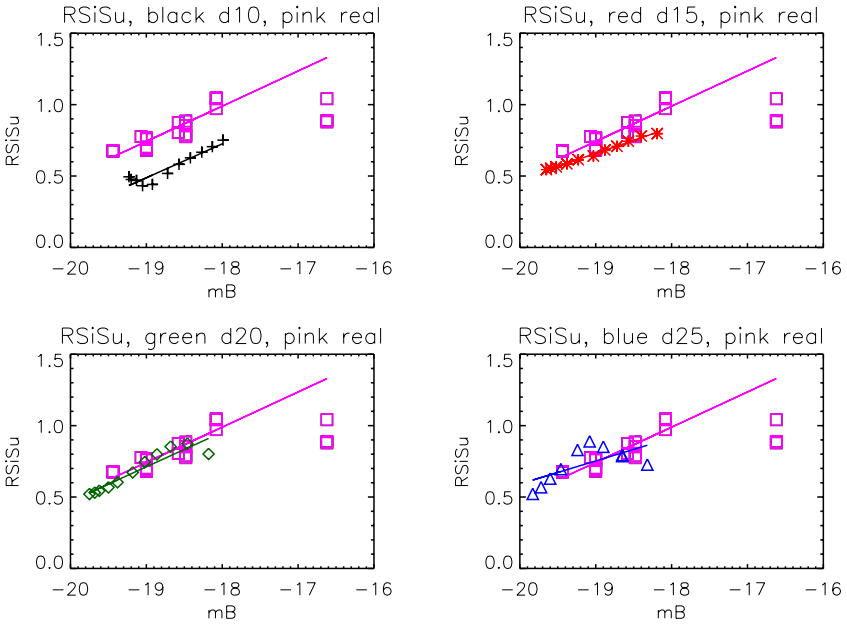

Figure 7.6: $\Re_{SiS}$ *time dependence. Pink squares: real supernovæ. Black: day 10 after explosion. Red: day 15 after explosion. Green: day 20 after explosion. Blue: day 25 after explosion.*

layer deeper than the SiII one. As time increases the density drops due to expansion. This causes luminosity variation to have less effect on the $\Re_{Si}$ evolution. The trend of the day 15, 20 and 25 after explosion are thus alike, but the slope is smaller for the later epochs. The $\Re_{Si}$ evolution closest to the real supernovæ is found for day 25 after explosion. Since the $\Re_{Si}$ evolution is strongly impacted by the intermediate ≈ 5900Å iron dominated peak, and since it forms in a region where the iron density decrease is slower than for earlier epochs, this again points toward a shallower iron density profile than what is predicted by the W7 model.

In Fig. 7.6 we display the $\Re_{SiS}$ correlation with luminosity for each of the synthetic spectra epochs we simulated. The best agreement with real supernovæ is found for day 20 after explosion. This happens to be in agreement with peak luminosity which usually occurs at the same date in the SNIA rest frame. Since $\Re_{SiS}$ is in complete agreement with reality for day 20 after explosion while $\Re_{Si}$ fails, the main problem of W7 model is likely to originate in the deeper iron layers rather than in the silicon family. At day 25 after explosion, the tendency of $\Re_{SiS}$ to decrease for blue magnitudes higher than $M_B = -18.4$ is confirmed. The $\Re_{SiS}$ trend reversal occurs at lower luminosity for day 25 after explosion. The supernova in then colder than at day 20 for the same luminosity, so that FeII lines

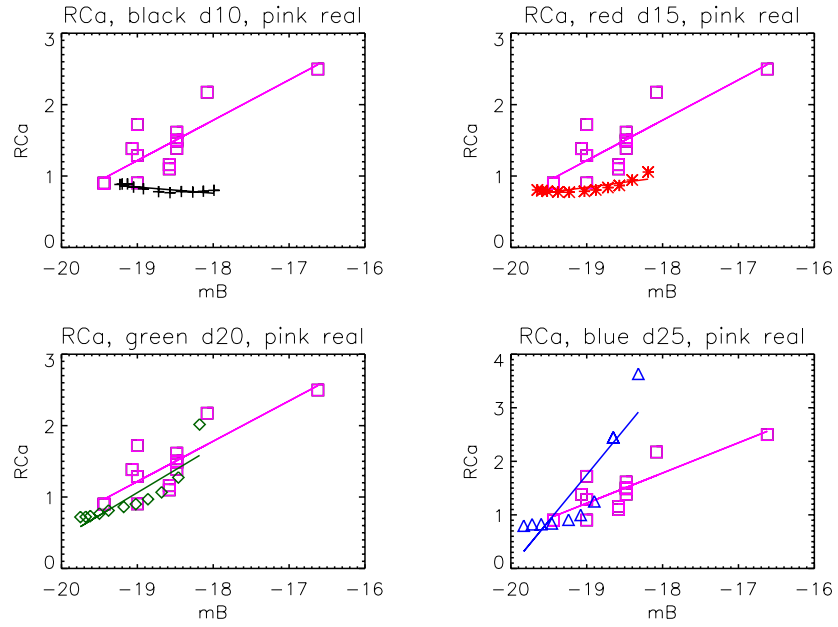

Figure 7.7: $\Re_{Ca}$ *time dependence. Pink squares: real supernovæ. Black: day 10 after explosion. Red: day 15 after explosion. Green: day 20 after explosion. Blue: day 25 after explosion.*

become preponderant for smaller blue magnitudes.

The supernova SN 1991bg seems to be following this trend, but the breakdown of the correlation occurs at lower luminosities for the real supernovæ, showing that the W7 model more accurately describes "Branch Normal" supernovæ. Even though the nucleosynthesis can not be the same for the faint SNeIa, their light curve evolution show their maximum light to occur earlier than average, in agreement with the trend of the synthetic spectra.

7.2 $\Re_{Ca}$ comparison with reality

We display in Fig. 7.7 $\Re_{Ca}$ correlation with luminosity for each epoch of the sequence as well as for real supernovæ. The agreement at day 20 after explosion is well within the observational dispersion. For simulated supernovæ the $\Re_{Ca}$ correlation with luminosity is not than linear, the later the epoch the steeper the $\Re_{Ca}$ increase with increasing blue magnitude.

As for $\Re_{SiS}$, days 20 after explosion is in agreement with the maximum light time for real supernovæ. And again SN 1991B falls out of the trend for this date, since extrapolation of day 20 after explosion trend would give a much larger $\Re_{Ca}$. On the other hand, the extrapolation of day 10 after explosion trend would give a coherent value. The adiabatic expansion

effect on these ratio is clearly proven, as well as their value as luminosity indicators.

The explanation of the quality of $\Re_{Ca}$ agreement with reality relies on the same physical property than $\Re_{SiS}$: even if it is very doubtful that the nucleosynthesis remain unchanged over the whole luminosity sequence, and the emission peaks are less sensitive to abundance changes than the absorption trough, these ratio are mainly driven by temperature changes.

Chapter 8

Prelude to NLTE studies

8.1 LTE vs NLTE

In the previous chapters, the discussion was based on LTE calculations. We will now present W7 converged models in LTE and NLTE for day 20 after explosion and of approximately the same blue magnitude[1]. The purpose is to compare both complete and "single element" spectra in order to study the LTE approximation and thus test the reliability of the "multi-layered" spectrum formation in the NLTE case. The magnitudes of these spectra are listed in table tab. 8.1, the NLTE spectrum is bluer than the LTE one for a comparable blue magnitude.

In fig. 8.1 we plot the LTE spectrum in black and the NLTE one in red. The left hand side displays the F_λ spectrum, showing a qualitative similarity below 4500Å. The right hand

[1]The blue magnitude was chosen, as it is the chosen parameter to compare to observed spectra. The next step would be to compare the magnitudes and spectra of LTE and NLTE spectra of the same bolometric luminosity in order to study the difference in the energy transfer between.

Table 8.1: *LTE and NLTE magnitudes of the studied spectra*

	LTE	NLTE
U	-20.1	-20.0
B	-19.4	-19.3
V	-19.5	-19.2
R	-19.3	-18.9
I	-18.7	-18.3

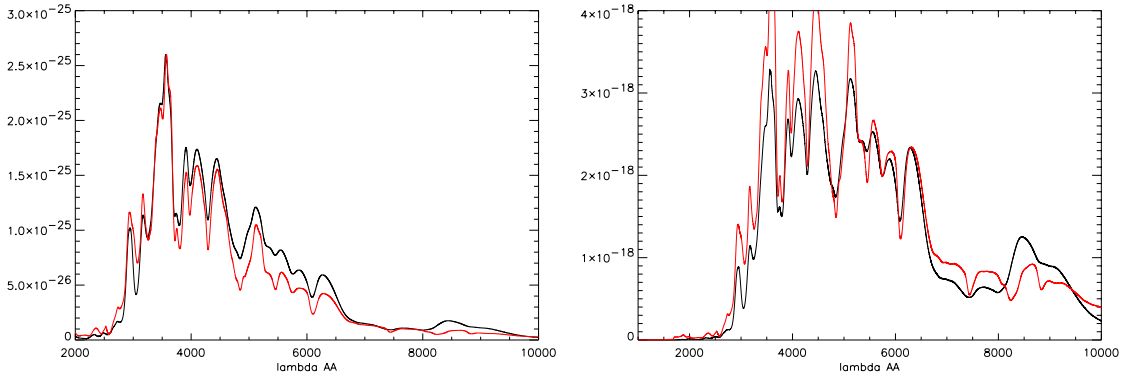

Figure 8.1: ***Left:*** *W7 model LTE (black) VS NLTE (red) calculation* ***Right:*** *idem but in F_ν scaled to both have the same 6300Å value.*

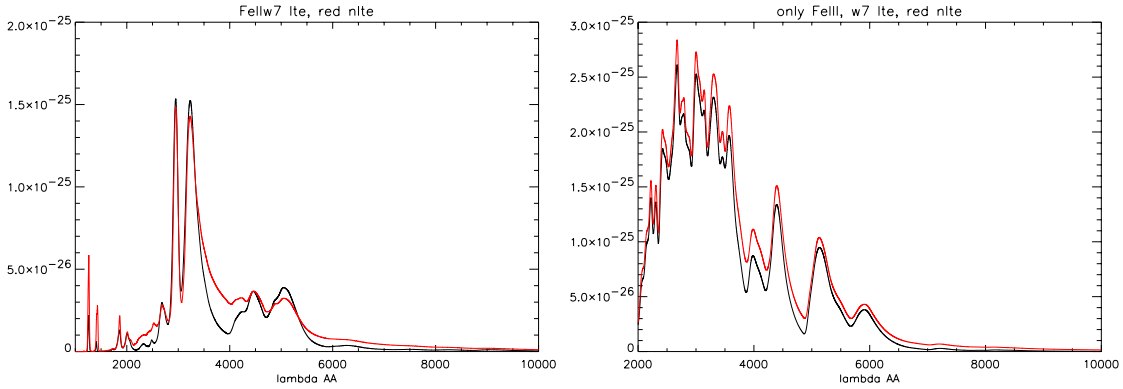

Figure 8.2: *LTE(black) vs NLTE(red)* ***Left: FeII single element spectrum, scaled to have the same 3000Å flux Right:FeIII single element spectrum***

side plot displays the F_ν spectrum[2], which emphasizes the long wavelength and eases the comparison. The F_ν spectrum are rescaled to have the same 6300Å flux, and show the similarity of the spectral features also in the $5000 - 7000$Å wavelength zone, even if the flux is larger in the LTE case. The NLTE and LTE spectra differ more in the flux repartition (i.e. the colors) than in the local feature shapes, i.e. the optical depth and source functions, even though this difference is as expected for SNeIa near maximum light, small.

Fig. 8.2 displays FeII and FeIII "single element" spectra. The FeIII spectrum, formed deep inside of the supernova where the collisional rates are predominant is as expected

[2]The energy per surface per unit of frequency. Since $F_\nu \propto F_\lambda * \lambda^2$, the decrease of the "pseudo-continuum" in the red is compensated, and the relative importance of the features are more comparable than with F_λ throughout the whole spectrum.

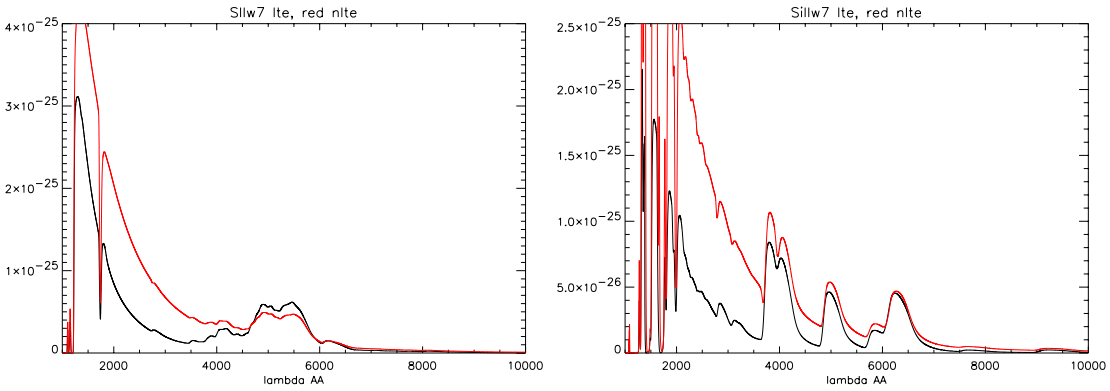

Figure 8.3: *LTE(black) vs NLTE(red)* ***Left:*** *SII single element spectrum* ***Right:*** *SiII single element spectrum Both scaled to have the same* $6200\,\mathring{A}$ *spectrum.*

much similar to the LTE spectrum. The "pseudo photosphere" defined previously is thus conserved in NLTE. The discrepancies between LTE and NLTE are also minor for FeII. This was to be expected[3]: the lower levels of the optical transitions of FeII are separated from the ground level by forbidden lines. The resulting energy gap is too wide for these levels population to be dominated by radiative rates. As the collisional rates prevail, FeII and FeIII thus appear to be coherently simulated in the LTE approximation used in PHOENIX.

Fig. 8.7 compares the SiII and SII "single element" spectra. They are qualitatively similar but for SiII below 2500Å. The NLTE effects are *qualitatively* negligible for these independent elements even though the small differences will affect the fine spectral studies such as line ratios.

8.2 NLTE line formation

In order to investigate whether the line formation procedure described previously holds in NLTE, we calculated several "single element" spectra on a W7 model converged for day 22 after maximum light in NLTE.

Fig. 8.4 left hand side displays the FeII and FeIII single element spectra: the FeIII dominated "pseudo-photosphere" also exists in NLTE.

The right hand side of the figure displays SiII and SII single element spectra. The

[3]Thanks David!

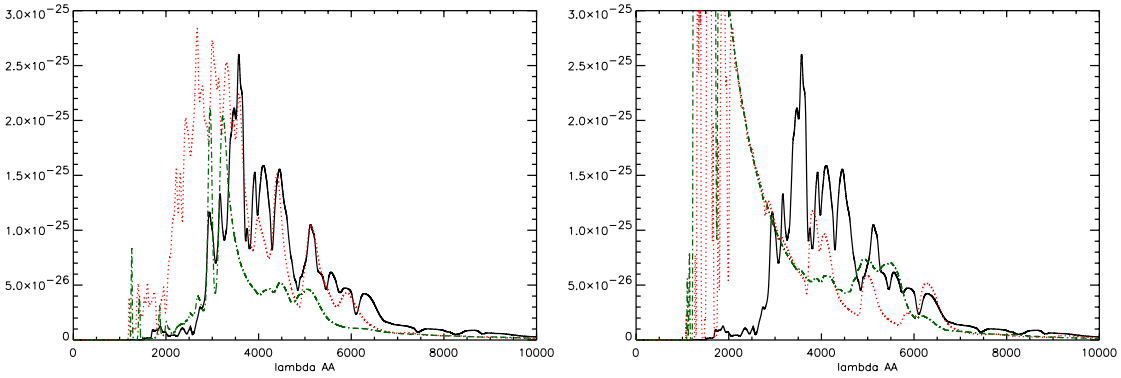

Figure 8.4: *NLTE,* ***Left:*** *FeII (green) & FeIII (red) single element spectrum* ***Right:*** *SiII (red) & SII (green) single element spectrum*

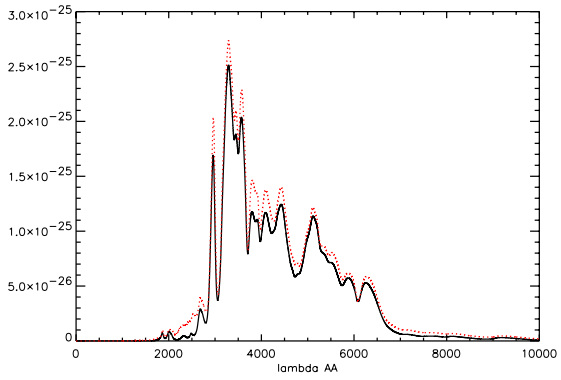

Figure 8.5: *LTE vs NLTE(red), FeII, FeIII, SiII & SII single element spectrum*

lines forming atop of the "pseudo-photosphere" dominate the $\approx$ 5700Å peak for SII and the $\approx$ 6200Å one for SiII as in the LTE case. The blue edge of the $\approx$ 5800Å trough of the $\Re_{Si}$ feature is *not* a P-Cygni profile but rather generated by a SII emission feature. In the same way the $\approx$ 6100Å trough is not a pure P-Cygni profile but a blend between the 6355 Å P-Cygni and the FeIII underlying emission.

The line forming process described in chapter 6 thus holds in NLTE. The quality of the LTE approximation in the $\Re_{Si}$ wavelength region and for FeIII, FeII, SiII & SII is stressed out in fig. 8.7 where the corresponding "single element" spectra in LTE and NLTE are displayed together. The main discrepancy between LTE an NLTE lies again mostly between 3500Å and 5500Åwhere the FeIII "pseudo-continuum" differs the most.

In the "multi-layered" line formation process, fig. 8.7 displays the SiII & SII "single element" spectrum, where the $\Re_{Si}$ wavelength region is shown to be dominated, in the

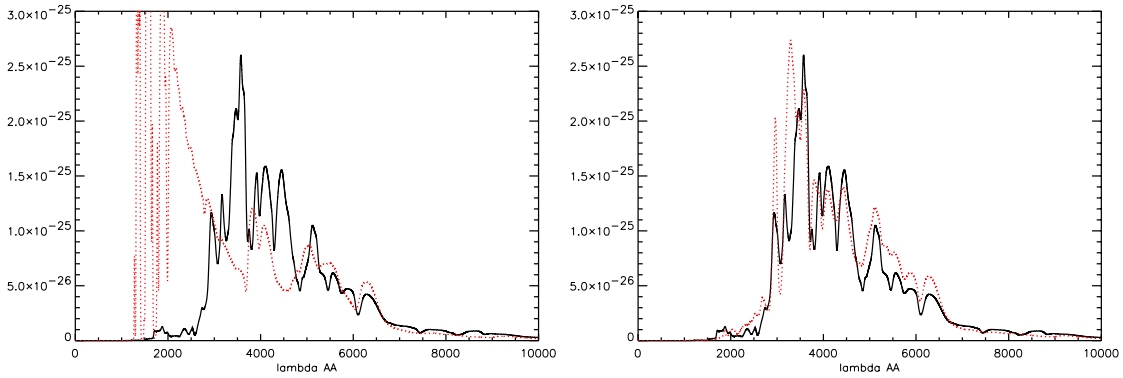

Figure 8.6: ***Left:*** *NLTE full spectrum(black), SiII & SIIsingle element spectrum(red)* **Right:** NLTE full spectrum(black), FeII, FeIII, SiII & SIIsingle element spectrum(red)

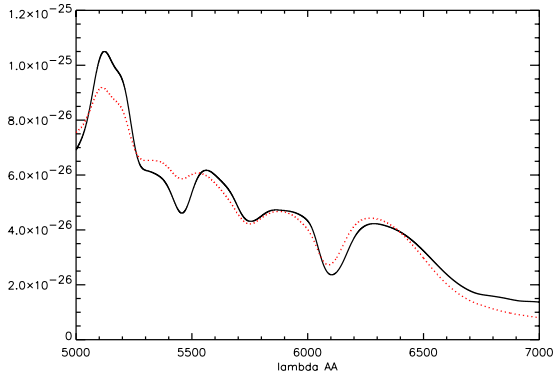

Figure 8.7: *NLTE full spectrum(black), FeII, FeIII, SiII & SIIsingle element spectrum(red), calibrated to have the same integral between* $5000\mathring{A}$ *and* $6500\mathring{A}$

$\approx$ 5700Åpeak by SII and in the $\approx$ 6200Åone by SiII. Also, the contribution of SII alone is not able to reproduce the $\approx$ 5300Å trough of the"sulfur W".

The right hand side of the figure shows the combination of FeIII, FeII, SiII & SII. As can be seen in the zoom displayed in fig. 8.7, the $\Re_{Si}$ wavelength region is qualitatively reproduced, as in the LTE case. Moreover, the "sulfur W" also appears more similar, proving the "multi-layered" process not to be reduced only to the $\Re_{Si}$ wavelength region.

This chapter was the first step on the NLTE studies, and proved that for individual elements, and especially iron, the LTE approximation including scattering for "Branch normal" blue magnitudes is close to the NLTE results. The "multi-layered" line formation process and the FeIII dominated "pseudo-photosphere" also proved not to be LTE artifacts. But detailed level populations studies will be needed to understand quantitatively the global discrepancies between the LTE and NLTE.

Conclusion

In this work we have studied the spectrum formation of SNeIa using the radiative transfer code PHOENIX to devise a grid of simulated spectra at different epochs and luminosity for the abundance structure of the W7 model.

We have used the self consistent physical structure of the supernova converged for each point of this grid and the "single element spectra" to study the line formation process, concentrating to the $5000 - 6500$Å wavelength region where the $\Re_{Si}$ line ratio is calculated. We have shown the spectrum formation of SNeIa to be a multi-layered process. The deeper layer is dominated for the dates studied by iron line blends which generate the overall shape of the spectrum. The outer silicon family elements layer on top of it then affects the spectrum through their strong lines as in the "photospheric" model, but with an underlying spectrum very different from a Planck function.

This new picture of the spectrum formation process, and the determination of the elements responsible of the $\Re_{Si}$ correlation with luminosity allowed us to derive a new line ratio we called $\Re_{SiS}$. It proved to be a blue magnitude indicator allowing luminosity measures with $\approx 15\%$ accuracy or better.

We simulated its use as well as the other spectral indicators $\Re_{Si}$ and $\Re_{Ca}$ in the SNAP/JDEM context and showed that they would allow us to monitor independently the mean luminosity of the SNeIa with a precision of $\approx 2\%$ to a redshift of $z = 1.5$ for $\Re_{SiS}$ and of of $\approx 9\%$ for $\Re_{Ca}$. Even if $\Re_{Ca}$ is less accurate than $\Re_{SiS}$, it is measurable for redshifts up to the $z = 1.7$ of SNAP/JDEM, since it is calculated in the 4000Å region of the spectrum. These two determinations of the SNeIa blue magnitudes will thus be a way to test evolution effects of the supernovæ independently of the light curve method.

We finally compared the BVRI colors calculated on the spectra of the simulated grid to

the Calan Tololo survey supernovæ ones at blue maximum light time. It allowed us to show that, since the overall shape of the spectrum is created by the iron line blends deep inside of the supernova, colors are weakly sensitive to the details of the abundance structure[4]. Also, comparing W7 to P.Höflich explosion models showed that the lack of flux in the I band pointed toward an underestimated flux transfer from the UV which could be accounted for by a shallower density profile.

[4]Even if, to the accuracy level needed to do accurate cosmology, the flux transfer due to lines is far from negligible

Bibliography

Arnett D., 2001, in Supernovae and Gamma-Ray Bursts: the Greatest Explosions since the Big Bang, pp. 250–257

Arnett W. D., 1982, ApJ, 253, 785

Baron E., Hauschildt P. H., Mezzacappa A., 1996, MNRAS, 278, 763

Cappellari M., Copin Y., 2003, MNRAS, 342, 345

Colgate S., White R., 1966, ApJ, 143, 626

Filippenko A. V., Riess A. G., 1998, pr, 307, 31

Garnavich P. M., et al., 2001, The luminosity of sn 1999by in ngc 2841 and the nature of peculiar type ia supernovae. preprint, astro-ph/0105490

Hamuy M., Phillips M. M., Suntzeff N. B., Schommer R. A., Maza J., Aviles R., 1996, AJ, 112, 2391

Hatano K., Branch D., Fisher A., Deaton J., Baron E., 1999, ApJS, 121, 233

Iwamoto K., Brachwitz F., Nomoto K., Kishimoto N., Hix W. R., Thielemann F.-K., 1999, ApJS, 125, 439

Jeffery D., Branch D., 1990, in Supernovae, Wheeler J. C., Piran T., eds., World Scientific, Singapore, p. 149

Kasen D., Nugent P., Wang L., Howell D. A., Wheeler J. C., Höflich P., Baade D., , Baron E., Hauschildt P., 2003, ApJ, 593, 788

Kim A. G., Linder E. V., Miquel R., Mostek N., 2004, MNRAS, 347, 909

Lentz E., Baron E., Branch D., Hauschildt P. H., 2001, ApJ, 557, 266

Mazzali P. A., 2000, A&A, 363, 705

Mihalas D., 1978, Stellar Atmospheres. W. H. Freeman, New York

Nugent P., Baron E., Branch D., Fisher A., Hauschildt P., 1997, ApJ, 485, 812

Nugent P., Phillips M., Baron E., Branch D., Hauschildt P., 1995, ApJ, 455, L147

Perlmutter S., Aldering G., Goldhaber G., Knop R. A., Nugent P., Castro P. G., Deustua S., Fabbro S., Goobar A., Groom D. E., Hook I. M., Kim A. G., Kim M. Y., Lee J. C., Nunes N. J., Pain R., Pennypacker C. R., Quimby R., Lidman C., Ellis R. S., Irwin M., McMahon R. G., Ruiz-Lapuente P., Walton N., Schaefer B., Boyle B. J., Filippenko A. V., Matheson T., Fruchter A. S., Panagia N., Newberg H. J. M., Couch W. J., The Supernova Cosmology Project, 1999, apj, 517, 565

Phillips M. M., 1993, ApJ, 413, L105

Reindl B., Tammann G. A., Sandage A., Saha A., 2005, ApJ, 624, 532

Thomas R., Kasen D., Branch D., Baron E., 2002, ApJ, 567, 1037

Appendix I: PHOENIX simulations

W7 model

The main model we used in our simulation was W7 devised by K.Nomoto((Iwamoto et al., 1999)). Fig. 8 and Fig. 9 display the number abundances of the main elements of this explosion model.

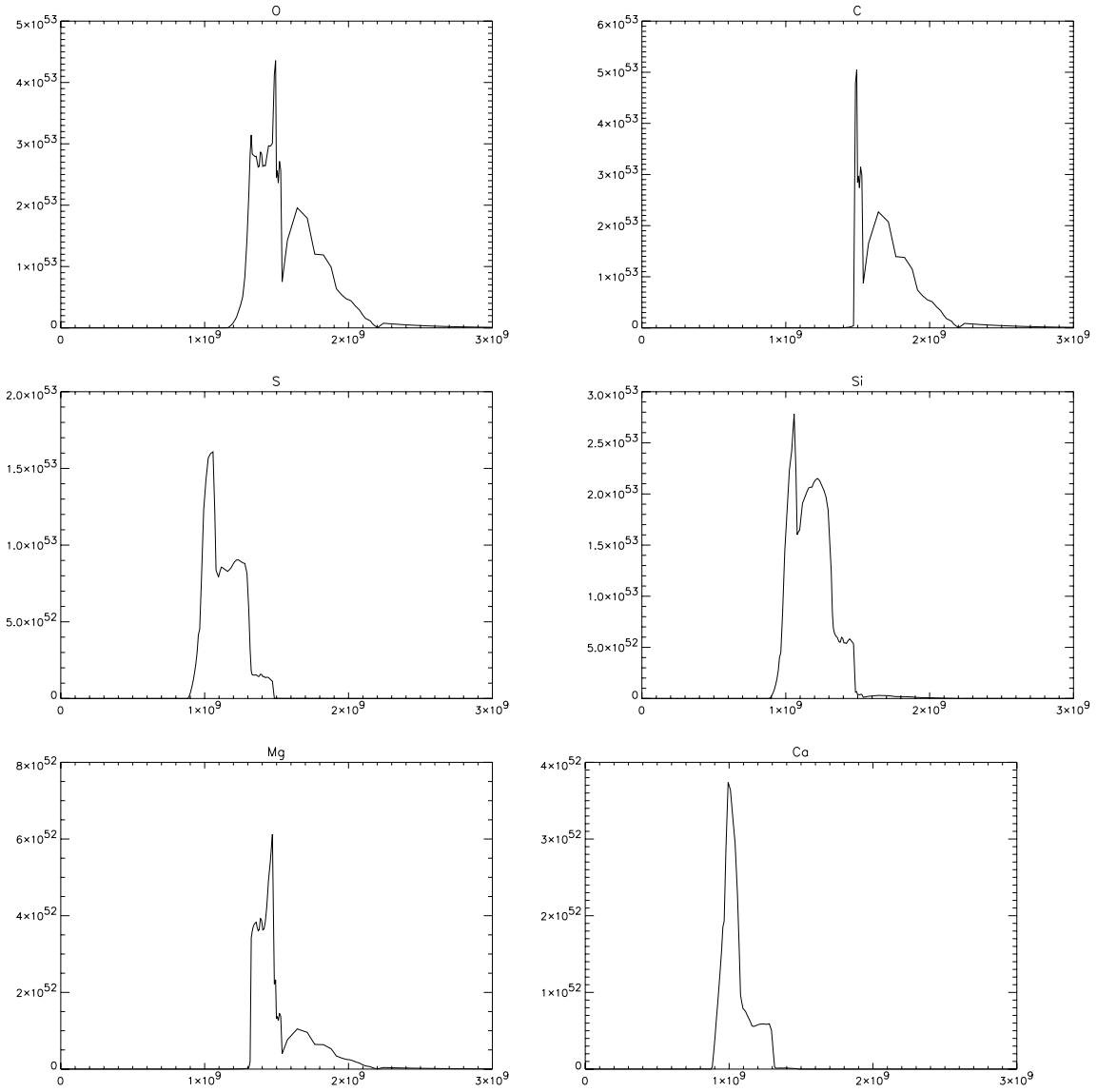

Figure 8: *W7 light elements abundances*

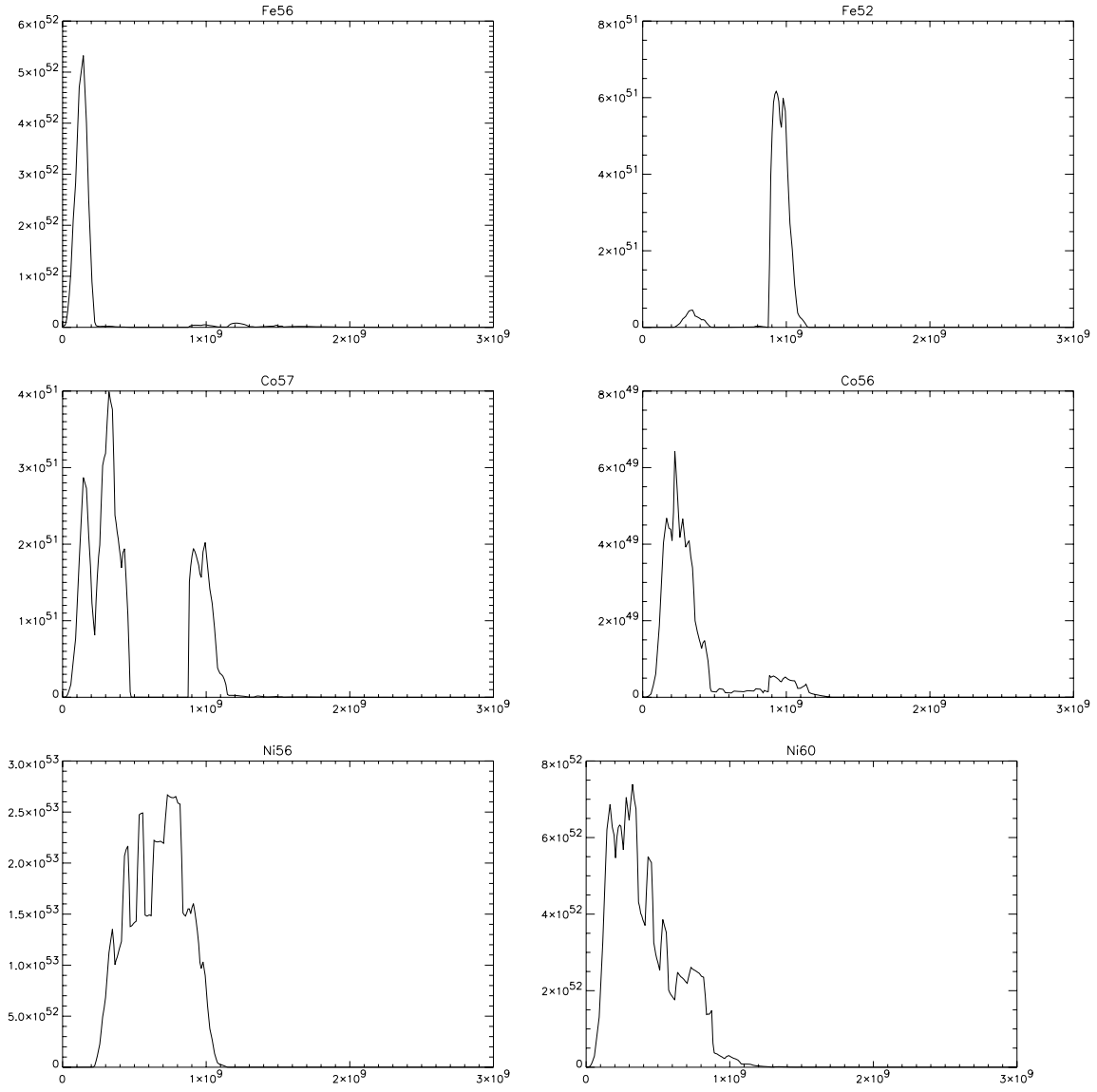

Figure 9: *W7 Iron family elements abundances*

Appendix II: Real supernovæ

In this appendix we present the spectra of the real supernovæ we used in this work.

name	Day after max	Blue absolute magnitude
sn1981b	0	-19.07
sn1986g	-1, -3, -5, 1, 3	-18.08
sn1989b	-1, -5	-18.58
sn1991bg	0, -2	-16.62
sn1991t	-3, 0	-19.44
sn1992a	0, -1, -5, 3, 5	-18.48
sn1994d	2, 3, 4, 5, -3, -4, -5	-19.0

Table 2: *Absolute blue magnitues and dates reminder*

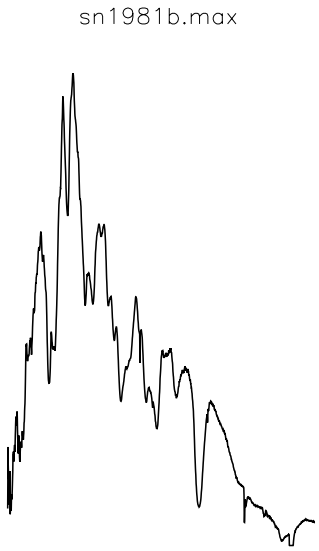

Figure 10: *Real supernovæ used, SN 1981B*

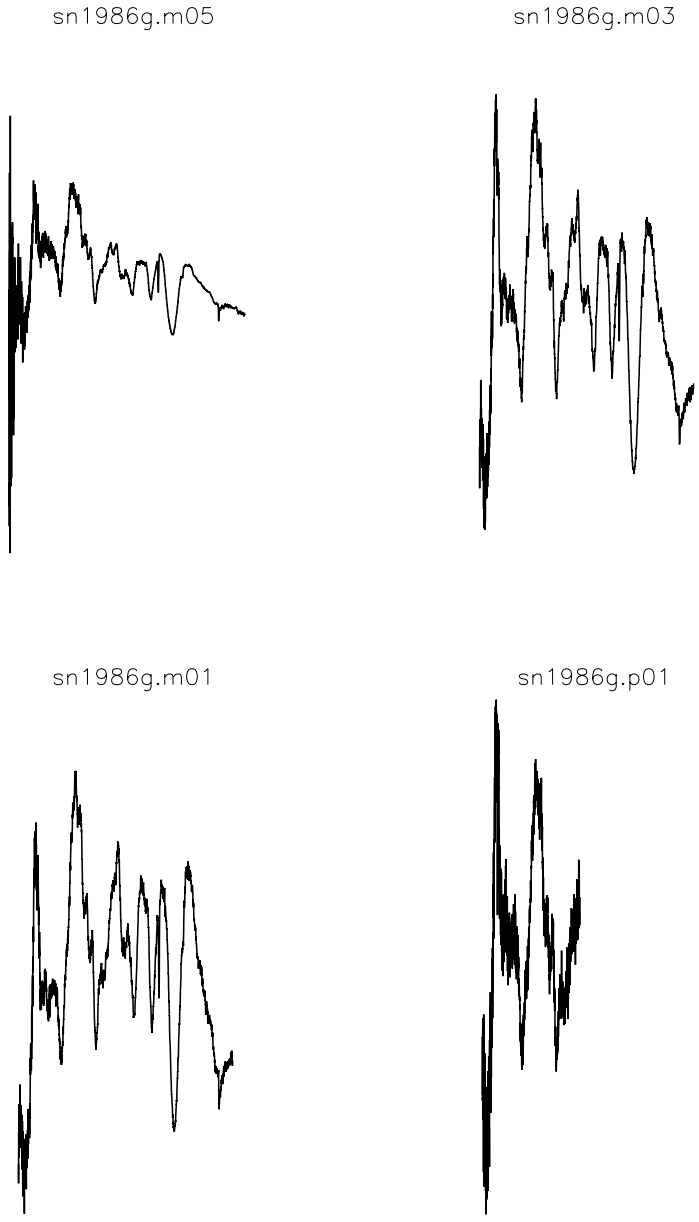

Figure 11: *Real supernovæ used, SN 1986G*

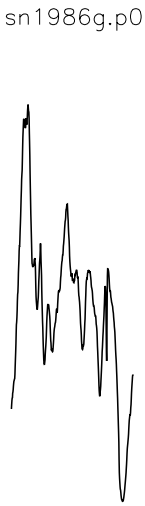

Figure 12: *Real supernovæ used, SN 1986G*

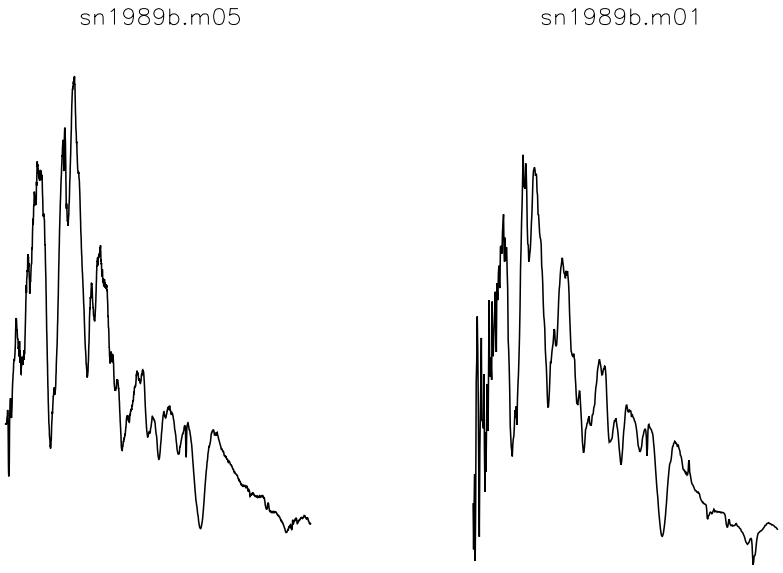

Figure 13: *Real supernovæ used, SN 1989 B*

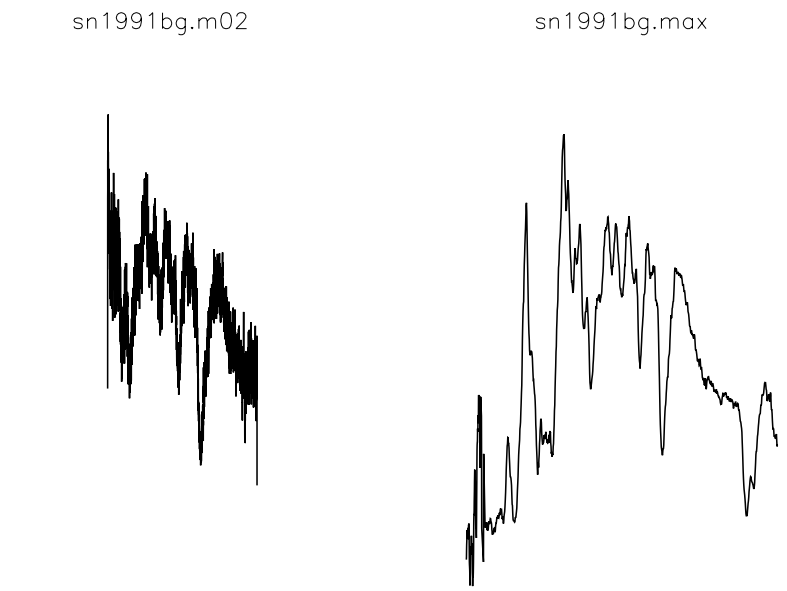

Figure 14: *Real supernovæ used, SN 1991bg*

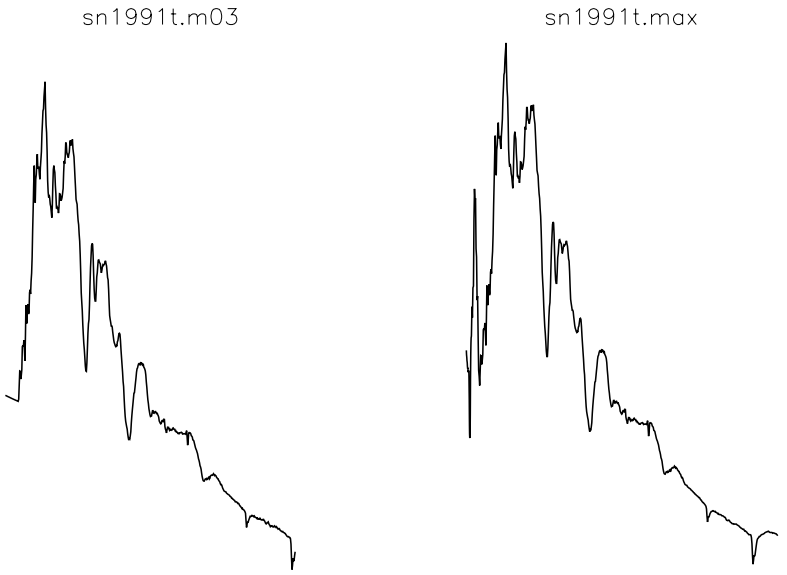

Figure 15: *Real supernovæ used, SN 1991T*

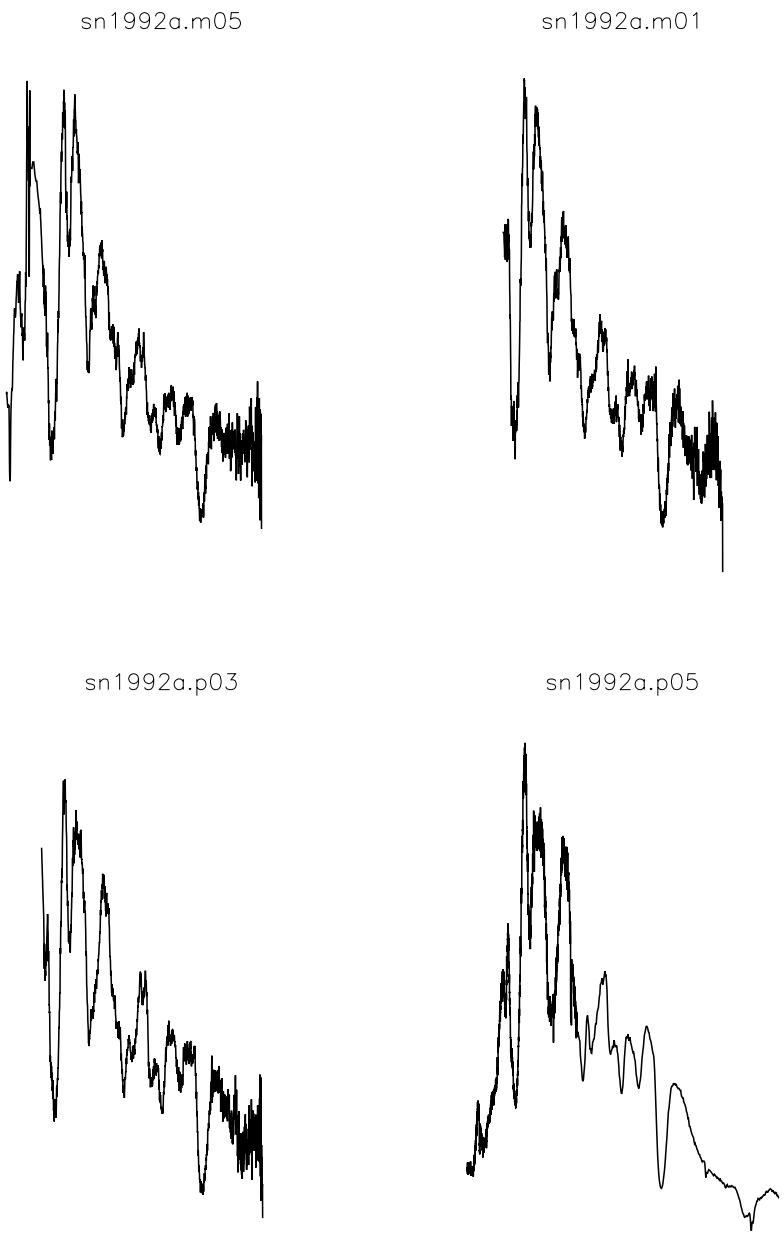

Figure 16: *Real supernovæ used, SN 1992A*

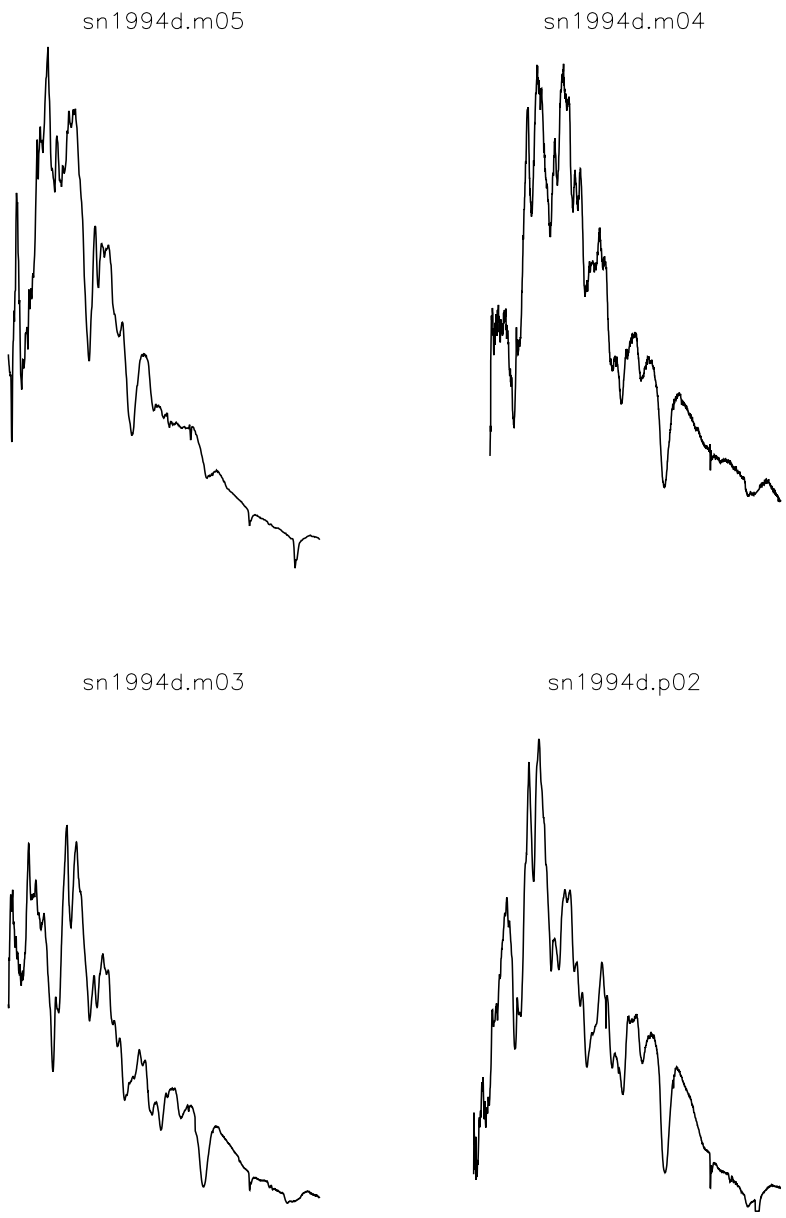

Figure 17: *Real supernovæ used, SN 1994D*

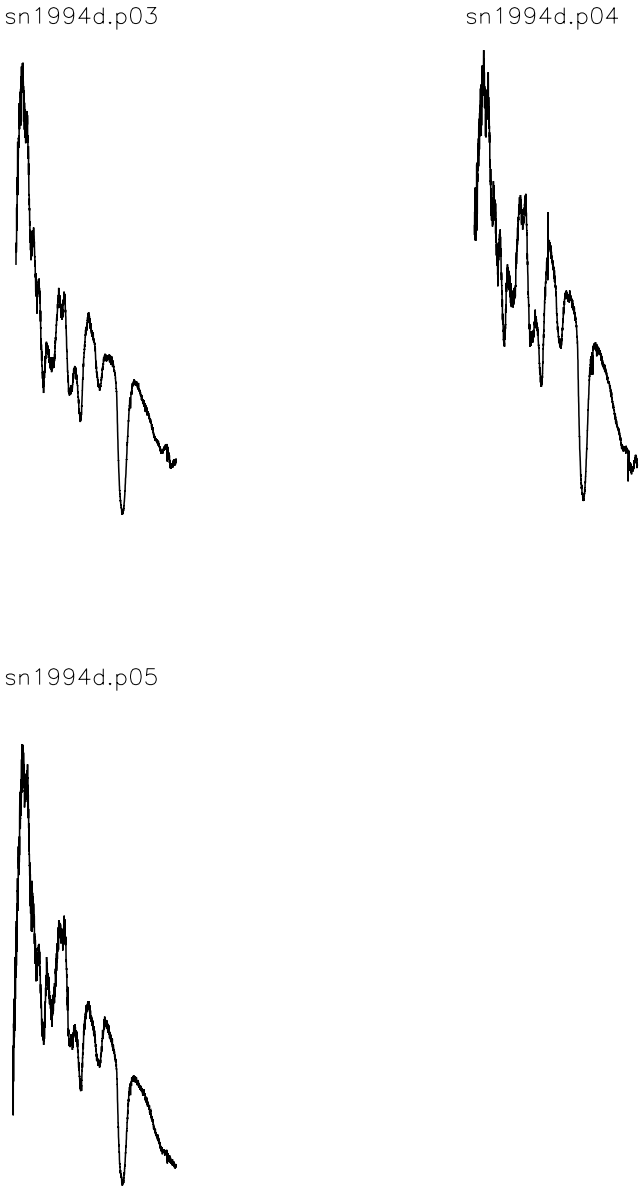

Figure 18: *Real supernovæ used, SN 1994D*

NOM : BONGARD (avec précision du nom de jeune fille, le cas échéant) Prénoms : Sébastien	DATE de SOUTENANCE 4 octobre 2005

TITRE : Transfert radiatif et étude spectrale des SNeIa dans le cadre de la Supernovae factory

Numéro d'ordre : 146-2005

DIPLOME DE DOCT.	DOCTEUR-INGENIEUR	DOCTORAT D'ETAT	DOCTORAT DE 3e CYCLE	Spécialité : Physique des Particules et Sciences de L'Univers
X	☐	☐	☐	

Cote B.I.U. – Lyon : T 50/210/19 / et bis	CLASSE :

RESUME :

Dans cette thèse, effectuée en cotutelle avec l'Université d'Oklahoma City, nous avons étudié le transfert radiatif dans les enveloppes en expansion rapide des supernovae de type Ia (SNeIa) dans le cadre de la collaboration SupernovaeFactory.

Ces étoiles qui explosent avec une luminosité comparable à celle d'une galaxie sont utilisées comme chandelles standard permettant d'étudier le comportement à grande échelle de l'univers. Nous avons utilisé le code de transfert radiatif PHOENIX développé par P. Hauschildt, F. Allard et E. Baron, pour simuler des spectres de SNeIa à différentes dates et luminosités afin d'étudier le processus de formation spectrale. Nous avons parallèlement élaboré un module de grille adaptative qui augmente sa robustesse de convergence.

Nous avons montré que la formation des spectres de SNeIa n'était pas aussi localisée que dans le modèle photosphérique standard mais qu'elle mettait en relation des régions allant de 5000 km/s à 20000 km/s pour des époques proches du maximum de luminosité. Nous avons de plus développé des indicateurs spectraux permettant de mesurer la luminosité des SNeIa avec une précision égale à celle des méthodes basées sur l'analyse des courbes de lumière. Il devient ainsi possible de contraindre de façon indépendante l'évolution des SNeIa avec le redshift, ce qui place ce travail à l'interface entre l'étude des supernovae en tant qu'objets stellaires et leur utilisation en cosmologie.

MOTS-CLES : Radiative transfer – Supernovae – Type Ia - Phoenix

Laboratoire de recherche : Institut de Physique Nucléaire de Lyon et l'Université d'Oklahoma

Directeurs de recherches : G. Smadja et E. Baron

Président du jury : R. Schaeffer Composition du jury : E. Baron – G. Smadja – D. Branch – J.-P. Chièze – P. Hauschildt	142 pages